

Level-3 Geometric Correction of FORMOSAT-2 Satellite Imagery and Efficient Image Resampling



By
Fahim Arif

A thesis submitted to the Faculty of Computer Science Department,
in partial fulfillment for the requirements of the degree of

DOCTOR OF PHILOSOPHY

College of Signals,
NATIONAL UNIVERSITY OF SCIENCES AND TECHNOLOGY,
Rawalpindi

March, 2009

© Copyright by Fahim Arif, 2009

Abstract

A significant problem in satellite imagery is geometric distortion. Accurate remote sensing and high resolution satellite images have made it necessary to revise the geometric correction techniques used for ortho-rectification. Conventional methods of photogrammetric modeling of remotely sensed images are insufficient for mapping purposes and need to be substituted with more rigorous approach to get a true orthophoto.

FORMOSAT-2, a newly launched remote sensing Taiwanese satellite, has high spatial resolution sensor onboard for a daily revisit orbit. However, like any image acquisition system, it also produces geometric distortions in its raw images. Pixel Projection Model (PPM) was devised by National Space Program Office (NSPO) Taiwan, for processing of Level-1A (Raw) satellite images to Level-2 (radio metrically corrected) images. Being systematically corrected, Level-2 images still possess terrain elevation, rotation-translation and geometric distortions. There was a dire need for enhancement of this model to produce Level-3 (geometrically corrected) image products.

A novel method for Level-3 correction of satellite images, especially suited for FORMOSAT-2, has been developed. The PPM has been enhanced to cater for geometric distortions caused by the attitude change in the satellite specifically in the pre-processing stage. The three attitude angles of the satellite are thus calculated and corrected as per the ground position or coordinates using least squares adjustments. The approach is based on non-systematic method in which physical modeling of the satellite imagery is considered. The mathematical model has been developed to calculate and correct instrument bias/ attitude angles. Ground Control Points have been integrated in the algorithm besides vertex matching

for more precise results. Results were verified by computing *MSE* for image to image matching and point to point matching. An improvement of 86.3% was obtained for the new Level-3 correction technique over the existing Level-2 algorithm.

Three conventional interpolation techniques for transformation of image pixels to earth coordinate system were also analyzed for improvement. The experimental results show that the cubic convolution based modeling is best suited for output pixel value transformation but it is computationally complex with a higher execution time. To improve this, a wavelet-transform based filter (Daubechies 4) was developed for image pixel transformation. The new method provides similar visual interpretation as cubic convolution but with much lower computational complexity and execution time. The proposed wavelet-transform based method is an order of magnitude faster than the cubic interpolation technique.

Level-3 geometrically corrected FORMOSAT-2 images can be used for disaster investigation/ prediction, environmental monitoring, vegetation evaluation, and multi-temporal image matching. In our work, we have focused on the application of geometrically corrected imagery for disaster investigation.

Acknowledgements

I am humbly thankful to the ‘Almighty Allah’ for his blessings and giving me the wisdom, knowledge and understanding, without which I would not have been able to complete my thesis research work.

I wish to express my deepest appreciation to my thesis research supervisor Dr. Muhammad Akbar for his supervision, dedication and commitment to this research. Also, my special thanks to all of my guidance committee members namely Professor Dr. I. M. Qureshi, Professor Dr. M. N. Jafri and Dr. Salim Akbar for their suggestions in this research work. Their advice and critical review was useful in giving it final shape.

I am grateful to Assistance Professor Dr. Aysegul Cuhadar of System and Computer Engineering Department of Carleton University for her support, valuable comments, and allowing me access to image and video processing lab. She provided the unique direction I needed, which would not have been possible otherwise. She contributed a lot in writing and finalizing this dissertation.

I am especially thankful to National Space Program Office (NSPO), Taiwan for permitting me to use and reproduce various imageries taken by FORMOSAT-2 satellite. I would like to express my sincere thanks to Dr. An-Ming Wu of NSPO for providing me the access to satellite images and ancillary data of FORMOSAT-2.

I am thankful to Dr. Muhammad Hussein Radfar of Carleton University for his support and thoughtful feedback. Also, I am gratified to Brigadier (Retired) Khan Muhammad of National University of Sciences and Technology, for final proof reading of this thesis and necessary guideline.

“Thank you” seems to be inadequate to show how patient and supportive my wife had been. I would like to thank deeply my parents for being patient and continuously giving me their special warmth and encouragement. Nevertheless, I would like to thank all my teachers, my friends and my family members for their valuable moral support, patience and encouragement so that I became able to complete my research work.

Table of Contents

Chapter 1: Introduction

1.1	Premise	1
1.2	Geometric Distortions in Satellite Imagery	1
1.3	Problem Statement and Research Objectives	3
1.4	Contribution of This Research	5
1.5	Outline of the Thesis	6

Chapter 2: Ortho-Rectification Using Geo-referencing

2.1	Introduction	8
2.2	Computing the Parameters of a Two-dimensional Coordinate Transformations	9
2.3	Filling an Array Aligned with the Ground Coordinate System	10
2.4	Mathematical Relationship between Coordinate Systems	12
2.5	Selection of Ground Control Points	16
2.6	Summary	17

Chapter 3: Formulation of Pixel Projection Model

3.1	Introduction	18
3.2	FORMOSAT-2 Satellite	19
3.2.1	Remote Sensing Instrument (RSI)	19
3.2.2	Daily Revisit Orbit	20
3.3	Factors Affecting Satellite Image Geometry	22
3.3.1	Parameters of Orbit Model	23
3.3.2	Earth Model	23
3.4	Pixel Projection Modeling	24
3.5	Mathematical Formulation of PPM	25
3.5.1	Position and Information of Satellite	26
3.5.2	Rotation Matrix (RM) and Euler Angles	27
3.5.3	Pixel Line-of-Sight (LOS) Vector from Recording Platform (Body) to ECF	29
3.5.4	Intersection of Recording Platform LOS Vector and the Geodetic Surface	32
3.6	Summary	36

Chapter 4: Level-3 Geometric Correction of FORMOSAT-2 Images

4.1	Introduction	37
4.2	Test Images and Ancillary Data	38

4.3	Level-3 Geometric Correction Technique	40
4.3.1	Geo-referencing Based on Pixel Projection Model (PPM)	41
4.3.2	Integration of GCPs	42
4.3.3	Projection by Least Squares Regression	43
4.3.3.1	Linearization of Equation for Attitude Determination	45
4.3.3.2	Finding Matrix of Coefficients of Unknown	47
4.3.3.3	Solution of Least Squares Adjustments	48
4.3.4	The Iteration Process of Level-3 Correction Algorithm	49
4.4	Improvements Achieved in PPM	51
4.5	Summary	53

Chapter 5: Experimental Results

5.1	Introduction	54
5.2	Residual Analysis	54
5.2.1	Image Matching	55
5.2.2	Point to Point Error Estimation	56
5.3	Image Resampling	59
5.3.1	Applying Different Approximations for Pixel Transformations	60
5.3.1.1	Nearest Neighbor (NN)	60
5.3.1.2	Bilinear Interpolation (BI)	60
5.3.1.3	Cubic Convolution (CC)	60
5.3.1.4	Comparison of Resampling Methods	61
5.3.1.5	Discussion on Resampling Methods Result	63
5.3.2	Wavelet Based Resampling Algorithm for Image Transformation	65
5.3.2.1	Daubechies 4 (D-4) Wavelet Filter	67
5.3.2.2	Results of D-4 Wavelet Based Resampling	68
5.3.2.3	Analysis of D-4 Wavelet Based Resampling	68
5.3.2.3.1	Complexity of Algorithm	70
5.3.2.3.2	RMS Analysis in Case of D-4	72
5.3.2.3.3	Execution Time	73
5.4	Application to Disaster Investigation	74
5.5	Summary	77

Chapter 6: Conclusions and Recommendations

6.1	Overview	79
6.2	Achievements and Applications	80
6.3	Limitations	82
6.4	Recommendations and Future Research	83
6.4.1	Specific to FORMOSAT-2 Imagery	83
6.4.1.1	Band to Band Co-registration	83
6.4.1.2	Digitized Map of Pakistan	84
6.4.1.3	Other Causes of Geometric Distortions	84
6.4.2	Other Remote Sensing Satellites and Challenges to Image Processing and Analysis	85

6.4.2.1 Different Resolutions	85
6.4.2.2 Techniques for Machine Assisted Interpretation	86
6.4.2.3 Multi-source and Multi-sensor Images	86
6.5 Summary	87

Appendices

A. Two-dimensional Coordinate Transformations	89
B. Digital Resampling	92
C. Systematic Formulation of Normal Equations into Matrix Notation	95

References	98
-------------------	-----------

List of Figures

Figure	Caption	Page
1.1	Geometric correction process	3
2.1	Geo-referencing to the ground coordinates	11
2.2	Example of geo-referencing	15
3.1	RSI coverage and the daily revisit of FORMOSAT-2	22
3.2	Platform attitude angles	23
3.3	Schematic for geo-referencing without DEM	25
3.4	Relationship between ground and satellite positions	26
3.5	Geometry of a digital CCD array	30
3.6	Geometry of satellite and earth line of sight vector	30
3.7	Projection of a point to geodetic surface	32
3.8	Geodetic latitude and altitude of a point	34
4.1	FORMOSAT-2 images obtained from NSPO for testing purpose	38
4.2	Portion of a dim file presenting ancillary data of RS image	39
4.3	Geometrically corrected images using pixel projection method	40
4.4	Geo-referencing with PPM	41
4.5	GCPs integration in PPM	43
4.6	A function of one variable	46
4.7	Iteration process in Least Squares adjustment algorithm	50
4.8	Level-3 pixel projection method for geometric correction	51

4.9	Level-3 geometrically corrected test images of Pakistan	52
5.1	Original and geo-referenced images of Islamabad	55
5.2	AOI in original and geo-referenced images	56
5.3	Original AOI image with 8 CPs	57
5.4	Results of three different approximation techniques for Islamabad image	61
5.5	Results of three different approximation techniques for Abbottabad image	61
5.6	3-dimensional plots of the approximations applied on test image 1 (Islamabad)	62
5.7	3-dimensional plots of the approximations applied on test image 2 (Abbottabad)	62
5.8	2-dimensional contour plots of the approximations techniques applied on test image 1 (Islamabad)	65
5.9	2-dimensional contour plots of the approximations techniques applied on test image 2 (Abbottabad)	65
5.10	D-4 Kernel Application	66
5.11	Test images resampled with D-4 method	68
5.12	Resampled test images with randomly selected 8 points	69
5.13	Graphical comparison of complexities	71
5.14	Images of FORMOSAT-2 after disastrous category 5 Hurricane Katrina struck New Orleans	75
5.15	Images of FORMOSAT-2 of Alert, Canada taken in Mar 2006	76
A-1	Comparison of two dimensional coordinate system with ground system	90
A-2	Scaled $X'Y'$ coordinate system and its superimposition onto	91

the *EN* ground coordinate system.

B-1	Form of the sinc function	93
B-2	Shape of the bicubic, bilinear and nearest neighbor interpolations	93

List of Tables

Table	Caption	Page
1.1	Terminology of different pre-processed HR image products	4
2.1	Ground and image coordinates for control points	11
2.2	Converted column and row coordinates	13
3.1	Technical specifications of FORMOSAT-2 satellite	19
3.2	Spectral bands of FORMOSAT-2 and their characteristics	20
3.3	Areas covered by daily revisit	22
4.1	Ancillary data of the test images	39
4.2	Image coordinates with corresponding location coordinates	43
5.1	<i>MSE</i> using pixel projection method (PPM)	59
5.2	<i>MSE</i> using Level-3 geometric correction method	59
5.3	Summary of complexities of interpolation techniques	71
5.4	<i>Rms</i> values for different interpolation methods and their resemblance with the original images	72
5.5	Execution time for interpolation methods	73

List of Abbreviations

AOI	Area of Interest
BI	Bilinear Interpolation
CC	Cubic Convolution
CCD	Charged Coupled Device
CPs	Control Points
D-4	Daubechies 4
DEM	Digital Elevation Model
DIMAP	Digital Map
DN	Digital Number
ECF	Earth Centre Fixed
ECI	Earth Centre Inertial
GCPs	ground Control Points
GPS	Global Positioning System
groundels	ground elements
GSD	Ground Sampling Distance
HR	High Resolution
IIFOV	Instantaneous Field Of View
J2000	Julian Day 2000
Kms	Kilometers
LOS	Line-Of-Sight
LVLH	Local Vertical Local Horizontal

m	Meters
MS	Multi-Spectral
MSE	Mean Square Error
NAD27	North American Datum 1927
NN	Nearest Neighbour
NSPO	National Space Program Office
PAN	Panchromatic
PPM	Pixel Projection Model
RM	Rotation Matrix
RMS	Root Mean Square
SAR	Synthetic Aperture Radar
RS	Remote Sensing
RSI	Remote Sensing Instrument
UTC	Universal Coordinated Time
WGS84	World Geodetic System 1984

Introduction

1.1 Premise

This chapter covers the areas which are vital for understanding the material presented in the thesis and thus for appreciating their contribution to the geometric rectification of FORMOSAT-2 satellite imagery. Initially, it may seem that the problem is very specialized but this is not so. It will be shown how various aspects of the problem relate to many other fields such as, image processing, computer vision, photogrammetry and aerospace control systems.

The initial sections in this chapter provide an introduction to geometric distortions introduced in satellite imagery, methods and levels of their rectification. Some basic characteristics of FORMOSAT-2 satellite are also included since FORMOSAT-2 images are used to produce Level-3 geometrically corrected products. Finally, the contributions of this research are introduced and the organization of the dissertation is outlined.

1.2 Geometric Distortions in Satellite Imagery

Geometric distortion is an error in an image, between recorded image coordinates and its actual earth coordinates even if projected theoretically with an ideal sensor under ideal conditions [1, 2]. These distortions are classified into internal distortions, resulting from the geometry of the sensor and external distortions resulting from the attitude of the sensor or the shape of the object [3-5].

Potentially there are many more sources of geometric distortion of image data than radiometric distortion and their effects are more severe. These can be related to a number of

factors, including rotation of the earth during image acquisition, the finite scan rate of some of the sensors, the wide field of view of some of the sensors, the curvature of the earth, non-ideal behavior of sensors, variations in platform altitude and velocity and panoramic effects related to the imaging geometry. Geometric distortion in satellite imagery can rise when velocity (speed and direction) and orientation are variable over the scanning period [6-14].

Geometric correction is undertaken to overcome geometric distortions resulting from factors stated above during the acquisition of digital or scanned image. Rectification process is achieved by establishing the relationship between the image coordinate system and the geographic coordinate system. For this, sensor calibration data, measurement of position and attitude, determination of ground control points, atmospheric conditions etc. are required [15, 16]. Rectification process involves a number of stages, of these most important are: selection of suitable method, determination of parameters, checking for accuracy and interpolation or resampling of post-process data [17]. These are diagrammatically shown in Figure 1.1. Methods of geometric correction can be broadly classified as systematic correction, non-systematic correction and a combination of the two [18-20]. Systematic correction is applied when the geometric reference data or the geometry of the sensor is measured. Non-systematic correction is used when transformation from a geographic coordinate system to an image coordinate system or vice versa is determined. A combined method is the choice in which first systematic correction is applied and then residual errors are reduced by applying a non-systematic method [21].

Geometric transformation is a function which maps the coordinates of a pixel from one set of values to another. For practical purposes, the best way to implement this for rectification is the inverse mapping strategy. Each pair of pixel coordinates from the

synthesized output image is mapped to a point in the input image. The intensity at the input image point is assigned to the output pixel [22-25].

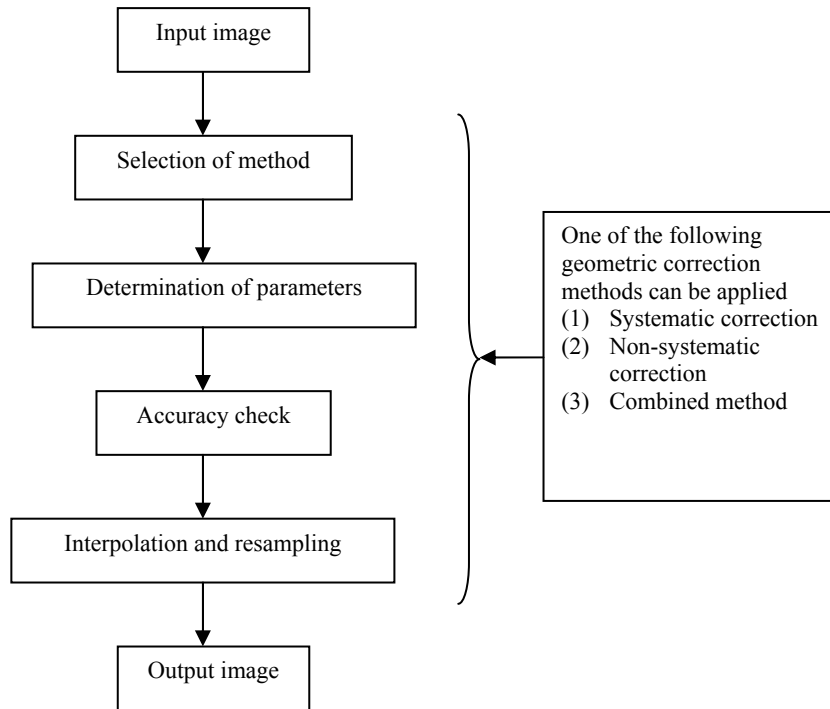


Figure: 1.1 Geometric correction process

1.3 Problem Statement and Research Objectives

In Remote Sensing (RS), different types of High Resolution (HR) satellite imagery with different levels of pre-processing can be obtained. Unfortunately, different image providers use a range of terminologies to denominate the same type of image data [26]. Table 1.1 gives the terminologies of different pre-processed products for some HR images.

The raw Level-1A images with only normalization and calibration of the detectors without any geometric correction are satellite-track oriented. In addition, full metadata related to sensor, platform and image are provided [27]. The geo-referenced Level-2 images corrected for systematic distortions. Since they have been systematically corrected and geo-referenced, the Level-2 images still retain the terrain elevation distortions, rotation-

translation distortions and geometric distortions [28-30]. Since Level-2 images are not in their original geometry, physical models can still be developed for using basic metadata information to produce Level-3 geometrically corrected images.

Table: 1.1 Terminology of different pre-processed HR image products

Terminology used for HR Image Data	SPOT5 (French) 2002	RADARSAT-2 (Canadian) 1995-2007	OrbView3 (US Commercial) 2003	IKONOS-II (US Commercial) 2000	QuickBird3 (US Commercial) 2001	FORMOSAT -2 (Taiwan) 2004
Raw Data	0A	Signal data	----	----	----	----
Normalized & Calibrated	1A	Single look complex	Basic	----	Basic	1A
Sub-pixel Accuracy	1B	Ground range	----	----	Standard	----
Geo-referenced (GCPs)	2A	Map	----	Geo standard	----	2
Radiometrically Corrected	2B	Precision map	----	Reference pro	----	----
Geometrically Corrected	3	Ortho	Ortho	Precision precision-plus	Ortho DG DOQQ	3

Based on the above discussion, this thesis addresses the problem of achieving Level-3 geometric correction of FORMOSAT-2 images. The research objective is to develop a new model for processing of Level-2 images obtained with Pixel Projection Model (PPM) [31-37]. The aim is to remove geometric distortion from images in the pre-processing stage. Our approach is based on non-systematic method in which physical modeling of the satellite imagery is considered. In that we used fundamental matrix form of least square adjustment for mathematical formulation [38]. The mathematical model was then developed to calculate and correct instrument bias and the attitude angles (discussed in chapter 4). In addition, GCPs are integrated into the algorithm besides vertex matching of RS images with ground

coordinates for more precise results [38]. Test images and ancillary data in DIMAP format are provided by National Space Program Office (NSPO) Taiwan.

We investigated three conventional resampling methods for output pixels transformation [39]. A novel approach, Daubechies-4 (D-4) wavelet filter, has been applied and validated for the same purpose [40, 41]. Finally, Level-3 geometrically corrected FORMOSAT-2 images can be used in different application areas like environmental monitoring, disaster early warning systems, vegetation index measuring etc [42, 43]. In chapter 5 we mainly focused on the application of RS images in disaster investigation in which we processed three consecutive images of the same location having disasters occurring.

1.4 Contribution of This Research

The main contribution of this research is the up-gradation and enhancement of Pixel Projection Method (PPM) for FORMOSAT-2 satellite imagery. PPM was initially designed for achievement of Level-2 corrected images without correcting geometric distortions. To achieve Level-3 geometric correction, the PPM application was amended such that geometric distortions are removed. We developed the application to cater for geometric distortions caused by the change in attitude of the satellite specifically. The three attitude angles of the satellite are thus calculated and corrected as per the ground position or coordinates with the help of least square adjustments. The aim was to eradicate geometric distortion from images in the pre-processing stage. Our approach is based on non-systematic method in which physical modeling of the satellite imagery is considered which was achieved through least square adjustment. The mathematical model has been developed to calculate and correct

instrument bias and the attitude angles. In addition, GCPs are integrated into the algorithm besides vertex matching of RS images with ground coordinates for more precise results.

We investigated three conventional resampling methods for output pixels transformation. An exceptional approach of Daubechies-4 (D-4) wavelet filter was applied for the same purpose.

The practical application of this algorithm in the difficult domain of photogrammetry is manifold. Geometrically corrected level-3 images can be utilized in a variety of applications like environmental monitoring, disaster early warning systems, vegetation index measuring etc. However, particularly in the field of disaster investigation this technique was applied and shown with the help of examples.

1.5 Outline of the Thesis

This thesis is organized into six chapters. Chapter 1 is introduction to the thesis. It introduces the issues related to geometric distortions in RS images. It describes the problems addressed in this thesis.

Chapter 2 provides the background material on ortho-rectification with geo-referencing. The basic method of geo-referencing is explained. It includes computing the parameters of a two-dimensional coordinate transform and filling an array aligned with the ground coordinate system. GCPs are used for geo-referencing and this method is further elaborated with the help of a diagram. Geo-referencing is also known as ground registration. It performs geometric rectification at an initial stage.

Chapter 3 illustrates the formulation of PPM. An introduction to FORMOSAT-2 satellite and factors affecting its image geometry are given. Mathematical modeling of PPM is explained in detail. Level-3 geometric correction using least square method is discussed in

Chapter 4. Test images and ancillary data, mathematical formulation, algorithm and results are also presented in this chapter.

Chapter 5 presents the analysis, experimentation and application of Level-3 geometrically corrected FORMOSAT-2 satellite images. Results are validated through rigorous analysis of residuals by image to image and point to point matching. Two different experiments of resampling techniques for RS images are also elucidated in this Chapter. Application in disaster investigation of Level-3 processed images is also illustrated with the help of daily revisit imagery. Chapter 6 summarizes the thesis by conclusions and recommendations for future work.

Ortho-Rectification using Geo-referencing

2.1 Introduction

RS digital images are obtained via different sources like satellite imaging sensors, digital cameras and scanned aerial photographs. In its elementary form, a digital image bears no relationship to a ground coordinate reference system. Rather, its coordinate basis consists of integer column and row numbers which specify the location of a pixel within a rectangular image array. Geo-referencing, which is also called ground registration, is a technique in which a digital image is processed so that the column and rows of the resulting product are aligned with north and east in a ground coordinate system [44, 45]. Some researchers, particularly in the field of remote sensing, refer to geo-referencing as rectification of digital imagery [46]. The process of geo-referencing an image involves two fundamental steps. First, the parameters of a two-dimensional coordinate transformation (see appendix A) which relate the digital image to the ground system are computed. Second, an array which is aligned with the ground coordinate system is filled with appropriate values that quantify the brightness of the ground at the corresponding locations [47-49].

This chapter describes elementary method for compiling planimetric maps from vertical photographs and satellite images. This technique is relatively simple to perform and generally requires simpler and less expensive equipment compared to the rigorous photogrammetric mapping techniques. The technique explained in Chapters 3 and 4 are more sophisticated and give more precise and accurate results.

2.2 Computing the Parameters of a Two-dimensional Coordinate Transformation

As a first step, a number of GCPs, identifiable in the image and for which accurate ground coordinates are available or known are manually selected. The column and row image coordinates of each GCP are obtained and subsequently related to the ground coordinates. Various image manipulation programs are available for calculating the image coordinates [50-56].

Coordinate transformation in geo-referencing converts ground coordinates (x and y) to image coordinates (X and Y). This conversion (from ground to image) might seem to be backwards, however, it is logical. Image coordinates of the common points serve as control for the transformation, and the resulting parameters give relationship from ground to image coordinates. Although any two-dimensional coordinate transformation can be used, but conformal and affine are the most often employed transformations because of their convenience and suitability [57]. For expediency purpose we use the two-dimensional conformal coordinate transformation, which are derived in appendix A, and are repeated here as Equation 2.1.

$$\left. \begin{aligned} X &= ax - by + T_x \\ Y &= ay + bx + T_y \end{aligned} \right\} \quad (2.1)$$

where x and y are ground coordinates and X and Y are image coordinates obtained by converting from their column and row values. Whereas a , b , T_x , and T_y are the parameters determined during the first step. Once computed, these parameters are used to transform coordinates of additional points from the ground system to the image system. The reason for this arrangement of the transformation will become apparent in the description of the second step in Section 2.3.

2.3 Filling an Array Aligned with the Ground Coordinate System

In the second step of geo-referencing, an image that is aligned with the ground coordinate system is produced. The ground is divided into rectangular grids of individual elements called groundels (ground elements), equivalent to pixels of a digital image. Pixels have no specific relationship to the ground; groundels are arranged at a specified spacing in a grid which is parallel to the ground coordinate system. For each groundel, the x and y coordinates of its center point are transformed, based on the parameters computed in the first step, into corresponding image coordinates. The brightness value from the image at the corresponding location is then inserted into the groundel array. This involves the process of resampling (see Appendix B). This process is applied to each groundel. It produces the geo-referenced image in the groundel array.

The geo-referencing process is more elaborated in Figure 2.1 [47]. Figure 2.1 (a) shows an 8 x 8 pixel digital image prior to the geo-referencing process. The image is represented as a square, that is how it appears on a computer screen. The solid line grid of Figure 2.1 (b) represents an array of groundels which are nominally aligned with the ground coordinate system xy . Nominal ground coordinates are associated with the centers of the groundels, shown as small dots in Figure 2.1 (b). The dotted lines represent the digital image as it would appear when properly aligned with the ground system. Four control points (1, 2, 3, and 4) having coordinates in the ground xy system shown in the image are manually selected. Coordinates of these control points in image system of Figure 2.1 (a) and the ground system are listed in Table 2.1. The image coordinates corresponding to pixel centers indicated by crosses in Figure 2.1 (a). These are specified to the nearest row and column number, which is commonly used in most geo-referencing applications. But more elaborate

techniques are now available which yield accurate fractional row and column coordinates [58-63].

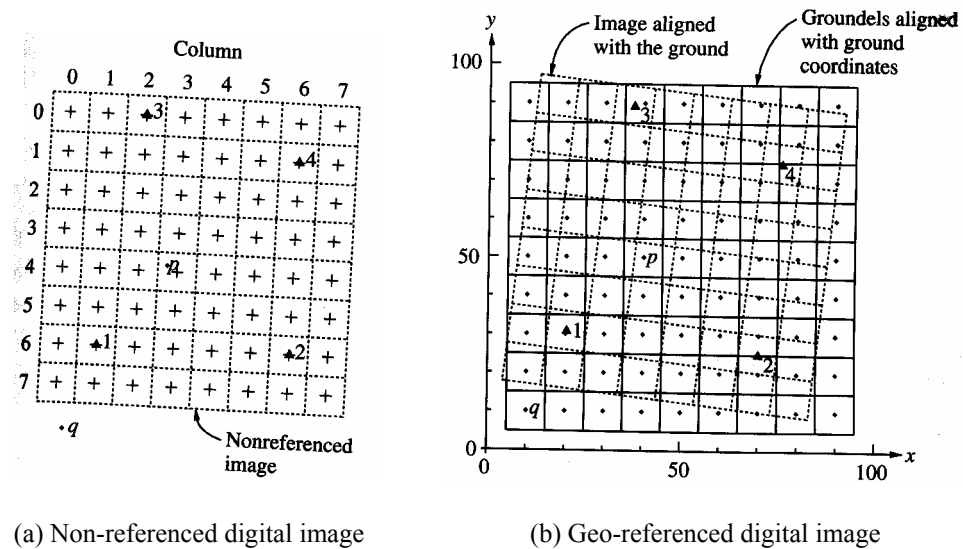


Figure: 2.1 Geo-referencing to the ground coordinates.

Table: 2.1 Ground and image coordinates for control points.

Points	Ground Coordinates		Image Coordinates	
	x	y	Column	Row
1	20.4	30.6	1	6
2	70.1	24.9	6	6
3	37.1	89.3	2	0
4	75.8	74.4	6	1

Coordinate transformation yields the mathematical relationship between the image and ground coordinates. It is useful to convert the column and row coordinates of image pixels to the more conventional XY system. In Figure 2.1 (a) column coordinates increase from left to right, like conventional X coordinates but the row coordinates increase from top to bottom, which is opposite to the conventional Y coordinates. Because of this configuration,

image coordinate system results in a left-handed coordinate system, as opposed to the more commonly used right-handed system. But ground coordinate system is typically a right handed coordinate system. Transformation of a left-handed system to a right-handed system can cause mathematical inconsistencies in certain coordinate transformations, such as the conformal transformation. This inconsistency can be remedied by a number of approaches.

One approach is to use the row coordinates as the abscissa and the column coordinates as the ordinate. This results in a right-handed coordinate system rotated 90° clockwise. Another approach is to simply use a transformation that is able to account for the difference between left and right-handed coordinate systems. The affine transformation has this capability by virtue of its separate x and y scale factors, one of which will be positive and the other negative. A third method is to convert the image coordinates from a left-handed system with the origin in the upper left corner to a right-handed system with its origin in the lower left corner [64]. This is accomplished by selecting the column coordinate as the abscissa and calculating ordinate values by subtracting row coordinates from the maximum row number.

2.4 Mathematical Relationship between Coordinate Systems

As stated earlier the two-dimensional conformal transformation is being used to relate ground coordinate system of Figure 2.1 (b) to the image coordinate system of Figure 2.1 (a). Using image coordinates from Table 2.1, a right-handed XY coordinate system is created using the third method described in Section 2.3. The maximum row number of the image is 7, therefore the original row coordinates are subtracted from 7 to obtain Y coordinates. The resulting XY image coordinates are listed in Table 2.2.

Table: 2.2 Converted column and row coordinates

Points	Original Image Coordinates		Converted Image Coordinates	
	Column	Row	X=Column	Y=7-Row
1	1	6	1	1
2	6	6	6	1
3	2	0	2	7
4	6	1	6	6

Equation 2.2 is based on Equation 2.1. Values of x and y from Table 2.1 have been substituted in Equation 2.1 to get Equation 2.2. This equation is used to transform xy ground coordinate system to the XY converted image coordinate system.

$$\left. \begin{aligned}
 20.4a - 30.6b + T_X &= 1 + V_{X_1} \\
 30.6a + 20.4b + T_Y &= 1 + V_{Y_1} \\
 70.1a - 24.9b + T_X &= 6 + V_{X_2} \\
 24.9a + 70.1b + T_Y &= 1 + V_{Y_2} \\
 37.1a - 89.3b + T_X &= 2 + V_{X_3} \\
 89.3a + 37.1b + T_Y &= 7 + V_{Y_3} \\
 75.8a - 74.4b + T_X &= 6 + V_{X_4} \\
 74.4a + 75.8b + T_Y &= 6 + V_{Y_4}
 \end{aligned} \right\} \quad (2.2)$$

Where a , b , T_X , and T_Y are parameters explained in Section 2.2.

V in Equation 2.2 shows residuals (see Appendix C for details). Using the least squares approximation, Equations 2.2 is solved for the most probable values of a , b , T_X , and T_Y , which are

$$\left. \begin{aligned}
 a &= 0.09921 \\
 b &= 0.01148 \\
 T_X &= -0.67 \\
 T_Y &= -2.27
 \end{aligned} \right\} \quad (2.3)$$

Once transformation parameters have been computed, the task of geo-referencing is completed by filling the groundel array with brightness values from the digital image. The 9x9 groundel array is shown in Figure 2.1 (b). This involves 81 separate applications of the above transformation, each followed by placing of the brightness value from the image through resampling. For example, point p in Figure 2.1 (b) has ground coordinates of $x = 40$ and $y = 50$. Its image coordinates X and Y , by substitution into Equation 2.1, are

$$X = 40a - 50b + T_x = 40(0.09921) - 50(0.01148) + (-0.67) = 2.7 \quad (2.4)$$

$$Y = 50a + 40b + T_y = 50(0.09921) + 40(0.01148) + (-2.27) = 3.1 \quad (2.5)$$

Expressing the location in column and row coordinates gives

$$\text{Column} = X = 2.7 \quad (2.6)$$

$$\text{Row} = 7 - Y = 3.9 \quad (2.7)$$

The column and row location is indicated by the position of point p in Figure 2.1 (a). This position falls within the area of the pixel at column = 3 and row = 4, so the brightness associated with that particular image pixel could be copied into the corresponding groundel at $x = 40$ and $y = 50$. In this case it is accomplished by using the nearest-neighbor method described in Appendix B. Alternatively, bilinear or cubic interpolation could be used for the resampling.

Another possibility for some of the groundels is to fall outside the limits of the digital image such as point q . From Figure 2.1 (b), point q corresponds to the groundel at coordinates $x = 10$ and $y = 10$. Transforming these coordinates into the XY image system gives

$$X = 10a - 10b + T_x = 10(0.09921) - 10(0.01148) + (-0.67) = 0.2 \quad (2.8)$$

$$Y = 10a + 10b + T_y = 10(0.09921) + 10(0.01148) + (-2.27) = -1.2 \quad (2.9)$$

Expressing this location in column and row coordinates gives

$$\text{Column} = X = 0.2 \quad (2.10)$$

$$\text{Row} = 7 - Y = 8.2 \quad (2.11)$$

Now the row coordinate of 8.2 is beyond the maximum row number of 7, there is no brightness value from the image corresponding to this particular groundel. As per padding phenomenon, it is appropriate to use a default value of 0 for the groundel brightness value.

Figure 2.2 shows the result of geo-referencing applied to a satellite image. Figure 2.2 (a) shows the non-referenced image. Notice that although true directions of streets in the area correspond to basic directions (north, south, east and west) but the general directions of streets appear to be rotated approximately 10° in the image. Figure 2.2 (b) shows the resulting geo-referenced image where the directions of streets now properly correspond to cardinal directions.



(a) Non-referenced satellite image



(b) Geo-referenced image

Figure: 2.2 Example of geo-referencing.

In geo-referencing of digital imagery, it is beneficial to choose groundel dimensions consistent with the pixel dimensions of the image. Therefore while geo-referencing a satellite

image with 10 m pixels, the ground size should also be 10 m. Otherwise more elaborate resampling methods are necessary for dimensions differing by more than a factor of about 1.5.

2.5 Selection of Ground Control Points

Selection of GCPs is an important step for geo-referencing. It is important to select a well-distributed pattern of GCPs, preferably with a point in each of the four corner and additional points spaced uniformly throughout the interior. It is also important to avoid choosing all Control Points (CPs) in a small cluster in one area of the image. In addition, if the affine or projective transformation is used, it is critical that the CPs should not lie along a straight line; otherwise the transformation becomes ill-conditioned and yields poor results. Depending on the transformation used and the required geometric accuracy, number of control points per image should be roughly 8 to 15 [65]. With a smaller number of CPs, accuracy is generally lower and it is difficult to detect errors present in the coordinates of one or more points [66]. For better accuracy, a large number of CPs are desirable; however, beyond 15 points, the marginal benefit of additional points outweighs the extra effort involved [67].

Geometric accuracy of a geo-referenced image is assessed through evaluation of the residuals from the transformation. These are always computed and evaluated. Large residuals indicate errors in measured image or ground coordinates. Root mean square (*rms*) of the residuals is one of the methods to get a nominal indication of the accuracy. It is also possible to compute a transformation with small residuals but still have low accuracy in terms of absolute position. This would occur if the ground coordinates are scaled from a map with significant systematic error. Probably the map was based on the NAD27 datum, but the

resulting geo-referenced image is assumed to be in the NAD83 datum. To remove the systematic errors of this type, it is advisable to perform a field test on a randomly selected sample of image points (checkpoints) using an independent source of higher accuracy, such as a Global Positioning System (GPS) survey. Amount of discrepancies between coordinates obtained from the geo-referenced image and the ones obtained from the higher-accuracy method may be used to assess accuracy.

2.6 Summary

In this chapter we described the geo-referencing method with the help of GCPs. Geo-referencing is generally considered as an ortho-rectification procedure. Using this technique, an RS image can be ground registered to its map or world coordinate system but it cannot geometrically correct each pixel location. The image is globally co-registered to its map coordinates (eastings and northings, or latitudes and longitudes) rather than pixel and line numbers. Advances in RS and HR satellite images have made it necessary to revise the geometric correction techniques used for ortho-rectification. Various methods from simple 2D polynomial models to rigorous mathematical models derived from digital photogrammetry are used for this problem. In such scenarios, conventional methods of photogrammetric modeling of RS images are insufficient for mapping purposes and need to be substituted with a more rigorous approach to get a true ortho-photo. To correct geometric distortions in images captured from spacecraft or aircraft, the process of geometric modeling becomes imperative.

Formulation of Pixel Projection Model

3.1 Introduction

Pixel Projection Model (PPM) has been devised by National Space Program Office (NSPO) Taiwan, for processing of Level-1 satellite images. This algorithm takes into account four vertices of the satellite image and geo-references these to ground coordinates. It uses WGS84 as geodetic model and extracts details of vertices from ancillary data of the image, available in DIMAP format. This model is used for processing FORMOSAT-2 images [68, 69]. Mission of FORMOSAT-2 is to capture daily images of Taiwan and its surrounding areas for disaster monitoring, land use and ocean surveillance during the 5-year mission life time. The image taken by the Remote Sensing Instrument (RSI) onboard is in the nadir direction, a swath width of 24 km and a field of regard of ± 45 degrees for along-track and cross-track viewing [70]. RSI provides images for 2 m Ground Sampling Distance (GSD) in Panchromatic (PAN) band and 8 m GSD in four Multi-Spectral (MS) bands over 24 km swath width in the nadir direction [71]. The high resolution requirement makes geometric correction more critical for the mission. Knowledge of the satellite navigation and information of the Digital Elevation Model (DEM) are insufficient for the geometric correction needs [72]. In this chapter, we first describe the FORMOSAT-2 satellite and its imaging instrument onboard known as RSI including its daily revisit orbit. Different factors affecting the image geometry are then explained and finally the mathematical formulation and description of PPM is elaborated.

3.2 FORMOSAT-2 Satellite

FORMOSAT-2 satellite was launched on May 21, 2004 by NSPO, Taiwan into the sun-synchronous orbit located at 891 kms above ground. Its successful operation proved the concept of HR satellite imagery. Temporal resolution can be improved by deploying a high spatial resolution sensor in a daily revisit orbit [73]. Technical specifications of FORMOSAT-2 are given in Table 3.1 [26]. These specifications make FORMOSAT-2 an ideal satellite for site surveillance [74]. However, sun-synchronous orbit with daily revisit schedule, large Instantaneous Field Of View (IFOV) and off-Nadir capabilities of RSI onboard FORMOSAT-2, give rise to new challenges in image processing.

Table: 3.1 Technical specifications of FORMOSAT-2 satellite.

Launch date: May 21, 2004		
Modes	Panchromatic	Multispectral
Spectral band	450-900 nm	blue: 450-520 nm green: 520-600 nm red: 630-690 nm near IR: 760-900 nm
Spatial resolution at nadir	2 m	8 m
File size (1A processing)	137 Mb	35 Mb
Maximum deviation off nadir	45°	
Swath width	24 km	
Data transfer rate to ground segment	120 Mbit/sec.	
Radiometric resolution	8 bits per pixel	
File format	GeoTIFF	
Processing	Radiometric, sensor and geometric correction Mapped to a cartographic projection	
Surveying frequency	Daily	
Stereopairs	None	
Order	7-14 days – archive 7-60 days – new collects	
Minimum order size	24 x 24 km (1 scene) – archive 24 x 24 km (1 scene) – new collects	

3.2.1 Remote Sensing Instrument (RSI)

The RSI onboard FORMOSAT-2 was built by EADS Astrium SAS, France [75]. It makes the FORMOSAT-2 imagery available for 2 m resolution in PAN and 8 m resolution in

four MS bands. It has scene coverage of 24×24 km. Table 3.2 gives the spectral range of each band [76]. FORMOSAT-2 is able to point to $\pm 45^\circ$ along track and $\pm 45^\circ$ across track [77].

Table: 3.2 Spectral bands of FORMOSAT-2 and their characteristics

Band	Spectral Range (μm)	Spatial Resolution (m)
B1	0.45-0.52	8
B2	0.52-0.60	8
B3	0.60-0.69	8
B4	0.76-0.90	8
PAN	0.45-0.90	2

The RSI is comprised of a monolithic linear Charged Coupled Device (CCD) array with 12000 pixels for PAN band and quad-linear CCD arrays with 3000 pixels for each MS band [78]. The individual MS CCD lines are shifted against the PAN CCD line combination in the sampling direction in the focal plane. Therefore, FORMOSAT-2 is able to take a much longer strip of image along its moving direction compared to the images taken by other high spatial resolution sensors [79]. However, the side effect of band-to-band mis-registration is also significant and visually obvious in the FORMOSAT-2 image. Taking the earth rotation and orbital instability into account, this effect is even more pronounced when satellite is operating in large angle ranges along and/or across track directions [80].

3.2.2 Daily Revisit Orbit

In a broad sense, the daily revisit orbit of FORMOSAT-2 is a special case of exactly repeating the sun-synchronous orbit with a period of one day. Rees provides a detailed derivation of a simple condition that must be fulfilled by this type of orbit [81].

$$\frac{P_n}{P'_E} = \frac{n_1}{n_2} \quad (3.1)$$

where, P_n is the nodal period

P'_E is one solar day of 24 h.

n_1 determines the time interval between successive opportunities to observe a given location.

n_2 governs the density of the sub-satellite tracks on the earth surface

In the case of FORMOSAT-2, to achieve daily revisit orbit ($n_1 = 1$) under the given condition of 14 sub-satellite tracks ($n_2 = 14$), P_n needs to be set at a value of 102.86 min. This is attained by placing FORMOSAT-2 at an altitude of 891 km with an inclination of 98.99° .

Although exactly repeating orbit is not a new idea, but FORMOSAT-2 is the first satellite with a high spatial resolution sensor placed in a daily revisit orbit. FORMOSAT-2 is able to capture any scene in its coverage area each day. In the mean time, each accessible scene can be systematically observed from the same angle under similar illumination conditions [82]. Figure 3.1 shows the accessible areas and the ground track of FORMOSAT-2 orbits with $\pm 45^\circ$ viewing angle across track (side looking) [83]. Table 3.3 gives the daily revisit number of the satellite and the corresponding area it covers.

Although the accessible area of the current FORMOSAT-2 orbit is limited in low latitude, this limitation can be removed by manipulating FORMOSAT-2 at a large viewing angle across the track. For example, in the event of tsunami in South Asia in 2004, NSPO increased the viewing angle to as high as $\pm 53^\circ$ and demonstrated that all areas can be imaged with a slight sacrifice in spatial resolution [84]. However, since the swath of FORMOSAT-2 imagery (24 km) is much less than the width of the accessible area during one overpass (more than 1500 km), only about 1.6% of the accessible areas in the shaded

region in Figure 3.1 are able to enjoy the continuous acquisition of images everyday. But if necessary, FORMOSAT-2 can be programmed to take daily images of the same site within its accessible area.

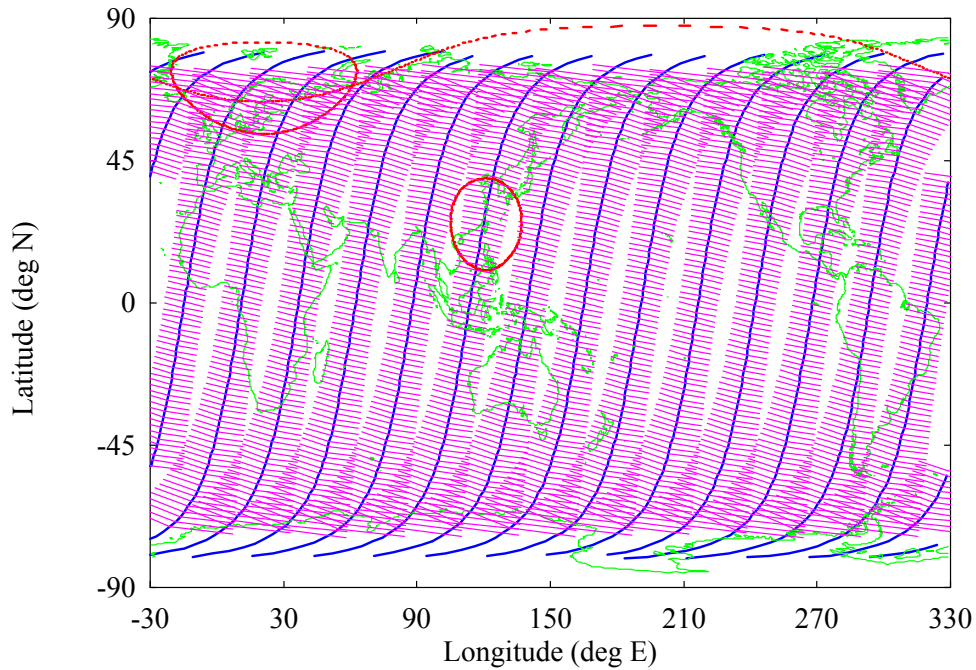


Figure: 3.1 RSI coverage and the daily revisit of FORMOSAT-2.

Table: 3.3 Areas covered by daily revisit

Daily Revisit No	Area Covered
1	Taiwan
2,3,4	Asia
5,6	Europe
7,8,9,10	America
11,12,13,14	Pacific

3.3 Factors Affecting Satellite Image Geometry

Several factors can affect satellite image geometry, such as the curvature and rotation of the earth, spacecraft speed, altitude and attitude, and properties of the scanner. The orbital velocity of the satellites can be considered constant but variations in platform altitude and

attitude cannot be assumed to be negligible. Major factors affecting the image geometry are spacecraft attitude, earth rotation and continental drift or nutation.

3.3.1 Parameters of Orbit Model

Orbits of most earth remote sensing satellites are nearly circular because a constant image scale is desired. The orbital velocity of satellites can be considered constant in time, for example 1.0153×10^{-3} radians/second for Landsat-1/ 2. Variations in platform altitude and ground speed cannot be assumed negligible [85, 86]. Platform attitude is critical to geometric precision because of the long “moment arm” of high altitude satellite pointing. A very small change in the pointing angle results in a large change in the viewed location on the ground. Attitude is expressed by three angles of platform rotation: roll, pitch and yaw, shown in Figure 3.2 [87].

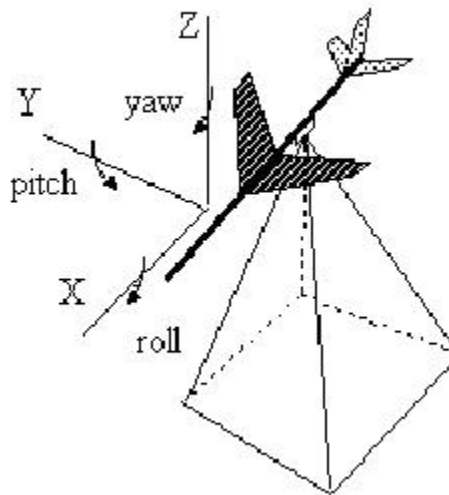


Figure: 3.2 Platform attitude angles.

3.3.2 Earth Model

Although geometric properties of earth are independent of sensors, they interact intimately via the orbital motion of the satellite. Two factors need consideration. Firstly, the

earth is not exactly a sphere but oblate described by Equation 3.2 and secondly the earth rotates at a constant angular velocity ω_e (given in Equation 3.3) while the satellite is moving along its orbit [88, 89].

$$\frac{p_x^2 + p_y^2}{r_{eq}^2} + \frac{p_z^2}{r_p^2} = 1 \quad (3.2)$$

where, (p_x, p_y, p_z) are the geocentric coordinates of any point P on the surface of the earth,

r_{eq} is the equatorial radius and

r_p is the polar radius.

The orbital velocity v_0 of satellite is computed using Equation 3.3 [90]:

$$v_0 = \omega_e r_e \cos \varphi \quad (3.3)$$

where, r_e is the radius of the earth

φ is the geodetic latitude.

ω_e is the angular velocity of the earth equal to $7.29211510 \times 10^{-5}$ radians/second.

3.4 Pixel Projection Modeling

Geometric modeling of a satellite image is necessary for finding the position of each pixel in geographical or map coordinate system. The direct geo-referencing method explained earlier in Chapter 2 is though useful for ortho-rectification but its importance is increased with the growing accuracy of satellite ancillary data [91, 92]. For example, the FORMOSAT-2 can provide position data with accuracy up to 20 m. In PPM the intersection of the sensor line-of-sight with the reference earth ellipsoid is found by applying a simple algorithm involving several coordinate transformations and basic geometry. Schematically it is shown in Figure 3.3 [93]. FORMOSAT-2 satellite ancillary data gives time of imaging in Universal Coordinated Time (UTC), spacecraft orbital position and velocity in Earth Center

Fixed (ECF) and Earth Center Inertial (ECI) frames. The procedure is independent of Digital Evaluation Model (DEM).

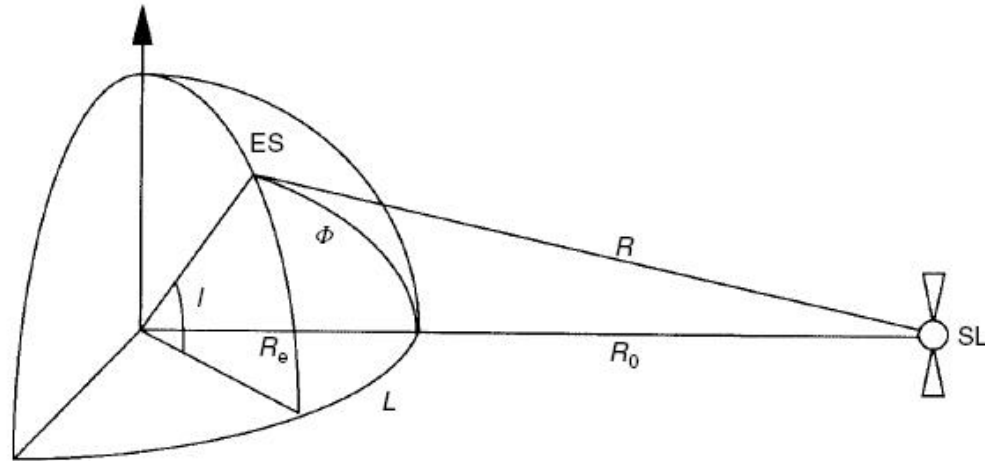


Figure: 3.3 Schematic for geo-referencing without DEM.

The pixel projection modeling in ECF is described as; computing the earth Rotation Matrix (RM) first. RM is based on the Julian day number (J2000) corresponding to the UTC time. With the help RM we can find Euler angles. The next step then is to transform Euler angles in the sequence of 1-2-3 from body frame (pointing) to Local Vertical Local Horizontal (LVLH) frame, from LVLH to ECI and then to ECF frame. In this way the corresponding “Body to ECF” transformation matrix is computed. After this transformation, sensor line-of-sight vector is transformed into ECF frame. Finally the coordinates (latitude, longitude and height) of the intersection of sensor line-of-sight vector and the earth ellipsoid surface based on WGS84 are found [94-96].

3.5 Mathematical Formulation of PPM

Steps involved in PPM have been explained qualitatively in Section 3.4. The primary aim of PPM is to transform the image recorded in CCD array to the ground coordinated

image (geo-referencing) and get a Level-2 image. The mathematical formulation of the method is explained in this section.

3.5.1 Position and Information of Satellite

Vehicle position and attitude is found directly from ancillary data. During processing of FORMOSAT-2 imagery, ancillary data is available in DIMAP format as a dim file. DIMAP format is a French format developed for recording earth observation satellite data. Ancillary data needs some interpolations for its subsequent utilization in any application software [97].

Generally, the imaging satellite is moving along a well defined close-to-circular elliptical orbit. Figure 3.4 shows the relationships between satellite position in orbit and ground position on the earth [93].

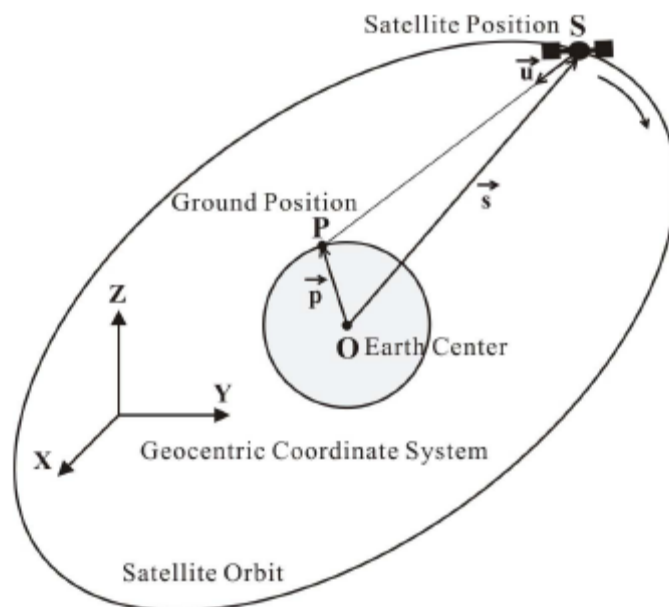


Figure: 3.4 Relationship between ground and satellite positions.

The position vector, \vec{p} is the displacement vector from earth center to a point P on earth, \vec{u} is LOS (line-of-sight) vector and satellite position vector \vec{s} is the vector of the distance between satellite position S and earth center O . These vectors satisfy Equation 3.4.

$$\vec{p} - \vec{s} = \mu \vec{u} \quad (3.4)$$

where μ is an arbitrary constant [97, 98].

The relationship between satellite position in orbit and ground position on the earth helps to understand the geometry of recorded imagery. Further analysis of satellite position let us know the exact attitude angles on which it is present in the orbit at the time of recording an image. These attitude angles are articulated as Euler angles.

3.5.2 Rotation Matrix (RM) and Euler Angles

In PPM, the attitude is found with the help of rotation matrix which is made up of Euler's angles. Equation 3.5 gives x_b , y_b and z_b components of the body frame (recording platform), derived from the x_l , y_l and z_l components of LVLH plane of line of sight vector. Whereas, Equation 3.6 defines RM. RM is the combined matrix of Euler's angles.

$$\begin{pmatrix} x_b \\ y_b \\ z_b \end{pmatrix}_{Body} = R_1(\phi)R_2(\theta)R_3(\psi) \begin{pmatrix} x_l \\ y_l \\ z_l \end{pmatrix}_{LVLH} \quad (3.5)$$

$$R_1(\phi)R_2(\theta)R_3(\psi) =$$

$$\begin{pmatrix} \cos\theta\cos\psi & \cos\theta\sin\psi & -\sin\theta \\ -\cos\phi\sin\psi + \sin\phi\sin\theta\cos\psi & \cos\phi\cos\psi + \sin\phi\sin\theta\sin\psi & \sin\phi\cos\theta \\ \sin\phi\sin\psi + \cos\phi\sin\theta\cos\psi & -\sin\phi\cos\psi + \cos\phi\sin\theta\sin\psi & \cos\phi\cos\theta \end{pmatrix} \quad (3.6)$$

where, x_b , y_b and z_b are x , y and z components of the body frame

x_l, y_l and z_l are $x, y,$ and z components of LVLH plane

ϕ, θ and ψ are roll, pitch and yaw angles respectively.

R represents the basic matrix.

Orthogonal RM is formed by the successive multiplication of three basic matrices $R_1(\phi), R_2(\theta)$ and $R_3(\psi)$. $R_1(\phi), R_2(\theta)$ and $R_3(\psi)$ are the basic matrices of roll, pitch and yaw angles about spacecraft central orbital axis. Their specific details are available in [99]. The matrix-multiplication given in Equation 3.5 transforms the LVLH frame to the body frame. The transformation matrix from the body frame to the LVLH frame is obtained by transposing the matrix. The inverse relationship can be found because of orthogonality, i.e. the inverse matrix is equivalent to its transpose.

ECF frame is determined after calculating LVLH frame. It is a process of coordinate transformation from orbit to earth-centered coordinates in inertial space. Two-dimensional array vectors are obtained by this transformation using the spacecraft movement. The array dimension for one observation depends on the observation period, that is, the number of pixels in the along-track direction. The process is carried out by using position and velocity information from the ancillary data. Effects of the Precession and the Nutation are taken into account for accurate geographical location from the ancillary data. These factors are important because the spacecraft position information is based on the Julian Day (J2000) coordinate frame [100]. J2000 coordinate frame are the earth inertial coordinates at noon of January 1st, 2000 [101]. The line of sight vectors in the LVLH or orbital reference coordinate frame are converted to the ECF frame expression as illustrated by Equations 3.7 to 3.11.

$$\begin{pmatrix} \hat{e}_{x_l} \\ \hat{e}_{y_l} \\ \hat{e}_{z_l} \end{pmatrix} = \begin{pmatrix} b_{11} & b_{12} & b_{13} \\ b_{21} & b_{22} & b_{23} \\ b_{31} & b_{32} & b_{33} \end{pmatrix} \begin{pmatrix} \hat{e}_{x_r} \\ \hat{e}_{y_r} \\ \hat{e}_{z_r} \end{pmatrix} \quad (3.7)$$

$$\hat{e}_{x_l} = \hat{e}_{y_l} \times \hat{e}_{z_l} \equiv b_{11}\hat{e}_{x_r} + b_{12}\hat{e}_{y_r} + b_{13}\hat{e}_{z_r} \quad (3.8)$$

$$\hat{e}_{y_l} = -\bar{h}_{ECF} / |\bar{h}_{ECF}| \equiv b_{21}\hat{e}_{x_r} + b_{22}\hat{e}_{y_r} + b_{23}\hat{e}_{z_r} \quad (3.9)$$

$$\hat{e}_{z_l} = -\bar{r}_{ECF} / |\bar{r}_{ECF}| \equiv b_{31}\hat{e}_{x_r} + b_{32}\hat{e}_{y_r} + b_{33}\hat{e}_{z_r} \quad (3.10)$$

$$\bar{h}_{ECF} = \bar{r}_{ECF} \times (\bar{v}_{ECF} + \omega_e \hat{e}_{z_r} \times \bar{r}_{ECF}) \quad (3.11)$$

where, $\omega_e = 7.29211510 \times 10^{-5}$ rad/sec is the earth rotation rate.

v and r in Equation 3.7 represent velocity and distance or position of spacecraft from the earth respectively, expressed in the ECF frame [102].

x , y and z are unit vector components of axes of the orbit coordinate frame (e_{x_r} , e_{y_r} and e_{z_r}) are expressed in ECF coordinate frame (e_{x_l} , e_{y_l} and e_{z_l}).

3.5.3 Pixel Line-of-Sight (LOS) Vector from Recording Platform (Body) to ECF

To determine the LOS vector, first direction or angle of view ψ to be found from recording platform to ground location of a particular area. To find out view direction in body frame that is from the linear CCD array image plane (recording platform) to ground location, Figures 3.5 and 3.6 demonstrate view angle ψ . Total numbers of pixels are assumed as $2n$, so that its half equals n with a total half view angle of β . The view angle of pixels is defined by the boundary conditions given in Equation 3.12.

$$\psi = \tan^{-1}\left[\left(\frac{i-n-1}{n}\right)\beta\right] \quad \text{for } i = 1, 2, \dots, 2n+1 \quad (3.12)$$

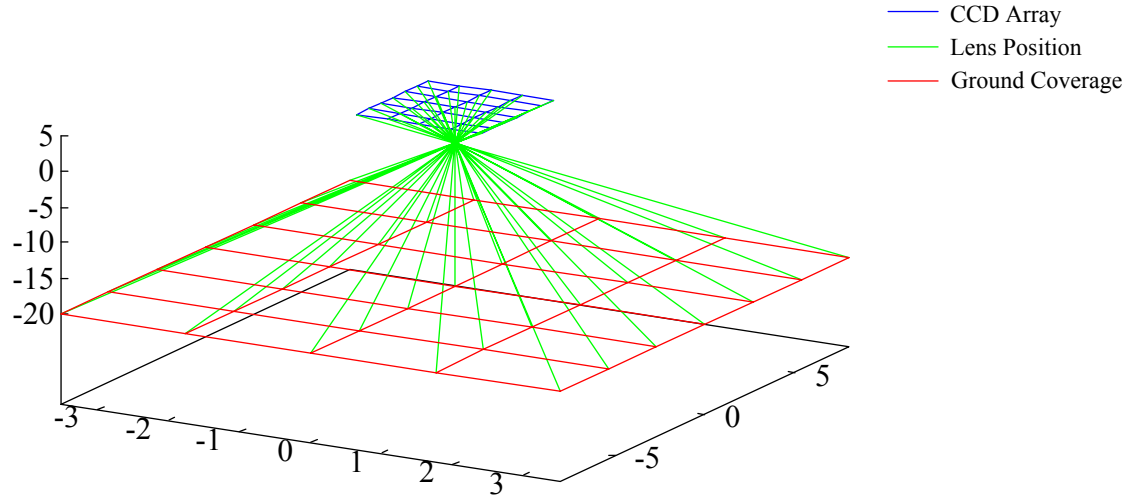


Figure: 3.5 Geometry of a digital CCD array.

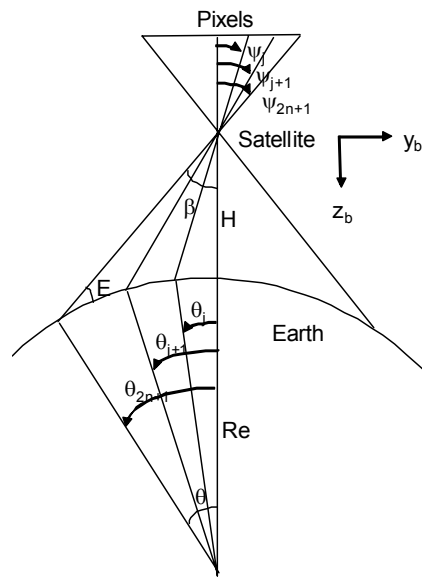


Figure: 3.6 Geometry of satellite and earth line of sight vector.

While knowing the viewing angle, the corresponding view direction q is calculated by Equation 3.13.

$$q = \frac{k + \tan \psi}{\sqrt{1 + \tan^2 \psi}} \quad (3.13)$$

Similarly the relationship of view angle in x and y directions is obtained for 2-D planar CCD array. Equation 3.14 gives x component and Equation 3.15 y component of the view angle.

$$\psi_x = \tan^{-1}\left[\left(\frac{i-m-1}{m}\right)\alpha\right] \text{ for } i = 1, 2, \dots, 2m+1 \quad (3.14)$$

$$\psi_y = \tan^{-1}\left[\left(\frac{j-n-1}{n}\right)\beta\right] \text{ for } j = 1, 2, \dots, 2n+1 \quad (3.15)$$

$$q = \frac{k + \tan \psi_y + \tan \psi_x}{\sqrt{1 + \tan^2 \psi_y + \tan^2 \psi_x}} \quad (3.16)$$

where, i and j indices indicates the corresponding components in CCD plane.

m and n are the total number of pixels in each direction.

View direction q given in Equation 3.16 is for a 2-D CCD array. Further details on computation of the angle and view direction are available in [103-107].

Once view angle and view direction from CCD array to earth centric system are known, transformation of image pixel values can be performed. For transformations from the body frame to LVLH and ECF, image resampling techniques are adopted. Four resampling techniques are explained in Chapter 5. Details of three conventional interpolation techniques are given in Appendix B.

3.5.4 Intersection of Recording Platform LOS Vector and the Geodetic Surface

Projection is a protocol to project image of an imaginary three-dimensional object on a plane surface. A map-projection is any method used in cartography (mapmaking) to represent the two-dimensional curved surface of the earth or other body on a plane. PPM derives projection parameters which in case of RS are latitude, longitude and height from the intersection of sensor line-of-sight vector and the geodetic surface. Figure 3.7 shows projection of a point p to its geodetic coordinates. Coordinates of p are derived from the Instantaneous Field Of View (IFOV) of satellite imaging system's pixel in ECF.

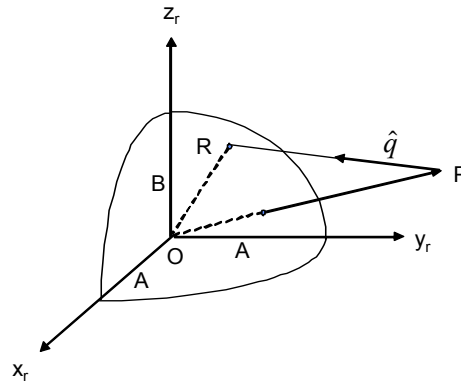


Figure: 3.7 Projection of a point to geodetic surface.

The earth surface projection \overline{OR} of a view direction vector q is given by Equation 3.17. Geodetic coordinate system, geocentric coordinates and local vertical coordinates of map projections are given in details in [107-110]).

$$\overline{OR} = \overline{OP} + s\hat{q} \equiv (a, b, c) + s(d, e, f) \equiv X, Y, Z \quad (3.17)$$

where, a, b, c are components of point R , and

d, e, f are components of point P .

X, Y, Z are the geocentric components.

The only unknown quantity in Equation 3.17 is s . Scalar quantity s must satisfy Equation 3.18.

$$\frac{X^2}{A^2} + \frac{Y^2}{A^2} + \frac{Z^2}{B^2} = 1 \quad (3.18)$$

where, A is equivalent to radius of the earth,

B is the minor axis and is calculated as $A(1-f)$,

The flattening of earth f is $1/298.26$, f can be calculated as $1-b/a$.

It is important to note that two constant quantities are required to define the size and shape of a reference ellipsoid. These are the semi-major axis of the ellipsoid A and the flattening f . From these two defining constants, other parameters can be derived.

From Equations 3.17 and 3.18, we obtain Equation 3.19.

$$\left(\frac{d^2}{A^2} + \frac{e^2}{A^2} + \frac{f^2}{B^2}\right)s + 2\left(\frac{ad}{A^2} + \frac{be}{A^2} + \frac{cf}{B^2}\right)s + \left(\frac{a^2}{A^2} + \frac{b^2}{A^2} + \frac{c^2}{B^2} - 1\right) = 0 \quad (3.19)$$

Further simplification leads to Equation 3.20.

$$s = \frac{-\left(\frac{ad}{A^2} + \frac{be}{A^2} + \frac{cf}{B^2}\right) - \sqrt{\left(\frac{ad}{A^2} + \frac{be}{A^2} + \frac{cf}{B^2}\right)^2 - \left(\frac{d^2}{A^2} + \frac{e^2}{A^2} + \frac{f^2}{B^2}\right)\left(\frac{a^2}{A^2} + \frac{b^2}{A^2} + \frac{c^2}{B^2} - 1\right)}}{\left(\frac{d^2}{A^2} + \frac{e^2}{A^2} + \frac{f^2}{B^2}\right)} \quad (3.20)$$

The scalar quantity s obtained in Equation 3.20 is the scale factor. The scaling in pixel position is the result of change in sensors LOS vector. The scaling factor is used to determine the new location of pixel intensity. The remaining quantities, geodetic latitude and altitude, are given by ϕ and h respectively, in Figure 3.8.

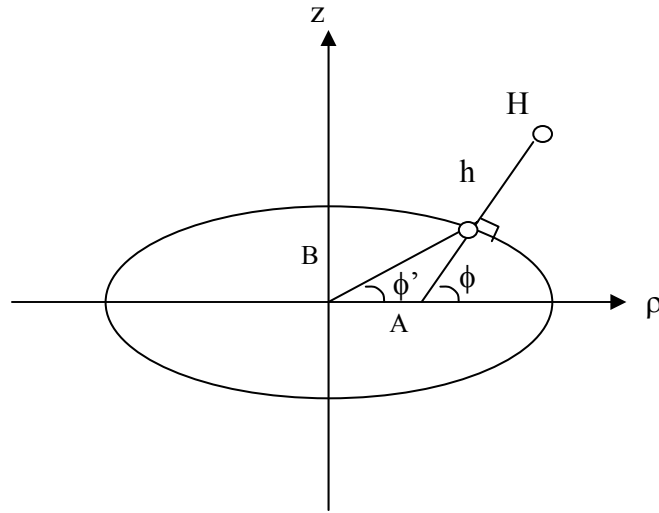


Figure: 3.8 Geodetic latitude and altitude of a point.

Equation 3.18 is derived from three dimensions of geocentric coordinates. Conversion of ground coordinates to image coordinates (being 2-D) only two parameters are required, that is latitude and altitude [111]. Thereby Equation 3.18 is reduced to Equation 3.21.

$$\frac{\rho^2}{A^2} + \frac{z^2}{B^2} = 1 \quad (3.21)$$

Relationship between the ellipsoid constants, the semi-major axis A , the semi-minor axis B , the flattening f , the first eccentricity e and the second eccentricity e' is given by Equations 3.22 to 3.26.

$$A = R_e \quad (3.22)$$

$$B = A(1 - f) \quad (3.23)$$

$$f = 1 - \frac{B}{A} \quad (3.24)$$

$$e = \frac{\sqrt{A^2 - B^2}}{A} \quad (3.25)$$

$$e' = \frac{A^2 - B^2}{A^2} \quad (3.26)$$

Differentiating Equation 3.21, we get

$$\frac{2\rho d\rho}{A^2} + \frac{2zdz}{B^2} = 0 \quad (3.27)$$

Which can be further reduced simplified

$$-\frac{d\rho}{dz} = \frac{z}{\rho} \frac{A^2}{B^2} \quad (3.28)$$

From Figure 3.7 latitude ϕ , is given by

$$\tan \phi = \tan \phi' \left(\frac{A^2}{B^2} \right) \quad (3.29)$$

Simplifying Equation 3.28 and 3.29, gives

$$\tan \phi = \frac{z_H - h \sin \phi}{\rho_H - h \cos \phi} \quad (3.30)$$

Using geodetic latitude ϕ , altitude of a point H is given by

$$h = \frac{\rho_H}{\cos \phi} - AC \quad (3.31)$$

where, C is a constant derived from the values of A , B and ϕ ,

$$C = \frac{1}{\sqrt{1 - \left(1 - \frac{B^2}{A^2}\right) \sin^2 \phi}} \quad (3.32)$$

After knowing values of latitude and altitude of a point, the intersection vector from sensor platform to geodetic surface is found. Required data to transform recorded image in

CCD array to the ground coordinated image is obtained by combining all the known quantities like position of the satellite, attitude angles, view direction, LOS vector from recording platform to ECF and intersection of recording platform vector with the geodetic surface. Pixel projection modeling is completed in this way and a geodetically transformed image is achieved.

3.6 Summary

FORMOSAT-2 provides a new source of remote sensing data with high-spatial and high-temporal resolutions. Using image processing technique described in this chapter, raw (Level-1) images of FORMOSAT-2 satellite are successfully converted to radiometrically corrected images. Radiometric corrections of HR images are called Level-2 image products. If DEM data of the same scene is available, it can be added into this procedure to get more accurate results.

FORMOSAT-2 satellite, RSI and daily revisit orbit characteristics, factors affecting FORMOSAT-2 imagery and parameters of the orbital and earth models have been described in this chapter. Mathematical formulation involved in PPM was also discussed in details. The numerical procedure explicated can be termed as PPM Version 1. The outcome of this version is Level-2 FORMOSAT-2 images.

Level-3 Geometric Correction of FORMOSAT-2 Images

4.1 Introduction

Remotely sensed images are available as geometric products. The images range from original sensor images that are improved from spacecraft orientation distortions (Level-1A products) to a more geometrically corrected images (Level-2 products) and even to ortho-rectified images. Different mathematical models are used for their processing [112-117]. Similarly different solutions are used for their improvements [118-122]. The solutions include from a mere shift in X and Y coordinates not taking advantages from the given sensor orientation to feature and contour matching using sophisticated image processing techniques [123-128].

Pixel projection method (PPM) has been devised by National Space Program Office (NSPO) Taiwan, for processing of Level-1A satellite images. The algorithm and its mathematical formulations have been explained in Chapter 3. The model has been used for processing of FORMOSAT-2 images to get a Level-2 image. Corrections obtained with it were global in nature. There was a dire need of improvement of PPM to achieve local geometric corrections to be classified as Level-3 geometric corrections. Development of an algorithm for Level-3 corrections especially for FORMOSAT-2 images is the core of this research work. For this task test Images and their ancillary data for development of the algorithm have been provided by NSPO.

In this chapter, test images and their ancillary data provided by NSPO are discussed.

Level-3 geometric correction method including GCPs integration and projection by least square regression is then described in detail.

4.2 Test Images and Ancillary Data

Test images 1 and 2 shown in Figure 4.1 (a) and (b), respectively were obtained from FORMOSAT-2 (courtesy NSPO). Test image 1 represents general area south of Islamabad (1500 x 2100 pixels); image was taken on 28th Oct 2005. Test image 2 represents northern part of Abbottabad (1500 x 3600 pixels). The image was taken on 9th Oct 2005, one day after the severe earthquake that struck northern parts of Pakistan. Ancillary data of FORMOSAT-2 imagery is available in DIMAP format. The file containing data of orbit, spacecraft, imaging instrument and digital imagery is called a dim file. A portion of dim file is shown in Figure 4.2. DIMAP is the French format developed for recording earth observation satellite data [129,130]. Important features of the ancillary data extracted from the dim file are given in Table 4.1.



(a) Test image1 showing area south of Islamabad (b) Test image2 showing North of Abbottabad.

Figure: 4.1 FORMOSAT-2 images obtained from NSPO for testing purpose

Column 1	Column 2
<pre> <Vertex> <FRAME_COL>1</FRAME_COL> <FRAME_ROW>1</FRAME_ROW> <FRAME_LAT>33.6024688432</FRAME_LAT> <FRAME_LON>72.9952789098</FRAME_LON> </Vertex> <Vertex> <FRAME_COL>3000</FRAME_COL> <FRAME_ROW>1</FRAME_ROW> <FRAME_LAT>33.5606169587</FRAME_LAT> <FRAME_LON>73.2569736999</FRAME_LON> </Vertex> <Vertex> <FRAME_COL>3000</FRAME_COL> <FRAME_ROW>4200</FRAME_ROW> <FRAME_LAT>33.2616531440</FRAME_LAT> <FRAME_LON>73.1658818972</FRAME_LON> </Vertex> <Vertex> <FRAME_COL>1</FRAME_COL> <FRAME_ROW>4200</FRAME_ROW> <FRAME_LAT>33.3033274536</FRAME_LAT> <FRAME_LON>72.9050641147</FRAME_LON> </Vertex> <Raw_Ephemeris> <Point_List> <Point> <Location> <X>1828294.00000000</X> <Y>5902847.00000000</Y> <Z>3824494.00000000</Z> </Location> </Point> </Point_List> </Raw_Ephemeris> </pre>	<pre> </Location> <Velocity> <X>2878.22070312</X> <Y>3127.56884766</Y> <Z>-6184.44531250</Z> </Velocity> <TIME>2005-10-28 5:18:0.00000</TIME> </Point> </Point_List> </Raw_Ephemeris> <Corrected_Attitudes> <ECF_Attitude> <Angles> <ROLL>-1.20524</ROLL> <PITCH>-0.31914</PITCH> <YAW>1.85932</YAW> </Angles> </ECF_Attitude> </Corrected_Attitudes> 5:18:0.00000</TIME> </Angles> </ECF_Attitude> </Corrected_Attitudes> </Instrument_Look_Angles_List> <Instrument_Biases> <ROLL>-15797000E-03</ROLL> <PITCH>-65795700E-02</PITCH> <YAW>-15776000E-02</YAW> </Instrument_Biases> <REFERENCE_BAND>1</REFERENCE_BAND> <REFERENCE_TIME>2005/10/28 5:18:0.50870</REFERENCE_TIME> <REFERENCE_LINE>1</REFERENCE_LINE> <LINE_PERIOD>1.2344e-03</LINE_PERIOD> </pre>

Figure: 4.2 Portion of a dim file presenting ancillary data of RS image

Table: 4.1 Ancillary data of the test images

META DATA	Test Image 1	Test Image 2
METADATA_FORMAT	DIMAP	DIMAP
METADATA_PROFILE	F2_Level_1A	F2_Level_1A
DATASET_NAME	FS2_112627000_1A_0001_M S	FS2_114586000_01_0001_ MS
COPYRIGHT	COPYRIGHT 2004/09	COPYRIGHT 2004/09
SCENE_ORIENTATION	194.22	194.18
DATASET_PRODUCER_NAME	NSPO	NSPO
DATASET_PRODUCER_URL	http://www.nspo.org.tw	http://www.nspo.org.tw
IMAGING_DATE	2005/10/28	2005/10/09
PRODUCT_INFO	FORMOSAT2 Product Level1A MS	FORMOSAT2 Product Level1A MS
RASTER DIMENSIONS		
No of Columns	3000	1500
No of Rows	4200	3600
PROCESSING_LEVEL	1A	1A
HORIZONTAL_CS_NAME	WGS 84	WGS 84

Both the test images were processed and geo-referenced using pixel projection method. The Level-2 output images are shown in Figure 4.3. Pixel projection method takes into account WGS84 world geodetic system for geo-referencing satellite data to an earth coordinate system. The test images were primarily ortho-corrected selecting vertices from the ancillary data.

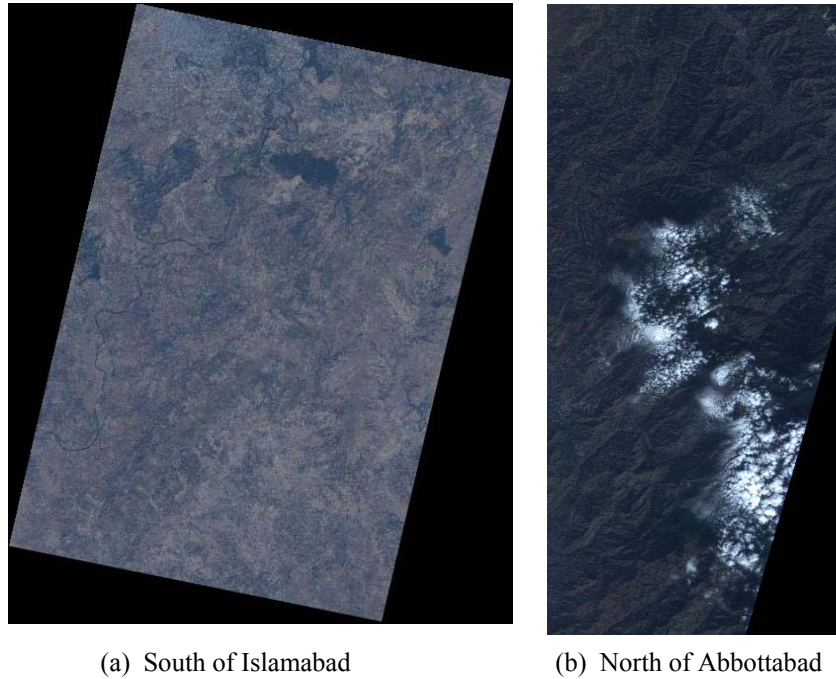


Figure: 4.3 Geometrically corrected images using pixel projection method

4.3 Level-3 Geometric Correction Technique

Different levels of correction for FORMOSAT-2 imagery and corresponding terminologies used by other remote sensing satellite processors have been tabulated in Table 1.1. Up to Level-2, image is said to be radiometrically corrected. Level-3 geometric correction technique is an extension of PPM. The changes made and the improvements achieved in the method are described in this section.

4.3.1 Geo-referencing Based on Pixel Projection Model (PPM)

Level-1A FORMOSAT-2 image is geo-referenced and resampled to obtain a Level-2 image. Procedural steps involved in geo-referencing FORMOSAT-2 images based on pixel projection method are shown in Figure 4.4. These steps include obtaining information about image from satellite ancillary data. Pixel location of recorded image is denoted by $\bar{r}' = \bar{f}'(m, n)$. Image pixels are assigned new pixel location through inverse projection as per ground coordinate system that is $\bar{r}' = \bar{f}'(j', k')$. Then interpolation by bilinear or cubic convolution methods is applied for pixel transformation $\bar{s}' = \bar{g}'(j', k')$. Finally the new image is filled up with pixel values $\bar{s}' = \bar{g}'(m, n)$.

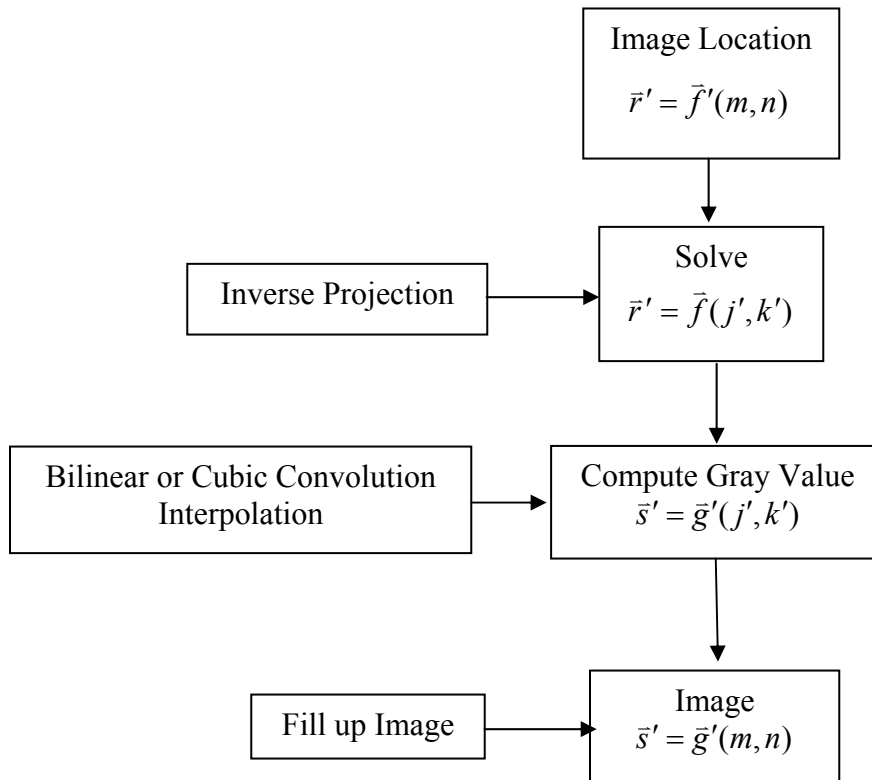


Figure: 4.4 Geo-referencing with PPM

4.3.2 Integration of GCPs

In the original PPM, image is geo-referenced without integrating GCP's from the map. Only vertices of the images are used to match the ground coordinates from the ancillary data. But in the new approach, besides geo-referencing with 4 vertices, further refinement is made by selecting GCPs from Google Earth software for precise geo-referencing. The coordinates of these points are then provided to the pixel projection application. This has made geo-referencing more accurate. Geodetic model WGS84 has been used for image projection. Procedural steps used for geo-referencing using GCPs are shown in Figure 4.5. Steps involved in this process comprise selection and matching of GCPs between remotely sensed image and the Google Earth. Locations of these points are provided to pixel projection application denoted by $\bar{r}_G = \bar{f}_G(j, k)$. Before inverse projection, attitude angles or instrument bias (ϕ, θ, φ) is solved with the help of least square method to get the exact location of pixels. This newly found location is represented with \bar{r}' , where $\bar{r}' = \bar{f}'(j', k')$. Among four interpolation techniques (nearest neighbor, bilinear interpolation, cubic convolution or Daubechies-4 wavelet based method) any one technique is selected for pixel transformation and resampling [131]. Finally image is filled up with pixel values $\bar{s}' = \bar{g}'(m, n)$.

Test image 1 was geometrically corrected for verification of the new technique. For simplicity only 6 GCPs were selected. The corresponding GCPs from Google Earth were manually selected. The GCPs alongwith their corresponding x and y image coordinates and ground coordinates from Google Earth (in degrees) for geo-referencing are given in Table 4.2. The integration of GCPs with vertices of image gives precision in image registration.

In subsequent step, the method of discovering exact pixel location is elaborated for which least squares approximation technique is employed.

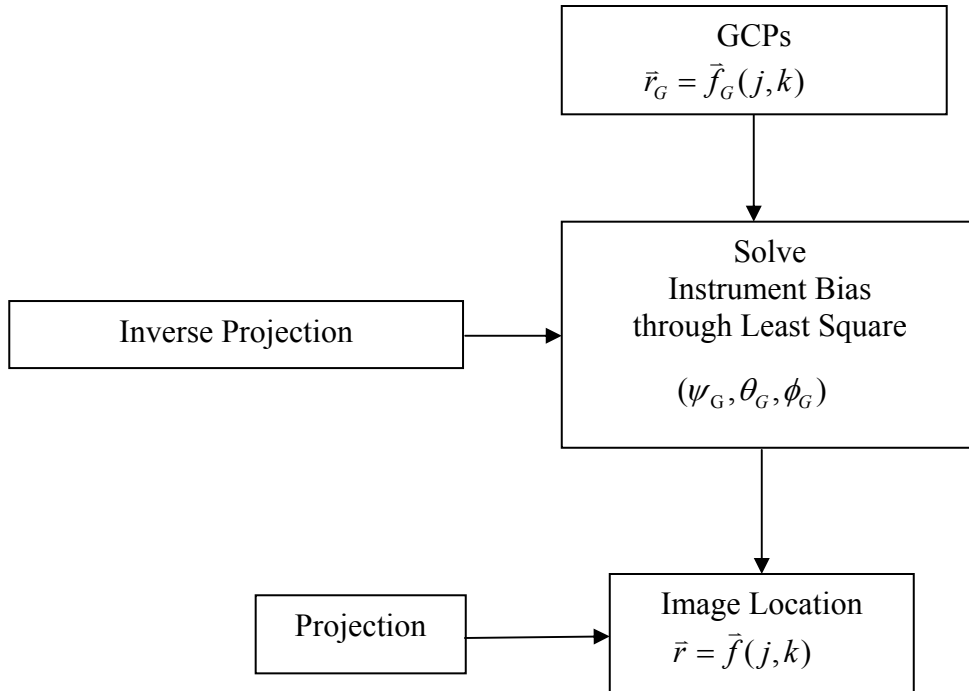


Figure: 4.5 GCPs integration in PPM

Table: 4.2 Image coordinates with corresponding location coordinates

Point No	Image Line (x)	Image Sample (y)	Location Lon	Location Lat
1	148	119	73°3'15"	33°30'13"
2	169	138	73°3'49"	33°29'14"
3	217	124	73°2'45"	33°27'43"
4	217	76	73°0'44"	33°28'1"
5	425	43	72°57'15"	33°21'11"
6	148	344	73°12'44"	33°28'29"

4.3.3 Projection by Least Squares Regression

Least squares normal equations are more easily understood and manipulated in matrix representation. Normal equations of least squares (given in Appendix C) are converted into

matrix notation. Generally least squares equation in matrix form for equally weighted observations is given by Equation 4.1.

$$(A^T A)X = A^T L \quad (4.1)$$

In Equation 4.1, $A^T A$ is the matrix of normal equation coefficients of the unknowns. Multiplying both side of the equation by $(A^T A)^{-1}$ and simplifying give Equation 4.2

$$X = (A^T A)^{-1}(A^T L) \quad (4.2)$$

Equation 4.2 is the basic least squares matrix equation for equally weighted observations. The matrix X consists of most probable values for unknowns $X_1, X_2, X_3, \dots, X_n$. L denotes the observations, i.e known values [132]. In the algorithm of Level-3 PPM, GCPs are the set of unknown observations. Values of GCPs in terms of latitudes and longitude have been calculated in previous section and are incorporated in the least squares equations.

Assuming that GCPs are expressed as (lon_1, lat_1) , (lon_2, lat_2) and attitude as (ϕ, θ, ψ) , the functions f and g , the projection longitude and latitude from the pixel to a GCP, are given by Equations 4.3, 4.4, 4.5 and 4.6 respectively.

$$f_1(\phi, \theta, \psi) = lon_1 \quad (4.3)$$

$$g_1(\phi, \theta, \psi) = lat_1 \quad (4.4)$$

$$f_2(\phi, \theta, \psi) = lon_2 \quad (4.5)$$

$$g_2(\phi, \theta, \psi) = lat_2 \quad (4.6)$$

The least squares regression is written as Equation 4.7.

$$Min h(\phi, \theta, \psi) = \sum_{i=1}^2 [(f_i - lon_i)^2 + (g_i - lat_i)^2] \quad (4.7)$$

Equation 4.7 though gives solution of least squares regression but practical solution for instrument bias determination is complicated and not yet completed. The fact of $Min h$ of

three angles is a highly non-linear function of the unknown vectors in this case $(\phi_0, \theta_0, \varphi_0)$. The solution given in Equation 4.7 is required to be linearized by derivation and expansion process for their ensuing use in finding matrix of coefficients of unknown and final solution of least squares adjustments. These steps are further elaborated in subsequent sub-sections.

4.3.3.1 Linearization of Equation for Attitude Determination

To determine the maximum value of a desirable property of a multi-spectral image, such as signal to noise ratio or spread in intensity, derivatives of vectors are taken. Partial derivative of a vector in two dimensions is written as $\frac{\partial}{\partial x}$. Most of the operations with vector derivatives correspond exactly to the operations with ordinary scalar derivatives. This can be verified by writing the expressions, component by component, as given in Equations 4.8 and 4.9.

$$\frac{\partial}{\partial x}(x^T y) = y \Leftrightarrow \frac{\partial}{\partial x} xy = y \quad (4.8)$$

$$\frac{\partial}{\partial x}(x^T x) = 2x \Leftrightarrow \frac{\partial}{\partial x} x^2 = 2x \quad (4.9)$$

Similarly for a scalar expression with a constant matrix A, partial derivative is given by Equation 4.10.

$$\frac{\partial}{\partial x}(xAy) = Ay \Leftrightarrow \frac{\partial}{\partial x} x^2 A = 2Ax \quad (4.10)$$

Let x_0 be the critical point of a function $f(x)$, then Equation 4.11 gives the derivative around that point.

$$\frac{d}{dx} f(x_0) = \left. \frac{d}{dx} f(x) \right|_{x=x_0} = 0 \quad (4.11)$$

As shown in Figure 4.6, $f(x_0)$ is a local minimum if $\frac{d^2}{dx^2} f(x_0) > 0$.

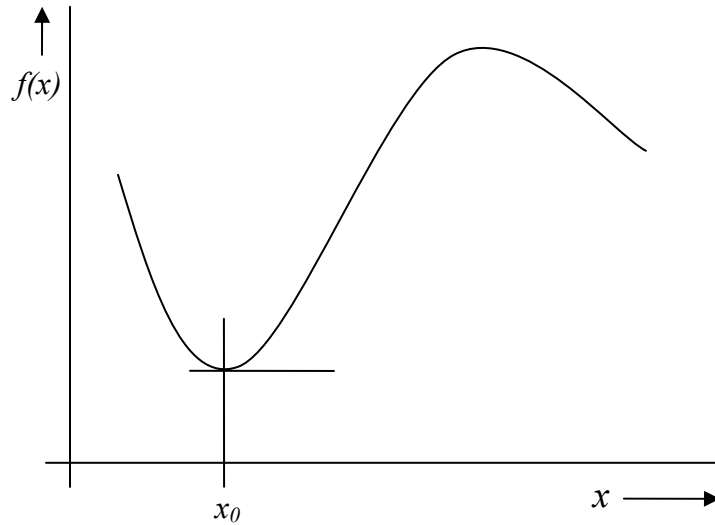


Figure: 4.6 A function of one variable

This becomes obvious if we express $f(x)$ as a Taylor series about x_0 .

$$f(x) = f(x_0) + (x - x_0) \frac{d}{dx} f(x_0) + (x - x_0)^2 \frac{d^2}{dx^2} f(x_0) + \dots \quad (4.12)$$

In case of satellite attitude there are three variables. The three angles roll, yaw and pitch denoted by ψ , θ and ϕ respectively represent the attitude. So to find minima about a point as per Taylor series, Equation 4.12 is written as.

$$f(x, y, z) = f(x_0, y_0, z_0) + (x - x_0) \frac{d}{dx} f(x_0) + (y - y_0) \frac{d}{dy} f(y_0) + (z - z_0) \frac{d}{dz} f(z_0) + \dots \quad (4.13)$$

Now consider the complex case of linearization of having three variables and two different functions. For simplicity only two points are considered for solving a problem of determination of attitude of satellite or instrument bias of a spacecraft. Equations 4.14 to 4.17 are obtained after manipulation for three variables. In this case, derivative is taken with

respect to the three variables (ϕ, θ, ψ) . This is more easily solvable if $f(\phi, \theta, \psi)$ is expressed as a Taylor series about $(\phi_0, \theta_0, \psi_0)$.

$$f_1(\phi, \theta, \psi) + \frac{\partial f_1}{\partial \phi}(\phi - \phi_0) + \frac{\partial f_1}{\partial \theta}(\theta - \theta_0) + \frac{\partial f_1}{\partial \psi}(\psi - \psi_0) = lon_1 \quad (4.14)$$

$$g_1(\phi, \theta, \psi) + \frac{\partial g_1}{\partial \phi}(\phi - \phi_0) + \frac{\partial g_1}{\partial \theta}(\theta - \theta_0) + \frac{\partial g_1}{\partial \psi}(\psi - \psi_0) = lat_1 \quad (4.15)$$

$$f_2(\phi, \theta, \psi) + \frac{\partial f_2}{\partial \phi}(\phi - \phi_0) + \frac{\partial f_2}{\partial \theta}(\theta - \theta_0) + \frac{\partial f_2}{\partial \psi}(\psi - \psi_0) = lon_2 \quad (4.16)$$

$$g_2(\phi, \theta, \psi) + \frac{\partial g_2}{\partial \phi}(\phi - \phi_0) + \frac{\partial g_2}{\partial \theta}(\theta - \theta_0) + \frac{\partial g_2}{\partial \psi}(\psi - \psi_0) = lat_2 \quad (4.17)$$

The three angles (ϕ, θ, ψ) of instrument bias are unknown values of least square regression, their coefficients are given in Equations 4.14 to 4.17, which are $\frac{\partial f_1}{\partial \phi}$, $\frac{\partial f_1}{\partial \theta}$, $\frac{\partial f_1}{\partial \psi}$ for

lon_1 , $\frac{\partial g_1}{\partial \phi}$, $\frac{\partial g_1}{\partial \theta}$, $\frac{\partial g_1}{\partial \psi}$ for lat_1 , $\frac{\partial f_2}{\partial \phi}$, $\frac{\partial f_2}{\partial \theta}$, $\frac{\partial f_2}{\partial \psi}$ for lon_2 and $\frac{\partial g_2}{\partial \phi}$, $\frac{\partial g_2}{\partial \theta}$, $\frac{\partial g_2}{\partial \psi}$ for lat_2 . These

are the desired values used in finding matrix of coefficient of unknowns which eventually lead to the solution of least squares adjustments.

4.3.3.2 Finding Matrix of Coefficients of Unknowns

A is the matrix of coefficients of the unknown in Equations 4.1 and 4.2. It is expressed as Equation 4.18 in matrix form (refer to Appendix C for details)

$${}_m A^n = \begin{pmatrix} a_{11} & a_{12} & a_{13} & \cdots & a_{1n} \\ a_{21} & a_{22} & a_{23} & \cdots & a_{2n} \\ a_{31} & a_{32} & a_{33} & \cdots & a_{3n} \\ a_{41} & a_{42} & a_{43} & \cdots & a_{4n} \\ \cdots & \cdots & \cdots & \cdots & \cdots \\ a_{m1} & a_{m2} & a_{m3} & \cdots & a_{mn} \end{pmatrix} \quad (4.18)$$

Equation 4.18 represents the entries of matrix A . Equations 4.12 to 4.17 giving partial derivation of three unknown variables and the expansion by Taylor series leading to linearization. Getting the coefficients of these unknowns lead to Equation 4.19 which is ultimately used in the basic least squares matrix equation.

$$A = \begin{pmatrix} \frac{\partial f_1}{\partial \phi} & \frac{\partial f_1}{\partial \theta} & \frac{\partial f_1}{\partial \psi} \\ \frac{\partial g_1}{\partial \phi} & \frac{\partial g_1}{\partial \theta} & \frac{\partial g_1}{\partial \psi} \\ \frac{\partial f_2}{\partial \phi} & \frac{\partial f_2}{\partial \theta} & \frac{\partial f_2}{\partial \psi} \\ \frac{\partial g_2}{\partial \phi} & \frac{\partial g_2}{\partial \theta} & \frac{\partial g_2}{\partial \psi} \end{pmatrix} \quad (4.19)$$

4.3.3.3 Solution of Least Squares Adjustments

Solution of finding the attitude angles of a satellite is given by Equation 4.20. These angles are fed to PPM in its first step for finding rotation matrix. In the original version of PPM, the angles were provided by ancillary data as constant quantities. But in the Level-3 geometric correction technique these are corrected with the help of GCPs from Google Earth and by the application of least square adjustments.

$$\begin{bmatrix} \phi - \phi_0 \\ \theta - \theta_0 \\ \varphi - \varphi_0 \end{bmatrix} = (A^T A)^{-1} A^T \begin{bmatrix} lon_1 - f_1 \\ lat_1 - g_1 \\ lon_2 - f_2 \\ lat_2 - g_2 \end{bmatrix} \quad (4.20)$$

Comparing Equation 4.20 with Equation 4.2 makes clear that left hand side of the equation is the solution matrix. In Equation 4.2 the unknown values were denoted by X . It has already been stated that L are the observations i.e the values of known quantities, in our

case the GCPs, whose longitudes and latitudes are provided by the programmer. In simple form these observations can be written as Equation 4.21 and 4.22.

$$L = [\textit{world coordinates} - \textit{image coordinates}] \quad (4.21)$$

$$L = \begin{bmatrix} \textit{longitude}_1 - f_1 \textit{ pixel projection longitude} \\ \textit{latitude}_1 - g_1 \textit{ pixel projection latitude} \\ \textit{longitude}_2 - f_2 \textit{ pixel projection longitude} \\ \textit{latitude}_2 - g_1 \textit{ pixel projection latitude} \\ \vdots \quad \quad \quad \vdots \quad \quad \quad \vdots \end{bmatrix} \quad (4.22)$$

4.3.4 The Iteration Process of Level-3 Correction Algorithm

The proposed technique explained has four steps. Step one deals with finding GCPs from Google Earth. Their longitudes and latitudes are matched with the pixel lines and samples. Then minimized squared residuals $Min h$ are calculated with the help of least squares method. In step two, the non-linear functions about three angels of instrument bias are linearized through partial derivation and subsequent expansion by Taylor series. In step three, coefficients of unknowns are found. They form unknown matrix of the basic equation of least squares adjustment. Step four gives the solution of unknowns. Multiplication of coefficients of unknowns in step 3 and the matrix of observations (the difference of GCPs and pixel projection longitudes and latitudes) give resultant values of matrix X . The resultant matrix is the solution of attitude angles. Equations 4.23 to 4.25 show the assignment of new angles.

$$\varphi_0^{new} = \varphi \quad (4.23)$$

$$\theta_0^{new} = \theta \quad (4.24)$$

$$\psi_0^{new} = \psi \quad (4.25)$$

On completion of fourth step, newly obtained values of attitude / instrument bias are reassigned to step two (refer to Equations 4.14 to 4.17). The process is repeated from step two again. Iterative process continues this way till all the pixel values are assigned with the new attitude angle values. Subsequently using procedure of PPM, input image is projected to the new output image. Pixel values are transformed to their new values given by the algorithm. Flowchart of the algorithm is shown in Figure 4.7.

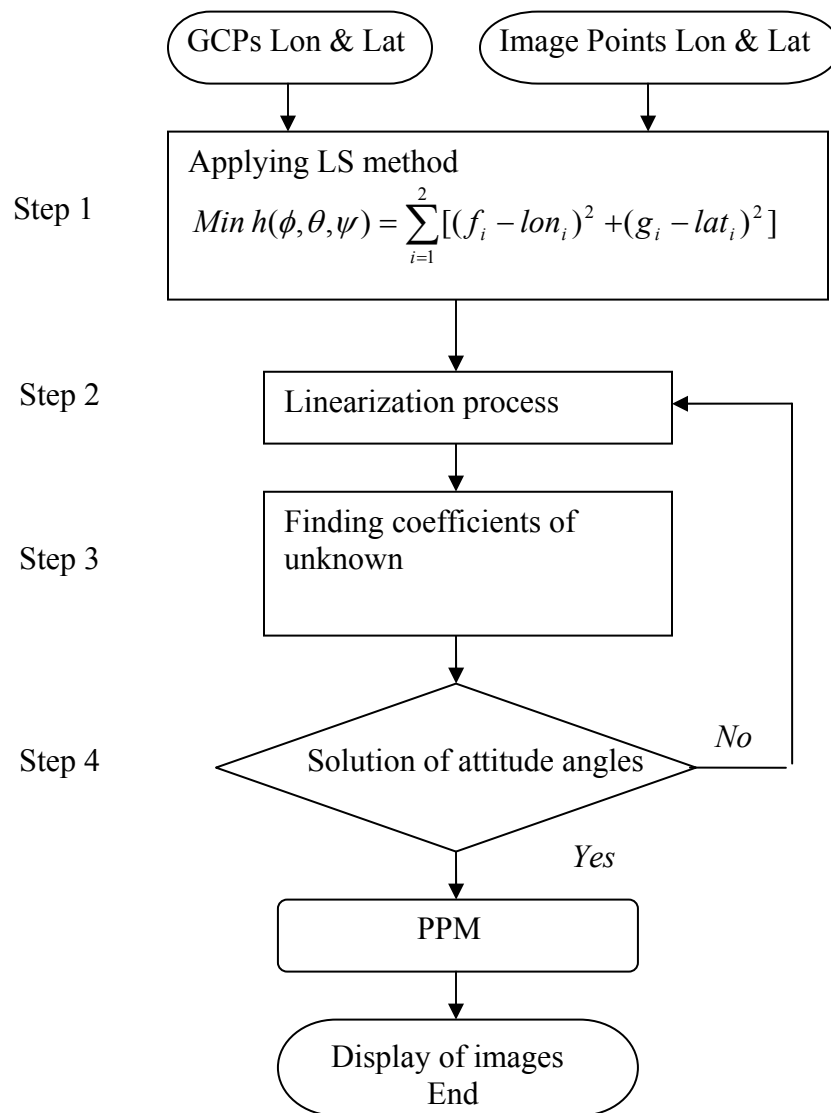


Figure: 4.7 Iteration process in Least Squares adjustment algorithm

4.4 Improvements Achieved in PPM

Three important and main changes were made in PPM to achieve Level-3 geometric correction. They include: GCPs incorporation in geo-referencing, amalgamation of GCPs and vertices based geo-referencing methods together and modification of attitude angles with least squares method for gaining correct attitude angles. These refinements improved the application of pixel projection model (PPM) to Level-3 geometric correction. Level-3 geometrically corrected image of FORMOSAT-2 is achieved with these improvements. Figure 4.8 shows diagrammatically the complete algorithm highlighting enhancements made to achieve Level-3 geometric corrections.

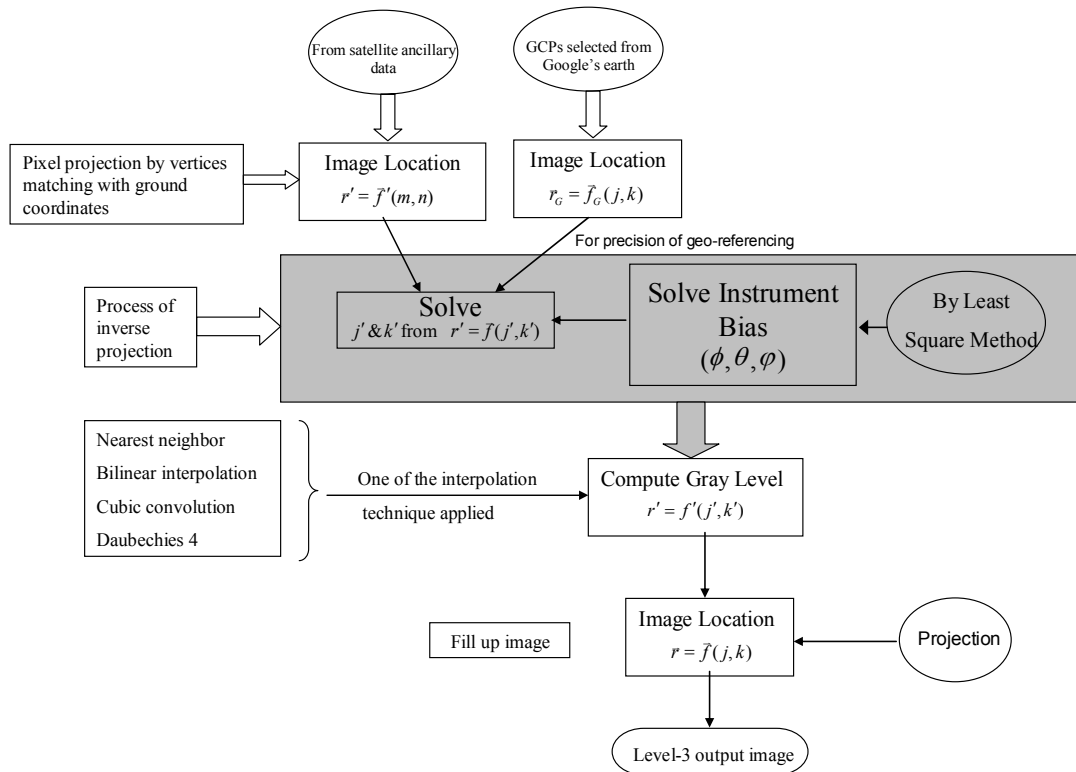
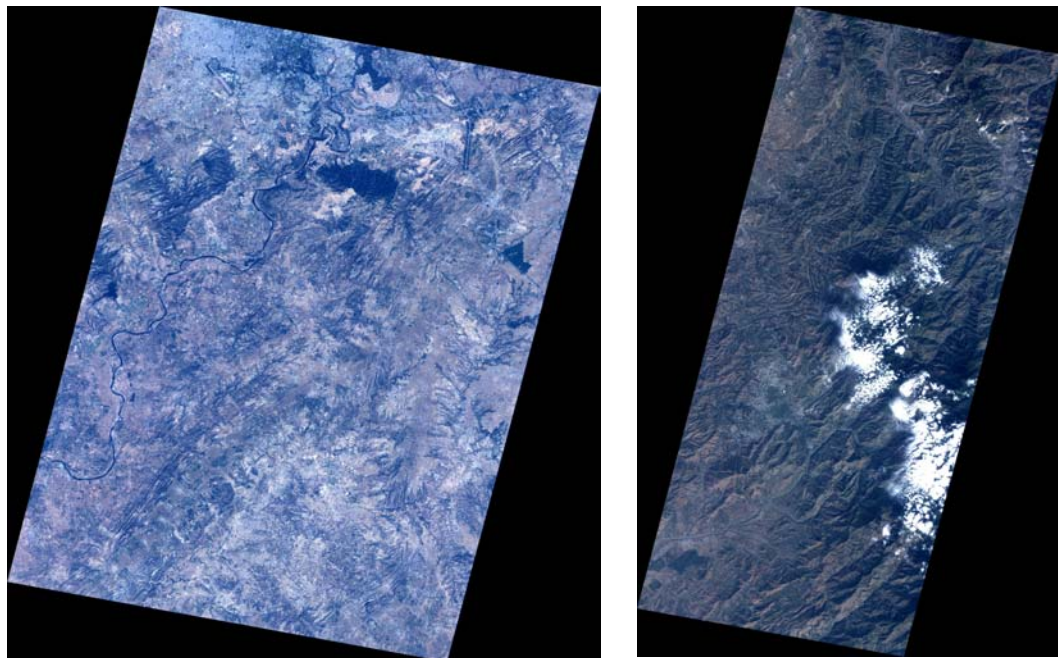


Figure: 4.8 Level-3 pixel projection method for geometric correction

FORMOSAT-2 satellite images are geo-referenced with GCPs selected from Google Earth software and vertices of images obtained from ancillary data of the satellite. Instrument bias is found with least square method and the gray level values are computed using an interpolation method. This technique supports four methods; nearest neighbor, bilinear interpolation, cubic convolution and Daubechies 4 methods. User can apply any one of these.

Two images, test image-1 and test image-2 shown in Figure 4.1 were obtained from FORMOSAT-2 (courtesy NSPO) of earthquake affected areas of Pakistan. Both images were processed and geo-referenced using Level-3 geometric correction version of PPM. Figure 4.9 (a) and (b) shows the output images obtained with Level-3 geometric correction technique. Raw satellite images have both radiometric and geometric distortions but with this technique remotely sensed images are radiometrically as well as geometrically corrected.



(a) South of Islamabad

(b) North of Abbottabad

Figure: 4.9 Level-3 geometrically corrected test images of Pakistan

4.5 Summary

In this chapter a novel approach for improvement of PPM with a view to enhancing FORMOSAT-2 imagery has been proposed. The original version of PPM, described in Chapter 3, did not include any GCP. In the proposed algorithm not only GCPs have been incorporated for precision geo-referencing of satellite imagery to ground coordinate system but the instrument bias has also been corrected with the application of least squares adjustment. The algorithm consisting of four steps has been described mathematically. In the first step, GCPs are found from Google Earth and matched with the pixels lines and samples of the image. Minimized squared residuals are calculated with the help of least squares method. The non-linearities of attitude angles are removed by taking derivatives of the function and expanding by Taylor series in the second step. Coefficients of unknown and solution of basic least square matrix are found in third and fourth step, respectively.

These computations are completed with an iterative process. The iteration process of Level-3 geometric correction technique has been explained in this chapter. It is important to note that the increased number of GCPs will increase the computation time and efforts. Selecting more number of GCPs means more time requirement of the processor for completion of this application because all GCPs are included in the process of computation. However, this extensive mathematical work is beneficial to achieve geometric correction of FORMOSAT-2 imagery. Level-3 images obtained with this technique are the highly accurate images of FORMOSAT-2 satellite imageries.

Experimental Results

5.1 Introduction

The proposed algorithm for removal of geometric distortions caused by attitude of spacecraft in satellite imagery has been described in Chapter 4. Level-3 PPM is a new and unique method of geo-referencing and geometric correction. For high precision geo-referencing, both vertices and GCPs have been used. With this approach more precise geo-referencing of satellite imagery was achieved and a Level-1 image was successfully converted to Level-3 geometrically corrected image. In this chapter, residual analysis of this new approach is carried out. The chapter is divided into three sections. First section presents the residual analysis carried out in two steps. In first step an image to image matching is performed and their Mean Square Error (*mse*) is calculated. In second step, eight points in the original image and geo-referenced images are selected and their *mse* is calculated. In the following section two different experiments for resampling of pixel values are presented. Finally, Level-3 geometric correction technique is applied on different images and they are tested for disaster monitoring application in the last section.

5.2 Residual Analysis

The goal of residual analysis is to find percentage of error between original version of PPM which gives Level-2 correction and Level-3 geometric correction technique, an enhanced version of PPM. In that corrected images with both the versions of PPM are compared with the original image acquired from Google Earth. The analysis is carried out in

two steps. First step deals with image to image matching and finding out their *mse*. Step 2 involves point to point matching and their *mse* calculations. Figure 5.1 shows three images of the test image 1 (Image of south of Islamabad obtained on 28th Oct 2005 by FORMOSAT-2). Figure 5.1 (a) is the original image obtained from Google Earth in its geocentric coordinates, the processed image with the PPM and the resultant Level-3 geometrically corrected images are shown in Figure 5.1 (b) and (c) respectively.

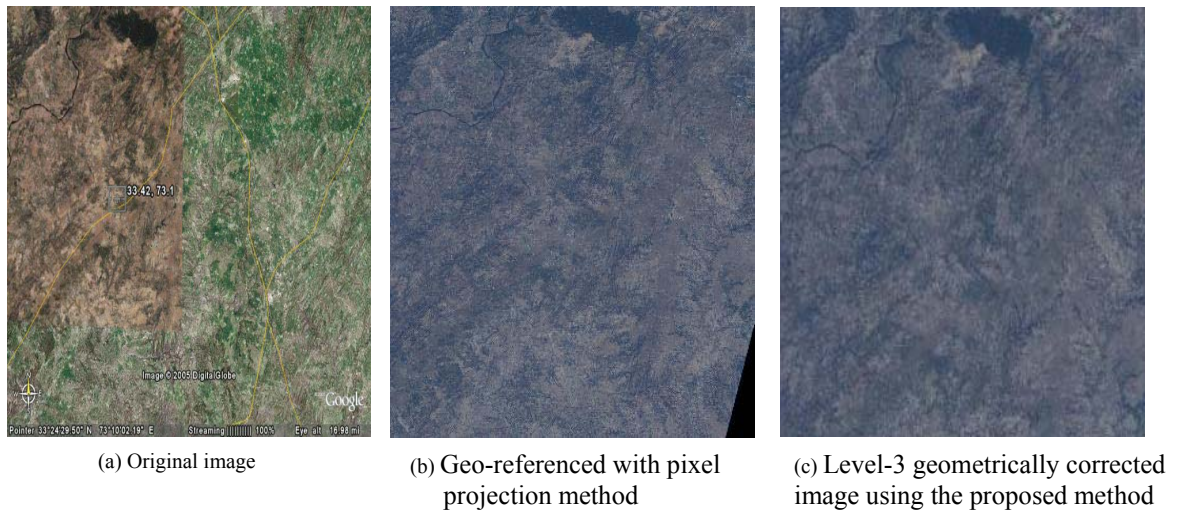


Figure: 5.1 Original and geo-referenced images of Islamabad

5.2.1 Image Matching

An Area of Interest (AOI) was selected in the test image. The portion of image was geometrically corrected using PPM and the proposed method. The AOI image and its corresponding geo-referenced images are shown in Figure 5.2 (a), (b) and (c).

The AOI in the original image, I_O , was matched with the AOI of Level-2 geo-referenced image I_{L2} and AOI of Level-3 geometrically corrected image I_{L3} . Using the differences between the images mean error is computed using Equations 5.1 and 5.2 implemented in MATLAB.

$$mse_1 = \text{mean}[(I_o - I_{l-2})^2] \quad (5.1)$$

$$mse_2 = \text{mean}[(I_o - I_{l-3})^2] \quad (5.2)$$

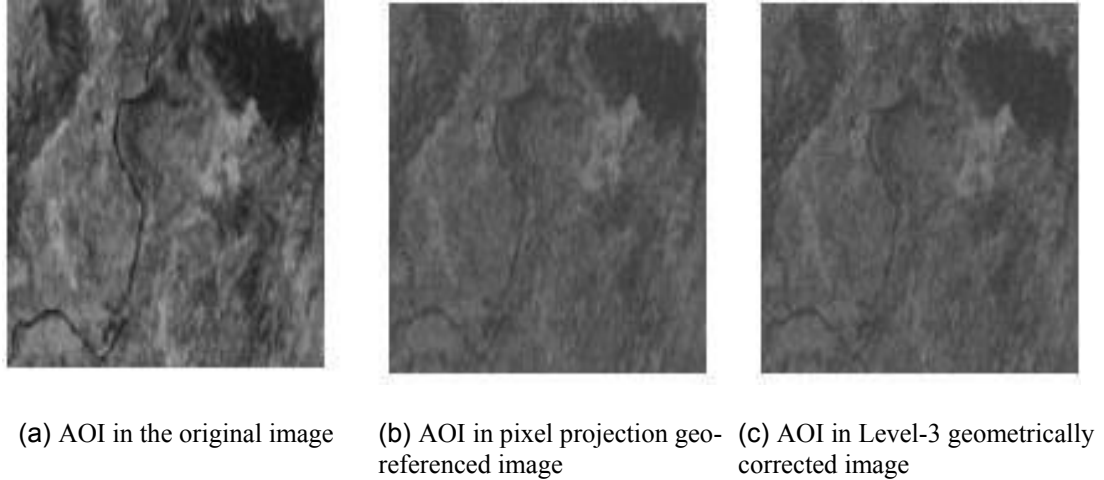


Figure: 5.2 AOI in original and geo-referenced images.

Mse_1 of the original image and Level-2 geo-referenced image comes to be 438.3470. On the other hand, mse_2 of original image and Level-3 geometrically corrected is 354.9952. It is evident that there is a mark decrease in mse of the image corrected with Level-3 geometric correction technique as compared to the one corrected with Level-2 geo-referencing method. Mse computation by image matching method showed that errors in the image have been reduced significantly by applying Level-3 geometric correction technique.

5.2.2 Point to Point Error Estimation

Point to point mean error calculation is another method of residual analysis for error estimation. It is implemented in MATLAB. For this eight control points (CPs) are randomly selected. The CPs in the original AOI image are shown in Figure 5.3. CPs at the same geo-

locations are also selected in the corresponding Level-2 and Level-3 geo-referenced images and are analyzed for residue calculations.

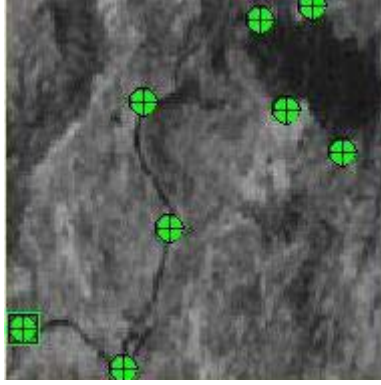


Figure: 5.3 AOI in original image with 8 CPs.

Equations 5.3 to 5.10 are used to calculate individual and total *mse* for these points.

$$mse1 = (x_{pp} - x_o)^2 / 2 \quad (5.3)$$

$$mse2 = (y_{pp} - y_o)^2 / 2 \quad (5.4)$$

$$total\ mse(along\ x - axis) = (x_{pp(1-8)} - x_{o(1-8)})^2 / 8 \quad (5.5)$$

$$total\ mse(along\ y - axis) = (y_{pp(1-8)} - y_{o(1-8)})^2 / 8 \quad (5.6)$$

$$mse1 = (x_{opti} - x_o)^2 / 2 \quad (5.7)$$

$$mse2 = (y_{opti} - y_o)^2 / 2 \quad (5.8)$$

$$total\ mse(along\ x - axis) = (x_{opti(1-8)} - x_{o(1-8)})^2 / 8 \quad (5.9)$$

$$total\ mse(along\ y - axis) = (y_{opti(1-8)} - y_{o(1-8)})^2 / 8 \quad (5.10)$$

where x_{pp} means x -coordinates of image corrected by pixel projection method (Level-2).

y_{pp} means y -coordinates of image corrected by pixel projection method (Level-2).

x_o means x -coordinates of original image.

- y_o means y -coordinates of original image.
- x_{opti} means x -coordinates of image geometrically corrected (Level-3).
- y_{opti} means y -coordinates of image geometrically corrected (Level-3).
- $x_{pp(1-8)}$ means aggregate values of all the eight x_{pp} in the image.
- $y_{pp(1-8)}$ means aggregate values of all the eight y_{pp} in the image.
- $x_{o(1-8)}$ means aggregate values of all the eight x_o in the image.
- $y_{o(1-8)}$ means aggregate values of all the eight y_o in the image.
- $x_{opti(1-8)}$ means aggregate values of all the eight x_{opti} in the image.
- $y_{opti(1-8)}$ means aggregate values of all the eight y_{opti} in the image.

Tables 5.1 and 5.2 show the *mse* worked out for the eight points. PP, Orig and Opti refers to pixel projection method (Level-2), original image cropped from Google Earth software and optimized geometrically corrected (Level-3) images, respectively. Improvements are observed in the values of *mse* along both x and y coordinates. Table 5.1 shows *mse* calculated for the pixel projection method (PPM) with reference to the original images. *Mse* for x coordinates is 1.9801425 and for y coordinates it is 10.1630875. Whereas, Table 5.2 shows values of *mse* calculation for geometrically corrected technique with reference to the original images. Values of *mse* for the Level-3 geometrically corrected method (proposed method) for x coordinates is 0.677126 and for y coordinates it is 5.44588625. It is evident from the comparison of *mse* values given in tables that errors have reduced 50% along both the axes of the image. The geometrically corrected Level-3 image has fewer errors as compared to that of pixel projection method (Level-2) image while locating it to the original geo-referenced image.

Table: 5.1 MSE using pixel projection method (PPM).

S/No.	PP X-Coordinate	PP Y-Coordinate	Orig X-Coordinate	Orig Y-Coordinate	mse-1 $(x_{PP} - x_O)^2 / 2$	Total mse $(x_{PP(1-8)} - x_{O(1-8)})^2 / 8$	mse-2 $(y_{PP} - y_O)^2 / 2$	Total mse $(y_{PP(1-8)} - y_{O(1-8)})^2 / 8$
1.	84.404	7.3546	85.426	9.2837	0.522	1.9801425	1.861	10.1630875
2.	101.43	2.4752	101.54	4.4043	0.006		1.861	
3.	93.369	38.447	94.39	43.326	0.521		11.902	
4.	112.55	50.475	112.21	54.106	0.058		6.592	
5.	44.348	35.383	46.504	37.312	2.324		1.861	
6.	55.582	67.383	55.582	71.355	0		7.888	
7.	37.879	123.44	40.603	125.26	3.710		1.656	
8.	5.3121	108.57	6.5603	112.32	0.779		7.031	

Table: 5.2 MSE using Level-3 geometric correction method.

S/N o.	Opti X-Coordinate	Opti Y-Coordinate	Orig X-Coordinate	Orig Y-Coordinate	mse-1 $(x_{Opti} - x_O)^2 / 2$	Total mse $(x_{Opti(1-8)} - x_{O(1-8)})^2 / 8$	mse-2 $(y_{Opti} - y_O)^2 / 2$	Total mse $(y_{Opti(1-8)} - y_{O(1-8)})^2 / 8$
1.	85.426	11.44	85.426	9.2837	0	0.677126	2.324	5.44588625
2.	101.31	6.2199	101.54	4.4043	0.026		1.648	
3.	94.277	43.44	94.39	43.326	0.006		0.006	
4.	110.5	50.362	112.21	54.106	1.445		7.008	
5.	45.482	38.333	46.504	37.312	0.522		0.521	
6.	55.695	69.426	55.582	71.355	0.006		1.86	
7.	39.468	122.3	40.603	125.26	0.6441		4.38	
8.	6.2199	109.48	6.5603	112.32	0.057		4.033	

5.3 Image Resampling

Having determined the mapping polynomials explicitly by use of GCPs or PPM the next step is to find points in the image corresponding to each location in the pixel grid. As expected grid centers will not usually project to exact pixel center locations in the image for which resampling is required [133-136]. For image resampling, three interpolation techniques are used [137,138]. After achieving Level-3 geometric correction, further experiments for image resampling were carried out. Bilinear interpolation technique was used for Level-2 PPM. In our experimentation we first investigated conventional interpolation techniques namely, Nearest Neighbor (NN), Bilinear Interpolation (BI) and Cubic Convolution (CC). Then, another experiment using Daubechies 4 (D-4) wavelet filter

for the process of resampling was carried out. This method substantially reduced the complexity of the algorithm. These experiments are discussed in details in this section.

5.3.1 Applying Different Approximations for Pixel Transformations

There are a number of techniques one might use to resample or transform an image. These generally have a tradeoff between speed and the degree to which they reduce visual artifacts. Each approximation scheme has distinct properties and affects an image information content, but each method must be evaluated with respect to the imagery's intended use [139-141]. The methods are nearest neighbor, bilinear interpolation and cubic convolution.

5.3.1.1 Nearest Neighbor (NN)

In this method each output pixel value is unmodified value from the closest input pixel. Therefore, less computation is involved than in other methods. However, when the raster data is resampled to a different cell size, a blocky appearance does result. The blocky appearance is because of duplication (smaller output cell size) or dropping (large output cell size) of input cell values [138, 142].

5.3.1.2 Bilinear Interpolation (BI)

An output cell value in the BI method is the weighted average of the four closest input cell values. This method produces a smoother appearance than the nearest neighbor approach, but it can diminish the contrast and sharpness of feature edges [138, 143].

5.3.1.3 Cubic Convolution (CC)

This method calculates an output cell value for a 4 x 4 block of surrounding input cells. This method produces sharper, less blurry images than BI, but computationally it is the most expensive resampling method [139, 140].

5.3.1.4 Comparison of Resampling Methods

Figures 5.4 and 5.5 show the results obtained with the aforementioned resampling techniques. The Figures 5.4 (a), (b), (c) and 5.5 (a), (b), (c) show the transformation of Level-3 geometric correction PPM algorithm applying NN, BI and CC approximations, respectively. Figures 5.6 and 5.7 are 3-dimensional plots of these approximation techniques. Figures 5.6 and 5.7 (b) (c) and (d) represent NN, BI and CC plots, respectively. The algorithm for comparison of interpolation methods was developed in MATLAB, however in Level-3 PPM geometric correction technique these methods are implemented using C++.

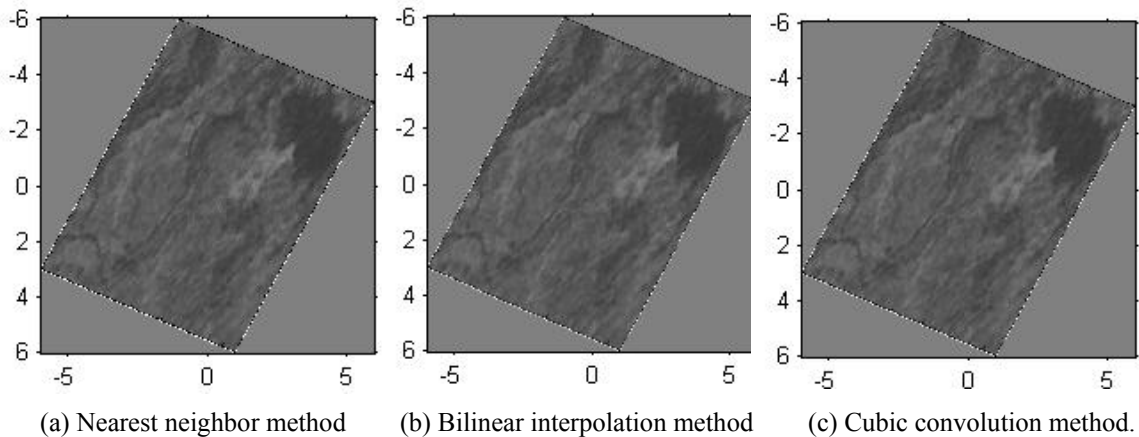


Figure: 5.4 Results of three different approximation techniques for Islamabad image

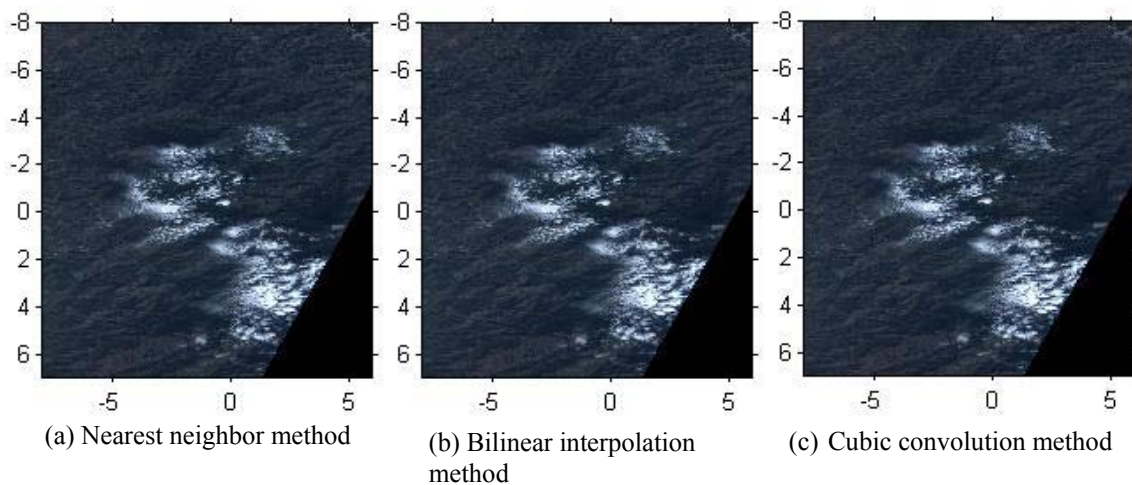
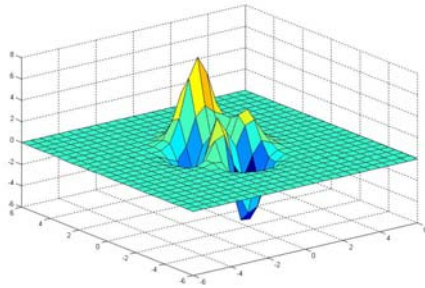
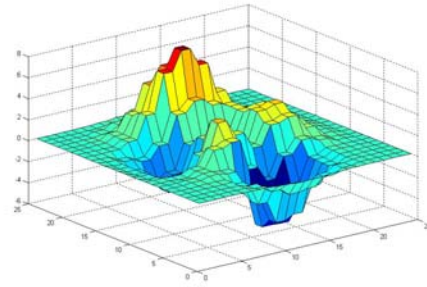


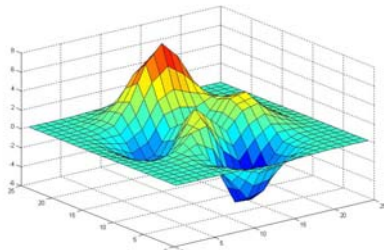
Figure: 5.5 Results of three different approximation techniques for Abbottabad image



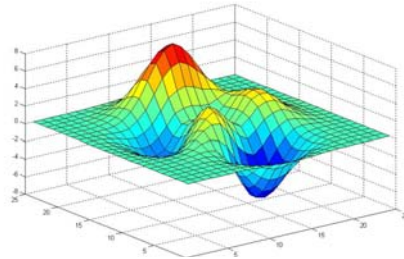
(a) Meshgrid



(b) Nearest neighbor method

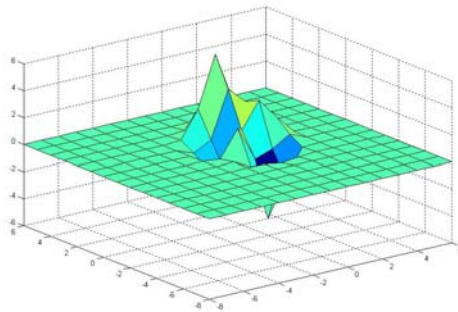


(c) Bilinear interpolation method

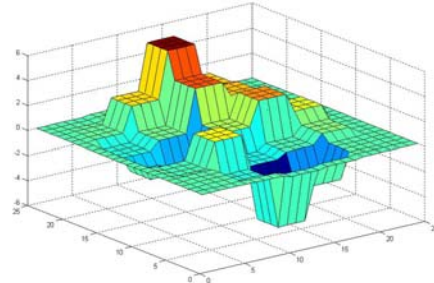


(d) Cubic convolution method

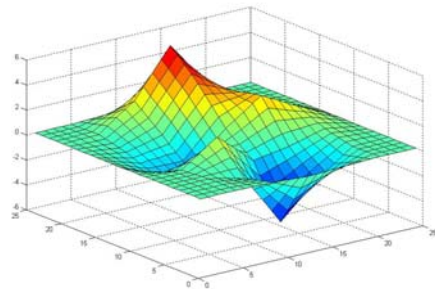
Figure: 5.6 3-dimensional plots of the approximations applied on test image 1 (Islamabad)



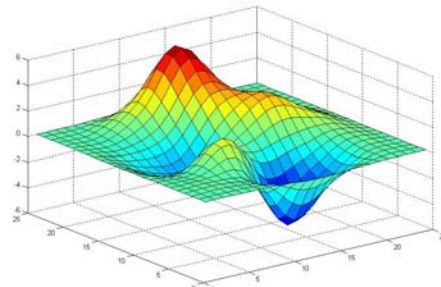
(a) Meshgrid



(b) Nearest neighbor method



(c) Bilinear interpolation method



(d) Cubic convolution method

Figure: 5.7 3-dimensional plots of the approximations applied on test image 2 (Abbottabad)

Figures 5.6 (a) and 5.7 (a) are 3-D plot meshes obtained by applying MATLAB *meshgrid* function [144]. The ranges of *meshgrid* function have been fixed to (-3: 0.5: 3) and (-3: 1: 3), respectively on a 7 x 7 matrix data which transforms the domain specified by vectors x and y to arrays X and Y . In MATLAB *peaks* function is used to generate peaks at low resolution. This *peaks* function was used to generate peaks of vectors x and y . In MATLAB notation, it is expressed as $z = \text{peaks}(x, y)$ [145] which to transform vectors x and y on mesh grid where intensity maximum and minimum values are plotted on peaks denoted by z . This is how the 2-d vector data is transformed into 3-d mesh.

Comparison of surface plots of different interpolation methods reveals that the CC method produces smoother peaks than NN and BI methods. The edges of the peaks show the varying intensities of the image grid. The image grids were obtained by using three different interpolation methods. The smoothness of the edges means continuity of the varying intensity values. More smoothness in the peaks means more continuity in the intensity values and less loss of information. By comparing three mesh plots it is apparent that information loss is negligible in CC method. In NN and BI, the drastic changes in the edges of peaks mean discontinuity in the intensity values of the resultant images and similarly there is information loss. Hence image obtained with CC method is closer to the original image as contrast to NN and BI methods.

5.3.1.5 Discussion on Resampling Methods Result

The simplest method of resampling an image is NN. Using this method one finds the closest corresponding pixel in the original image for each pixel in the destination image but it has its drawbacks also. In original version of PPM transformation was carried out with BI method. This method still has its own shortcomings. Therefore, there was a need to

investigate other 2-D interpolation techniques to determine a more suitable technique for transformation of pixel values. Three approximation methods were applied to obtain an optimal result. Test images of FORMOSAT-2 satellite shown in Figure 4.1 were used for testing/ justification.

The comparison and analysis of these interpolation methods were carried out using MATLAB. Inbuilt set of functions and tools including *cpselect*, *cpstruct2pairs*, *cp2tform*, *tformfwd*, and *imtransform* from the image processing toolbox, in combination with *pix2map*, *meshgrid* and interpolation functions like *interp2* from the mapping toolbox were used. Mathworks.com's help (www.mathworks.com) enabled us to geo-register remotely sensed data based on CP pairs to carry out testing and comparison of different interpolation techniques [146].

The approximation techniques were applied to the test images shown in Figure 4.1. Images obtained after resampling with these approximations are shown in Figures 5.4 and 5.5. The 3-D plots (Figures 5.6 and 5.7) to see the surfaces of these functions showing smoothness in peaks were also obtained. The 3-D plot of cubic convolution showed the most suitable peaks curve and hence is considered the excellent choice for pixel value transformation. To prove the same result alternatively, another good function of MATLAB (*imcontour*) was used. This function draws a 2-D contour plot of the intensity image, automatically setting up the axes so that their orientation and aspect ratios match the image. Contour plots for the three interpolation techniques are shown in Figures 5.8 and 5.9. Comparison of contour plots based on the surface plots of these approximation methods show the minimum and maximum values of the input image data matrix. Contour plots for

CC method in Figures 5.8 (c) and 5.9 (c) provide smoother details of the image data than NN and BI methods.

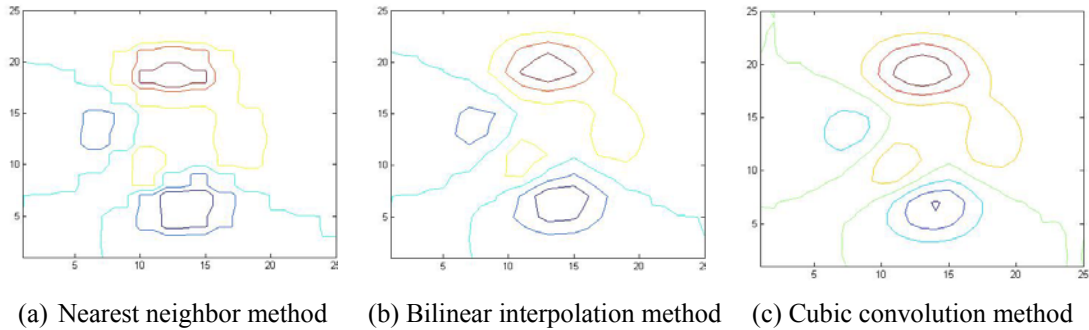


Figure: 5.8 2-dimensional contour plots of the approximations techniques applied on test image 1 (Islamabad)

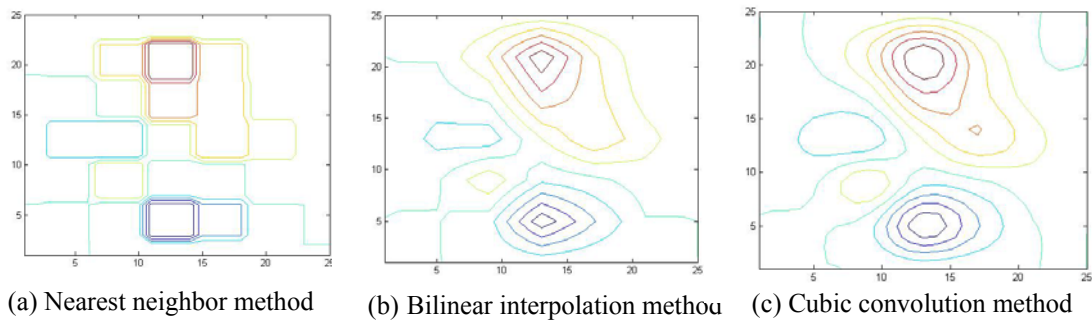


Figure: 5.9 2-dimensional contour plots of the approximations techniques applied on test image 2 (Abbottabad)

5.3.2 Wavelet Based Resampling Algorithm for Image Transformation

Different resampling techniques were investigated and applied to image pixel transformation to produce a geo-referenced image in Section 5.3.1. It was revealed that CC based modeling gave the best output pixel values compared to BI and NN methods.

In this section, another method based on Daubechies 4 (D-4) wavelet filter has been developed for image resampling. The wavelet and scaling coefficients for this filter are

arranged in a 2 x 4 ordered filter. The filter window proceeds from left to right and from top to bottom taking each pixel into account along the way. Diagrammatically it is shown in Figure 5.10. The resultant convoluted values are averaged. These new pixel values finally replace the original image pixel in the output image. Our results show that the geometrically corrected image with this resampling method is visually similar to the one obtained with CC method.

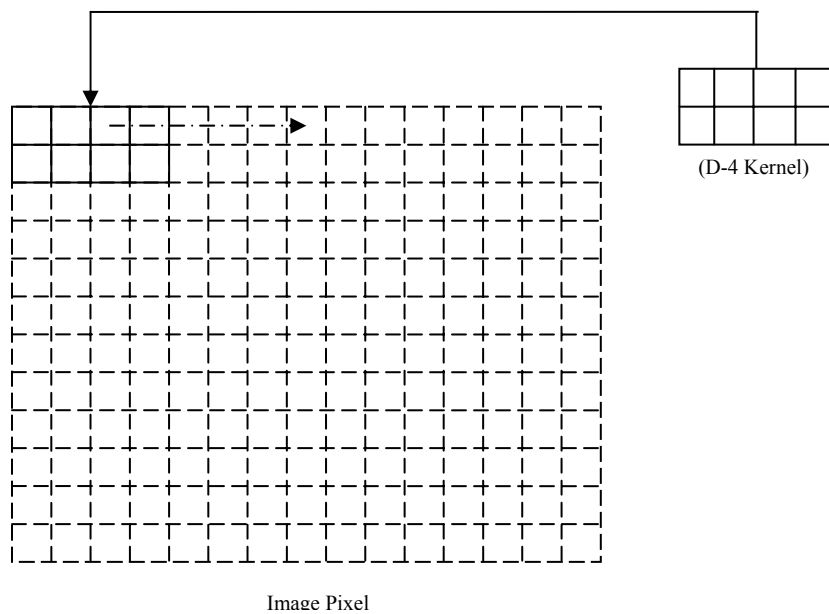


Figure: 5.10 D-4 Kernel Application

Though, root mean square (*rms*) of cubic convolution method is closer to the *rms* of the original image. There is 97.677% and 99.144 % resemblance for Islamabad image (test image 1) and 96.66% and 94.4% resemblance for Abbottabad image (test image 2) in *x*- and *y*- coordinates. Yet complexity of algorithm for CC method is more than all other methods. Whereas, D-4 based resampling method gives much optimized solution of image resampling. It has 97.5% and 98.897% resemblance for test image 1 and 94.086% and 94.183%

resemblance for test image 2 in x - and y - coordinates. Moreover, its *rms* value is also closer to the *rms* value of original image while its complexity is same as the BI method. Its execution time is also 56.7 % lesser than CC method. Therefore resampling based on D-4 wavelet filter is a better choice for cubic convolution method in image pixel transformation. In this section a three step comparison is also carried out among four interpolation/resampling methods which include D-4 wavelet filter based resampling and three conventional resampling methods NN, BI and CC.

5.3.2.1 Daubechies 4 (D-4) Wavelet Filter

The D-4 filter has four wavelet and four scaling function coefficients. The scaling function coefficients h_0 , h_1 , h_2 and h_3 are given in Equation 5.11.

$$h_0 = \frac{1+\sqrt{3}}{4\sqrt{2}}, h_1 = \frac{3+\sqrt{3}}{4\sqrt{2}}, h_2 = \frac{3-\sqrt{3}}{4\sqrt{2}} \text{ and } h_3 = \frac{1-\sqrt{3}}{4\sqrt{2}} \quad (5.11)$$

The wavelet function coefficient values are given in Equation 5.12.

$$g_0 = h_3, g_1 = -h_2, g_2 = h_1 \text{ and } g_3 = -h_0 \quad (5.12)$$

The scaling and wavelet functions are calculated by taking the inner product of the coefficients and the input image. Equations 5.13 and 5.14 give the inner product.

$$x[i] = h_0s[i] + h_1s[i+1] + h_2s[i+2] + h_3s[i+3] \quad (5.13)$$

$$y[j] = g_0s[j] + g_1s[j+1] + g_2s[j+2] + g_3s[j+3] \quad (5.14)$$

$s[i, j]$ in Equations (5.13) and (5.14) gives pixel value before resampling whereas $x[i]$ and $y[j]$ are the pixel values after resampling. Each iteration in the wavelet transform step calculates a scaling function value and a wavelet function value. The index i is incremented with each iteration, and new scaling and wavelet function values are calculated. Application details of D-4 to 1-D data are available in [147, 148].

5.3.2.2 Results of D-4 Wavelet Based Resampling

Previously, the test images were geometrically corrected to obtain Level-3 products by applying conventional interpolation techniques. Now the D-4 wavelet filter is being used for transforming image pixels. A 2 x 4 filter has been developed and applied on image data to transform pixel value into an output image. The resulting convoluted and averaged pixel values are used to replace the old input image pixel values. Test images 1 and 2 of FORMOSAT-2 are resampled with this method, results are given in Figure 5.11. Comparative analysis of D-4 method with other interpolation techniques used for resampling is given in Section 5.3.2.3.

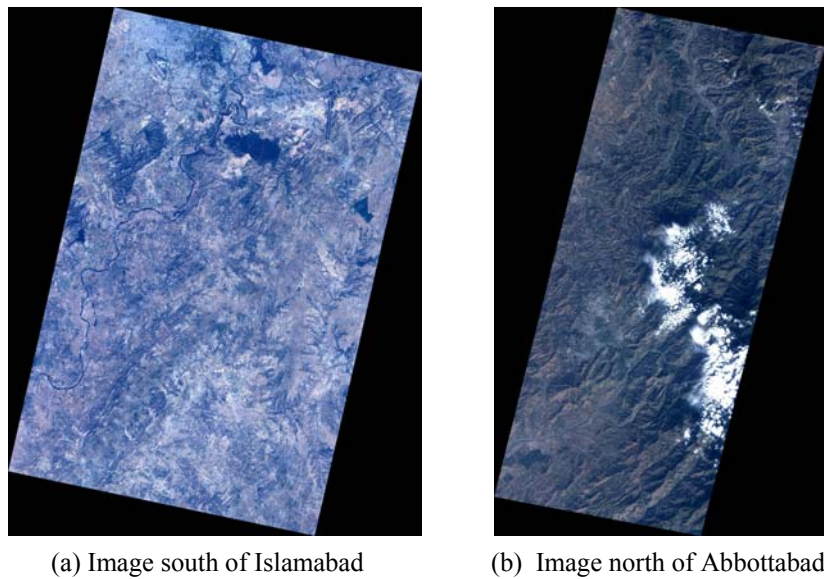


Figure: 5.11 Test images resampled with D-4 method

5.3.2.3 Analysis of D-4 Wavelet Based Resampling

To calculate *rms* values for these four methods of resampling eight random points (GCPs) were selected in geo-referenced images. Comparison was carried out among images resampled with four interpolation techniques and original geo-referenced image. The points

are shown in Figures 5.12. The accuracy, the visual interpretation and the efficiency of D-4 resampling algorithm was found much better as compared to other interpolation methods.

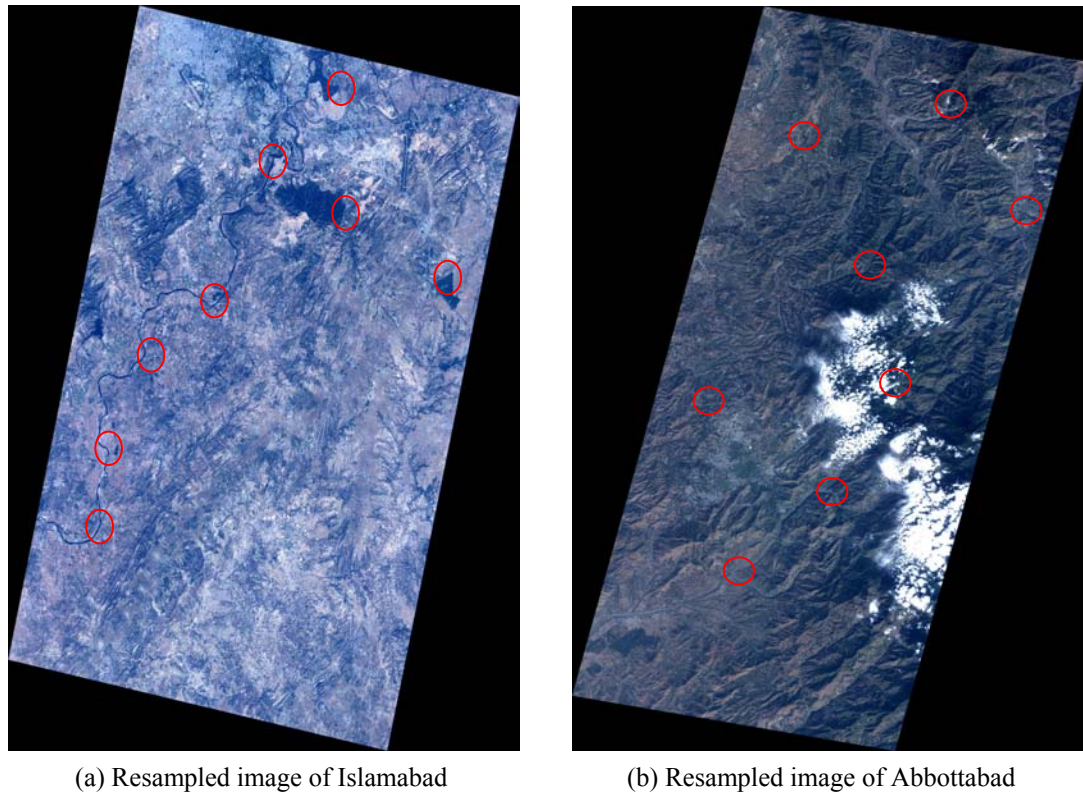


Figure: 5.12 Resampled test images with randomly selected 8 points

There are several important considerations in the analysis of any interpolation method. Of major importance is the accuracy of the technique, that is, exactness with which the interpolation function reconstructs the sampled function [149,150]. Additionally, some interesting effects can be predicted from the spectral characteristics of the interpolation kernel [151]. The accuracy and efficiency of the D-4 wavelet interpolation algorithm is compared with the conventional methods in this section. Analysis is carried out in three

ways. First, complexity of algorithms is found. Second, *rms* values of resultant images of all interpolation methods are calculated. Third, execution time of these methods is calculated.

5.3.2.3.1 Complexity of Algorithm

In the three resampling methods, CC interpolation function produces the best reconstructed image because of taking 4 x 4 neighboring pixels into account for resampling. In contrast, BI scheme reproduces an image having some artifacts. It takes 2 x 2 neighboring pixels into account for resampling. The NN algorithm is simple and straightforward in its application. This algorithm interpolates the nearest pixel it finds. By using CC method instead of BI or NN resampling schemes, the degree of complexity of functions is increased.

However, D-4 wavelet filter algorithm, takes 2 x 4 neighboring pixels for interpolation. With this algorithm higher degree of accuracy is achieved for reconstruction of image like CC scheme but with reduced complexity which is equal to that of BI scheme.

The relative accuracy of different interpolation methods is determined from their convergence rates. The convergence rate is a measure of how fast the approximation error goes to zero as the sampling rate decreases [152]. In CC algorithm, it was found that the approximation error consists of terms proportional to n^3 , where n is the sampling rate. Thus, the convergence rate for the CC interpolation function is $O(n^3)$. D-4's sampling increment is n giving a complexity of $O(n)$ for one-dimensional signal and $O(n^2)$ for a two-dimensional signal. Applying D-4 for image data will have a complexity $O(n^2)$ which is equivalent to BI or any quadratic function. Table 5.3 summarizes the complexities of algorithm in big O notation for the interpolation techniques used for pixel value transformation. Graphically this comparison is shown in Figure 5.13.

Table: 5.3 Summary of complexities of interpolation techniques

Interpolation Method	Complexity
Nearest Neighbor	$O(n)$
Bilinear Interpolation	$O(n^2)$
Cubic Convolution	$O(n^3)$
Daubechies 4	$O(n^2)$

Figure 5.13 shows graphical comparison of these complexities. This comparison is not indicative of the running time or the CPU cycles consumed; it merely gives an indication of how the computational resources will increase as the size of the problem to be solved increases. The horizontal axis in the diagram gives the size of the problem that is the number of records to process in a search algorithm and the vertical axis shows the computational effort required by the algorithms of each class.

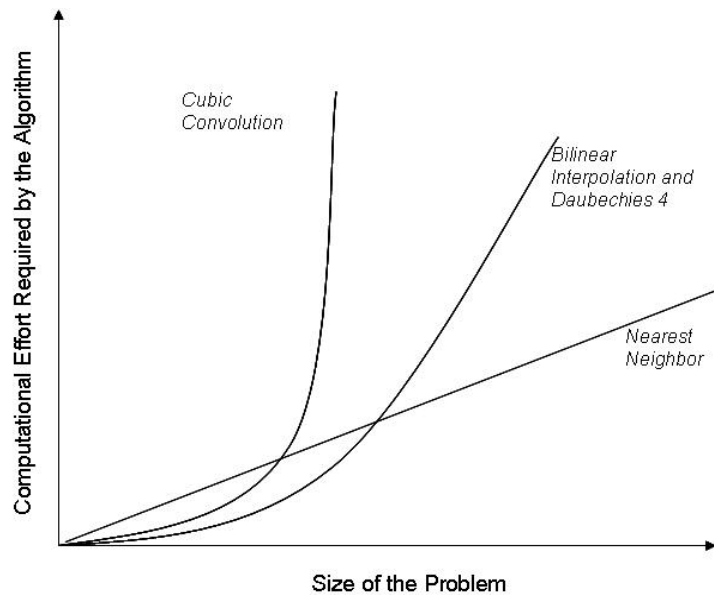


Figure: 5.13 Graphical comparison of complexities

5.3.2.3.2 RMS Analysis in Case of D-4

Rms also known as quadratic mean is a statistical measure of the magnitude of a varying quantity [153]. It is especially useful when variants are positive and negative. Equation 5.15 gives the mathematical representation of *rms* for discrete quantities of a collection of n values $\{x_1, x_2, \dots, x_n\}$. The intensity values are discrete therefore the equation is used to calculate *rms*.

$$x_{rms} \approx \sqrt{\frac{1}{n} \sum_{i=1}^n x_i^2} \quad (5.15)$$

Eight points are randomly selected on the test images 1 and 2. The points are selected in the resultant images geo-referenced with NN, BI, CC and D-4 based resampling methods. These are then compared with the original image. The points are shown in Figures 5.11. *Rms* for the first original image (test image 1 Islamabad) is 1045.858 along x -coordinates (lines) and 937.4257 along y -coordinates (samples). Similarly *rms* value for the second original image (test image 2 Abbottabad) for x and y -coordinates is 1486.68 and 1783.146, respectively [154-155]. *Rms* results achieved using different interpolation methods and their percentage resemblance with the *rms* values of the original image is shown in Table 5.4.

Table: 5.4 *Rms* values for different interpolation methods and their resemblance with the original images

Interpolation Method	Coordinates	Rms for Test Image-1 (Islamabad)	Rms for Test Image-2 (Abbottabad)	% Resemblance with Original Image Coordinates (Test Image 1)	% Resemblance with Original Image Coordinates (Test Image 2)
Nearest Neighbor	x	931.671	1236.761	89.081	83.189
	y	849.411	1493.45	90.611	83.75
Bilinear Interpolation	x	969.579	1307.369	92.71	87.938
	y	911.367	1596.098	97.22	89.51
Cubic Convolution	x	1021.563	1436.96	97.677	96.66
	y	929.4056	1683.29	99.144	94.4
Daubechies 4	x	1019.767	1398.76	97.5	94.086
	y	927.091	1679.42	98.897	94.183

From this analysis, it is clear that CC method gives best results in image transformation. *Rms* values of CC method are closer to the *rms* values of the original images. There is 97.677% and 99.144 % resemblance for Islamabad image (test image 1) and 96.66% and 94.4% resemblance for Abbottabad image (test image 2) in *x*- and *y*- coordinates. However, *Rms* values of D-4 method are also close to the *rms* values of the original test images. These values are 97.5% and 98.897 % for Islamabad image and 94.086% and 94.183% for Abbottabad image in *x*- and *y*- coordinates. This data shows that there is not much of difference between the *rms* values of the images obtained with CC and D-4 methods.

5.3.2.3.3 Execution Time

Since computational complexity is different for the four methods, therefore execution time for these resampling methods is also dissimilar. Execution time of the four methods is given in Table 5.5. The time for the resampling methods has been measured on Microsoft Windows XP Professional Version 2002 Service pack 2 operating system and a system having specifications as Inbox Odyssey 3230 Intel (R) Pentium (R) M mother board, 1.73 GHz processor and 256 MB RAM.

Table: 5.5 Execution time for interpolation methods

Interpolation Method	Running Time
Nearest Neighbor	23 Sec
Bilinear Interpolation	65 Sec
Cubic Convolution	127 Sec
Daubechies 4	72 Sec

The execution time of the resampling methods is dependent upon their computational complexity. NN and BI methods are computationally simple therefore take less execution time which is 23 and 65 seconds respectively for each method. CC method being

computationally more complex takes more time for execution which is 127 seconds. The D-4 method is computationally less complex as compared to CC method therefore its execution time is lesser than CC method. It takes 72 seconds to complete which is only 7 seconds more than BI method but 55 seconds lesser than CC method.

5.4 Application to Disaster Investigation

A simple approach to disaster investigation is to compare the successive observations of the same location. In these observations, even minor variations are monitored. This is categorized as change detection. Various change detection techniques have recently been summarized and reviewed by Lu et al. [156, 157]. Whatever be the method adopted for measuring change detection, it is a prerequisite to have precise geometrical registration between multi-temporal images. The impact of mis-registration on change detection is very significant [158, 159]. By comparing the spatial/ spectral information of a particular object or area over a period of time, the image interpreters can accurately identify the changes occurring. FORMOSAT-2 provides daily revisit images, image interpreters have more capacity to detect why and how changes occurred.

Figure 5.14 shows an example of disaster investigation. Category 5 Hurricane Katrina caused devastation along much of the north-central Gulf Coast of the United States on Aug 29, 2005. Figure shows three images of the Hurricane Katrina, recorded on September 2, 3, and 4, 2005, respectively. Figure 5.14 (a) taken on Sep 2, one day before striking of the hurricane, shows the clouds concentrating in the south west portion of the image. On Sep 3, Figure 5.14 (b) shows the hitting of the hurricane and the extent it is jetting in towards the north. Figure 5.14 (c), image taken on Sep 4, shows the aftermath of the Hurricane. These revisit images of the same scene with techniques of image processing for precise geo-

referencing and geometric correction give accurate information about disaster investigation of an area which makes the job of an image interpreter easy and efficient. To investigate certain features in the images, their color composites can be visually identified, however for a detailed analysis; histogram linear stretching or histogram equalization is applied.



(a) New Orleans,
2005.9.2

(b) New Orleans,
2005.9.3

(c) New Orleans,
2005.9.4

Figure: 5.14 Images of FORMOSAT-2 after disaster category 5 Hurricane Katrina struck New Orleans

Figure 5.15 shows another example of disaster investigation. The images were recorded in Mar 2006, of Alert, Canada. Alert is the northernmost permanently inhabited place in the world. It is located at $82^{\circ}28'N$, $62^{\circ}30'W$, about 10 km west of Cape Sheridan, the northeastern tip of Ellesmere Island, on the shore of ice-covered Lincoln Sea, in the territory of Nunavut in Canada. Figure 5.15 shows the drift in the rapture of ice bound mountainous region. Images recorded on Mar 24, 25 and 26, 2006 show the change taking place. It may be a result of climate change or global warming but presents a thought provoking area for the environmental monitoring agencies and analysts to carry on with their studies about the global events which are effectively covered by the FORMOSAT-2's daily revisit.

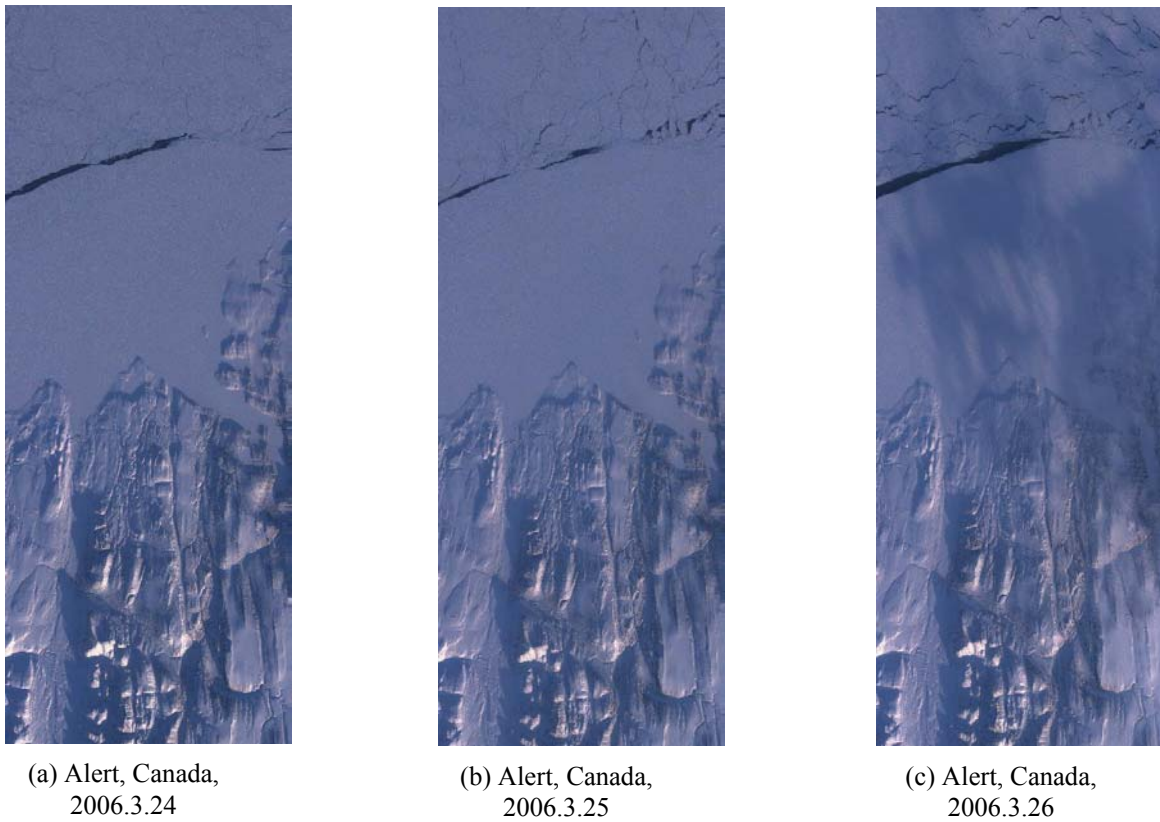


Figure: 5.15 Images of FORMOSAT-2 of Alert, Canada taken in Mar 2006

In the process of analyzing change detection, one helpful aspect is the fact of no-change in the vegetation cover. Usually it remains the same for a span of few days. This ensures the establishment of correlations among the daily revisit images taken by FORMOSAT-2. Similarly in Figure 5.15 the ice-bound area is again not subjected to change in daily revisits, only the rapture can be observed where change is taking place.

The area coverage by the image data provided by the RSI (Remote Sensing Instrument) is quite large 24 x 24 km, therefore image feature matching is not a problem in case of major features. The minor features are also identified correctly as the accuracy of Level-3 geometrically corrected image has been tested as 97.677% and 99.144 % for detailed

images like test images 1 and 2 shown in Figure 4.9, using cubic convolution resampling method.

5.5 Summary

In this chapter we discussed residual analysis of geometric correction technique, experimentation to check performance of various resampling methods and evocative application of geometrically corrected FORMOSAT-2 images for disaster investigation with examples from the recent past disasters occurring.

In analysis part, Level-3 geometric correction algorithm was evaluated using two approaches. The first approach was image to image matching and the second approach was point to point matching and error estimation. For this purpose eight points were randomly selected in all original image from Google Earth, Level-2 and Level-3 geometrically corrected images. In image to image analysis errors were found reduced from 438.3470 to 354.9952 by applying geometric correction technique. Whereas, in point to point analysis, *mse* for *x* and *y* coordinates for Level-2 PPM was 1.9801425/ 10.1630875 and for Level-3 geometric correction technique was 0.677126/ 5.44588625 respectively showing 50% reduction along both the axes of the image.

During experimentation process, three conventional 2-D interpolation methods were evaluated and analysed. Cubic convolution method was proved to be the best result orienting image transformation method. *Rms* of CC method was closest to the *rms* of the original images. There was 97.677% and 99.144 % resemblance for Islamabad image (test image 1) and 96.66% and 94.4% resemblance for Abbottabad image (test image 2) in *x*- and *y*-coordinates. However, CC method was found computationally more complex than all other methods. The complexity and execution time for this method was determined $O(n^3)$ and 127

seconds¹, respectively. D-4 wavelet based filter gave a much optimized solution. Its *rms* was closer to the original image *rms* and its complexity was also less. Visually, the image obtained with this method resembles the image gained with CC. Therefore resampling based on D-4 filtration method is a good replacement for CC method in image pixel transformation.

The novel features of sun-synchronous daily revisit orbit of FORMOSAT-2, makes it an ideal satellite for observing change detection. The chronological three day images of New Orleans, USA taken in Sep 2005 and Alert, Canada taken in Mar 2006, demonstrate the advantages of the daily revisit orbit for disaster investigation and Level-3 geometric correction for its utilization in feature detection.

¹ Running time computed for this experiment is dependent on image resolution and efficiency of the computer.

Conclusions and Recommendations

6.1 Overview

Images acquired by any remote sensing platform such as MS scanner onboard a satellite, a photographic system in an aircraft, or any other platform, will have various geometric distortions. This problem is inherent in remote sensing, because it's an attempt to accurately represent the three-dimensional surface of the earth as a two-dimensional image. Sources of geometric distortion are rotation of the earth during image acquisition, finite scan rate of some sensors, wide field of view of some sensors, curvature of the earth, non-ideal behavior of sensors, variations in platform altitude and velocity, and panoramic effects related to the imaging geometry [160].

Research reported in this thesis is specifically related to the geometric correction of FORMOSAT-2 satellite imagery. Though geo-referencing and correction of the images of FORMOSAT-2 satellite was initially carried out by National Space Program Organization (NSPO) of Taiwan which were termed as Level-2 correction. Level-2 correction of satellite images mean only radiometric corrections and no geometric corrections. There was a dire need for geometric corrections which are called as Level-3 image products. Although, pixel projection method (PPM) developed exists for the purpose of Level-2 corrections in its original form. This original version was however, not sufficient to obtain geometric corrections in satellite imagery. PPM was modified with the introduction of GCPs and least squares methods to obtain precise geo-referencing and to remove geometric distortions.

GCPs were introduced in PPM for accurate geo-referencing and least square regression was introduced to remove instrument bias or attitude distortions. Hence with the development of this approach, geometric corrections in FORMOSAT-2 satellite images were achieved.

Conventional ortho-rectification method of geo-referencing being carried out with the help of GCPs was described in Chapter 2. It geo-locates a remotely sensed image. The method suffers from, cumbersome procedure of selection of GCPs, poor precision in its matching with remotely sensed images, non-updation of maps and its correlation with imagery. The PPM of NSPO which is based on vertices matching of the image and its geodetic co-locations alongwith its mathematical model was explained in Chapter 3. Enhancement of PPM with least squares adjustment and its mathematical modeling was explained in Chapter 4. Residual analysis, experimentations consisting of resampling of digital imagery with conventional approximation techniques and a unique Daubechies-4 (D-4) filtration method were given in Chapter 5. The application of this new method was also discussed in the same chapter.

In this chapter we summarize our research work with objectives, goals achieved and limitations. Future work and recommendations envisaged specifically for FORMOSAT-2 imagery and other RS satellite systems are also given in this chapter.

6.2 Achievements and Applications

The major objective of this research work was to geometrically correct RS imagery. It is important to segregate geo-referencing and geometric correction here. Geo-referencing geo-locates the RS image to its ground coordinates, whereas geometric correction removes the distortions caused by different sources in a RS image. Geo-referencing is global in nature as the method of geo-locating is applied on the whole image. Geometric correction is local in

nature as it corrects and locates every pixel of the image to its exact ground location. In this way geo-referencing becomes part of precise geometric correction. Original version of PPM could only geo-reference FORMOSAT-2 imagery by matching the vertices of satellite image to its geodetic ground coordinates. In Level-3 geometric correction techniques precise geo-referencing was achieved with the help of GCPs incorporation and removal of geometric errors caused by attitude variation was obtained with the introduction of least squares adjustments.

The sub-image or local correction could have been achieved with the incorporation of Lagrange Multiplier. It was initially considered but there were two problems incorporating Lagrange Multiplier. One the cumbersome mathematical formulation and implementation in case of digital imagery and second, the starting point of the algorithm might have been an issue. This method would have been of high sensitive nature because of initial guess problem. In this scenario we suggested the solution by Least Square Method. With this method, the problem of geometric distortion caused by attitude change was successfully resolved.

PPM was initially using BI method for pixel value resampling in output image. We instead tested and applied all three conventional methods of interpolations (NN, BI and CC). It was concluded that in the process of pixel value transformation CC method has the most efficient results. On the contrary, it has more computational complexity and takes considerable running time. It deemed necessary to develop another method of resampling which has less complexity/ running time and more excellent visual interpretation results. For this purpose D-4 wavelet based method was used which gave excellent results. D-4 filter comprised of 2 x 4 pixel kernel based on 4 wavelet and 4 scaling coefficients. Results

achieved with this filter (given in Chapter 5) are close to CC method with computational complexity of function and execution time much reduced, almost equivalent to BI method. Its analysis proved that it can be a good replacement for CC method with a much lower cost.

This method of Level-3 geometric correction of FORMOSAT-2 images can be subsequently utilized for applications like disaster investigation, environmental monitoring, vegetation evaluation and multi-temporal image matching. In this dissertation we focused on the application of geometrically corrected imagery for disaster investigation. Different FORMOSAT-2 images were presented to show the disasters occurring around the world. These can be further investigated by continuous monitoring and analysis. The main purpose of this application is to minimize destruction from future mass scale disasters like earthquake, thunder storms, floods etc. The application is also useful for monitoring effects like environmental changes, vegetation evaluation and town planning etc.

6.3 Limitations

There are two major features of our algorithm for Level-3 geometric corrections but on the contrary these are limiting features for the algorithm also. The procedure of Level-3 geometric corrections developed is based upon availability of two things. First the ancillary data from the satellite and second the Google Earth software for finding out on-line GCPs.

PPM was originally based on the availability of ancillary data in the form of a dim file. PPM extracts information about image vertices, orbital velocity and attitude angles from ancillary data. Therefore, availability of FORMOSAT-2 ancillary data is a must for execution of Level-3 geometric correction technique of PPM.

Similarly for precision of geo-referencing, selection of GCPs from Google Earth is an important step of Level-3 geometric correction procedure. For our research, we were

dependent on this software because digital map of Pakistan was not available. Selection of GCPs from conventional maps would have made the procedure very cumbersome and exhaustive. Google Earth software was selected because of its free on-line availability. On-line connection of Google Earth is a must to obtain GCPs and their incorporation for geometrically correcting an image.

6.4 Recommendations and Future Research

The contributions in this thesis can be further extended in several interesting and fruitful directions. These are categorized into two parts, improvements related specifically to FORMOSAT-2 images and improvements related to other RS satellites.

6.4.1 Specific to FORMOSAT-2 Imagery

The innovative characteristic of sun-synchronous and daily revisit orbit makes FORMOSAT-2 an ideal satellite for site surveillance. The unique orbit and the arrangement of the CCD lines onboard FORMOSAT-2, however, have also raised new challenges in image processing. Level-3 geometric correction described in this thesis enables us to automatically handle a set of multi-temporal images with high spectral fidelity at high spatial resolution. Therefore, these are ideal for the analysis of change detection. Whatsoever technique is adopted for change detection but a precise method of geometric correction is a must.

Researchers are however encouraged to take on the issues given in subsequent sub sections while planning to carry on research on remotely sensed images obtained from FORMOSAT-2 satellite.

6.4.1.1 Band to Band Co-registration

Images gained from FORMOSAT-2 are multi-temporal and multi-spectral. Though

their geometric correction with precision in geo-referencing has been catered for by the Level-3 geometric correction technique but the issue of band to band co-registration warrant special attention especially in multi-spectral images. The accurate band to band co-registration is a prerequisite to generate a high quality image. This can be considered as a major problem of image processing of FORMOSAT-2 images after achieving geometric correction. The image matching techniques is one of the methods to be developed for band to band co-registration and can be applied to match multi-temporal images. In this way, the advantages of FORMOSAT-2 daily revisit imagery can be fully exploited for site surveillance, disaster monitoring and vegetation index observations.

6.4.1.2 Digitized Map of Pakistan

Although satellite images of different parts of Pakistan are available from FORMOSAT-2 satellite, but digitized map of Pakistan is not available. Therefore, Level-3 geometric correction technique was specially modified to incorporate Google Earth software to obtain geodetic coordinates of different locations of Pakistan. It is recommended that Level-3 geometric correction technique may be based on digital map to avoid dependence on Google Earth. Of course, this would require digital map of area under consideration.

6.4.1.3 Other Causes of Geometric Distortions

FORMOSAT-2 is able to point to $\pm 45^{\circ}$ along track and $\pm 45^{\circ}$ across track viewing by rotating the entire satellite rather than the sensor (RSI) itself. Therefore, the pointing range of FORMOSAT-2 is much larger than the pointing range of other modern RS satellite like ASTER. But with this, the orbital stability of FORMOSAT-2 gets much worse. It shows that FORMOSAT-2 satellite is more susceptible to distortions caused by the change in attitude or bias of the satellite. Therefore, while designing and developing Level-3 geometric correction

technique for FORMOSAT-2, this very cause of geometric distortion that is attitude distortion or instrument bias was kept in view.

Other causes of geometric distortion include rotation of the earth during image acquisition, finite scan rate and field of view of sensor, curvature of the earth, variations in platform velocity and panoramic effects related to the imaging geometry. It is therefore recommended that future research must be carried out for rectification of geometric distortion caused by any of these reasons.

6.4.2 Other Remote Sensing Satellites and Challenges to Image Processing and Analysis

Though, Level-3 geometric correction technique given in this thesis is specific to FORMOSAT-2 satellite because of using its ancillary data (DIMAP file). Opportunities still exist for extending the capabilities and applications of the proposed approach to RS satellites other than FORMOSAT-2 and Synthetic Aperture Radars (SAR). Several enhancements to the automatic geometric correction of RS images are possible. However, in principle the technique presented in this thesis can be utilized with some modifications. A number of issues are at hand which warrant considerations.

6.4.2.1 Different Resolutions

The difference in resolutions is an issue that arises when treating multi-source satellite data such as Landsat ETM+ and Aqua MODIS or SAR like RADARSAT-2. In this situation, the analyst must decide, for example what common pixel size will be used when co-registering the data, since either resolution or coverage will normally be sacrificed. Clearly this decision will be based on the need of a particular application and is a challenge more to the analyst than the algorithms. Besides having an algorithm for geometric correction

at hand, in this case co-registration of different resolutions will remain to be the major area of concern.

6.4.2.2 Techniques for Machine Assisted Interpretation

A lot of progress has been made to prepare machine assisted programs to interpret RS data. Machine assisted interpretation handles collection of tasks at the same time including pseudo coloring, radiometric correction, noise reduction and geo-referencing. Each one of these procedures involves a set of techniques [161]. For these procedures, machine assisted interpretation may be designed for a specific technique. Besides these procedures, key concern will remain the geometric correction of RS imagery. Even if a technique for geometric correction is adopted in machine assisted interpretation programs, it will be restricted to a specific cause of geometric distortion. So the problem of geometric correction will remain a major cause of worry for the interpreters and the analysts. It is therefore recommended that researchers must be encouraged to deal with the problem of geometric distortion in a highly structured way. Level-3 geometric correction technique can be enhanced and upgraded to deal with the geometric distortions of other RS satellites and other causes of geometric distortions besides attitude bias problem.

6.4.2.3 Multi-source and Multi-sensor Images

The issue of interpretation and analysis is even more complicated with the processing of multi-source and multi-sensor images at the same time. If a country like Pakistan obtains satellite imagery from different sources where sensors will also be different, an up-hill task for the analyst would be to process these images simultaneously. In this case, RS data available will be in different formats and will be based on different geodetic coordinate systems. Main hitch in such a case would be their precise geo-referencing and geometric

correction. Level-3 geometric correction technique is mainly devised for RSI on board FORMOSAT-2 satellite, has the scope for further enhancement of computational procedure for other sensors. This is another area in which future research can be carried out.

6.5 Summary

After the launch of FORMOSAT-2, the processing of its RSI recorded images was the next target. Level-1A raw image data was successfully transformed into Level-2 product through PPM by NSPO. Level-2 products were radiometrically corrected images only. Obtaining geometrically corrected images was a difficult task. Geometrically corrected images are classified as Level-3 images by the RS image analysts.

The primary aim of this thesis was to work out Level-3 geometric correction of FORMOSAT-2 images. This aim was achieved with the help of precise geo-referencing and correction of geometric distortions caused by the attitude change of the satellite. For this purpose Level-3 geometric correction technique was designed modifying original PPM. For precise geo-referencing ground coordinates and GCPs were obtained from Google Earth and attitude angles correction were attained by applying least squares adjustments. The technique was a new approach based on combination of precise geo-referencing and correction of attitude biased distortions. Test images were acquired from FORMOSAT-2 with the courtesy of NSPO, Taiwan.

In the process of geometric correction, resampling/ transformation of image pixels was accomplished using four 2-D interpolation methods. Each approximation method with its merits and demerits has been discussed and tested. Initially the three conventional approximation techniques (NN, BI and CC) were applied. CC method was found to be the best approximation technique but with increased computational complexity and execution

time. Then wavelet based D-4 filtration method was applied for more encouraging results. Outcomes of this method showed that its *rms* was closer to the original ground coordinated image. Its complexity and execution time were much lesser than CC scheme but with a matching visual interpretation as CC scheme. Thus resampling based on D-4 filtration scheme was found superior to CC method for image pixel transformation.

FORMOSAT-2 images are perfect for the analysis of change detection and its effectiveness in applications like disaster investigation. The chronological three day images of New Orleans, USA and Alert, Canada demonstrated the advantages of the daily revisit orbit and Level-3 geometric correction for its effective utilization in disaster monitoring.

Appendix A: Two-dimensional Coordinate Transformation

A-1 Introduction

An encountered problem in photogrammetry is conversion from one coordinate system to another. This is because photogrammetrists commonly determine coordinates of unknown points in convenient arbitrary rectangular coordinate systems. These arbitrary coordinates may be read from comparators or stereoscopic plotters, or they may result from analytic computation. The arbitrary coordinates must then be converted to a final system, such as the camera photo coordinate system in the case of comparator measurements, or to a ground coordinate system, such as the state plane coordinate system in the case of stereoplotter or analytically derived arbitrary model coordinates. The procedure for converting from one coordinate system to another is known as coordinate transformations. The procedure requires that some points have their coordinates known (or measured) in both the arbitrary and final coordinate systems. Such points are called control points.

A-2 Two-dimensional Conformal Coordinate Transformation

The term two-dimensional means that the coordinate system lay on plane surfaces. A conformal transformation is one in which true shape is preserved after transformation. To perform a two-dimensional conformal coordinate transformation, it is necessary that coordinates of at least two points be known in both the arbitrary and final coordinate systems. Accuracy in the transformation is improved by choosing the two points as far apart as possible. If more than two control points are available, an improved solution may be obtained by applying the method of least squares.

A two-dimensional conformal coordinate transformation consists of three basic steps: (1) scale change, (2) rotation, and (3) translation. The example illustrated in Figure A-1 is used to demonstrate the procedure. This example uses the minimum of two control points. Figure A-1 (a) shows the positions of points a through c , whose coordinates are known in an arbitrary XY system. Figure A-1 (b) illustrates the position of the same points, labeled A through C in a (ground) EN system. The coordinates of A and B are known in the ground system, and it is required to determine the coordinates of C in the ground system.

A-3 Scale Change

By comparing Figure A-1 (a) and (b), it is evident that the lengths of lines ab and AB are unequal; hence the scales of the two coordinate systems are unequal. The scale of the XY system is made equal to that of the EN system by multiplying each X and Y coordinate by a scale factor s . The scaled coordinates are designated as X' and Y' . By use of the two control points, the scale factor is calculated in relation to the two lengths AB and ab as

$$s = \frac{AB}{ab} = \frac{\sqrt{(E_B - E_A)^2 + (N_B - N_A)^2}}{\sqrt{(X_b - X_a)^2 + (Y_b - Y_a)^2}} \quad (\text{A-1})$$

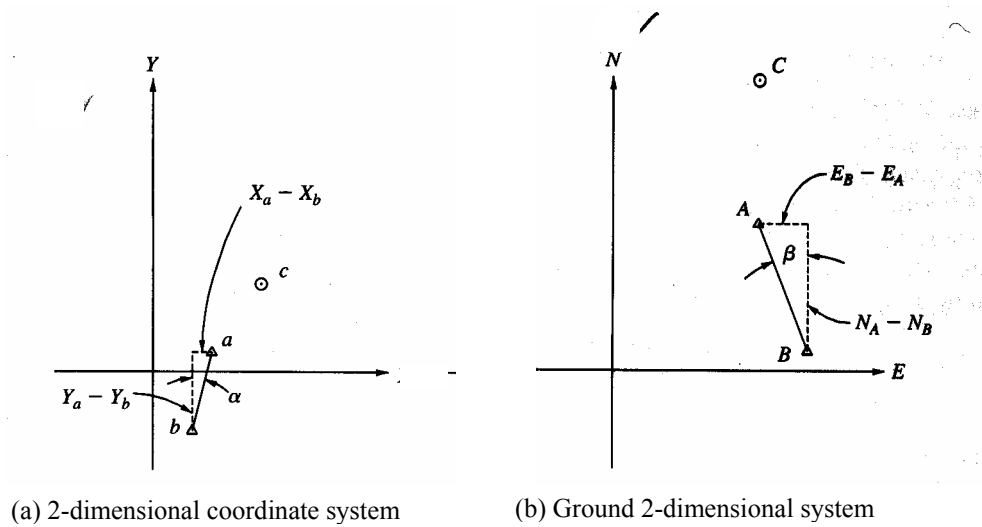


Figure: A-1 Comparison of two dimensional coordinate system with ground system.

A-4 Rotation

If the scaled $X'Y'$ coordinate system is superimposed over the EN system of Figure A-1 (b) so that line AB in both systems coincides, the result is as shown in Figure A-2. An auxiliary axis system $E'N'$ is constructed through the origin of the $X'Y'$ axis system parallel to the EN axes. It is necessary to rotate from the $X'Y'$ system to $E'N'$ system, or in other words, to calculate $E'N'$ coordinates for the unknown points from their $X'Y'$ coordinates. The $E'N'$ coordinates of point C may be calculated in terms of the clockwise angle θ by using the Equations A-2:

$$\begin{aligned} E'_C &= X'_C \cos \theta - Y'_C \sin \theta \\ N'_C &= X'_C \sin \theta + Y'_C \cos \theta \end{aligned} \tag{A-2}$$

Rotation angle θ , shown in Figure A-2 is the sum of angles α and β which are indicated on Figure A-1 (a) and (b). From coordinates of the two control points, these angles are calculated as

$$\begin{aligned} \alpha &= \tan^{-1} \left(\frac{X_a - X_b}{Y_a - Y_b} \right) \\ \beta &= \tan^{-1} \left(\frac{E_B - E_A}{N_A - N_B} \right) \end{aligned} \tag{A-3}$$

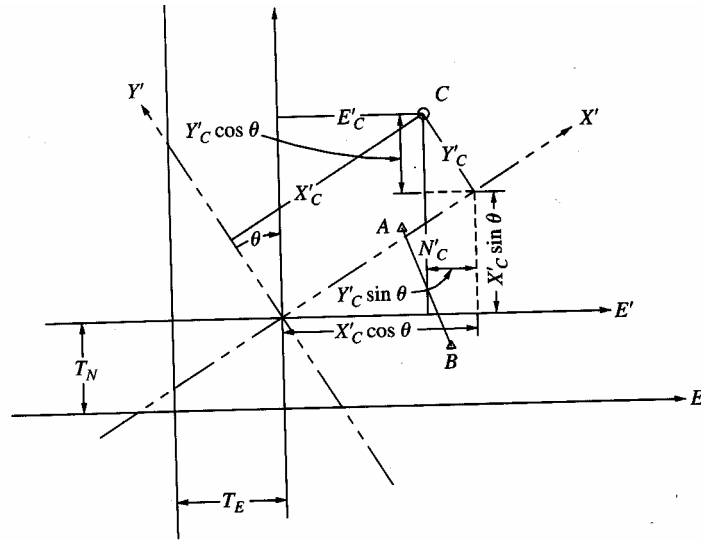


Figure: A-2 Scaled $X'Y'$ coordinate system and its superimposition onto the EN ground coordinate system.

A-5 Translation

The final step in the coordinate transformation is a translation of the origin of the $E'N'$ system to the origin of the EN system. The translation factors required are T_E and T_N , which are illustrated in Figure A-2. Final E and N ground coordinates for points C then are

$$\begin{aligned} E_C &= E'_C + T_E \\ N_C &= N'_C + T_N \end{aligned} \quad (\text{A-4})$$

where the translation factors TE and TN are calculated as

$$\begin{aligned} T_E &= E_A - E'_A = E_B - E'_B \\ T_N &= N_A - N'_A = N_B - N'_B \end{aligned} \quad (\text{A-5})$$

From Equation A-5, these translation factors may be calculated in two different ways by using either control point A or B . It is advisable to calculate them by using both points, to obtain a computation check.

Appendix B: Digital Resampling

B-1 Introduction

There are several techniques available for resampling digital images, although three particular ones are by far, most prevalent. They are known as nearest neighbor interpolation, bilinear interpolation and bicubic interpolation. Other, more computationally intensive techniques are generally not employed since they tend to be sensitive to sensor noise which exists in digital imagery.

B-2 Nearest Neighbor

The nearest neighbor interpolation is simplest of the three. As its name implies, the Digital Number (DN) chosen will be that of the image pixel whose center is closest to the center of the grid cell. From a computational standpoint, all that is required is to round off the fractional row and column values to the nearest integral value.

B-3 Bilinear Interpolation

A second resampling method, which involves greater computational complexity, is bilinear interpolation. In this approach, the four surrounding pixels are selected, and linear interpolation is performed in two directions.

B-4 Bicubic Interpolation

Bicubic interpolation also known as cubic convolution is a third resampling technique which is commonly used. Explanation of this technique requires a little background in sampling theory. First an assumption is made that the original signal has been sampled above the Nyquist rate, which is generally satisfied for imaging sensors. The Nyquist rate is, in essence, the sampling frequency required to faithfully record the highest (spatial) frequency content of the scene. Given this assumption, the sinc function allows an exact reconstruction of the original scene. The form of the sinc function is shown in Figure B-1. (Note that in this figure, the argument for the sine function is in radians). If the images had an infinite number of rows and columns, and all pixels were used for the interpolation, the sinc function would yield a perfect reconstruction. Practicality, however, dictates that interpolations are carried out using only small neighborhoods surrounding the interpolated pixel. A cubic spline approximation to the sinc function is the form generally used for bicubic interpolation. The

shape of the spline is given in Figure B-2. For comparison, Figure B-2 also shows the shape of the nearest neighbor and bilinear interpolations expressed in the form of similar weighting functions. Note that the cubic spline most nearly approximates the sinc function of Figure B-2, whereas bilinear and nearest neighbor interpolation are less consistent approximations.

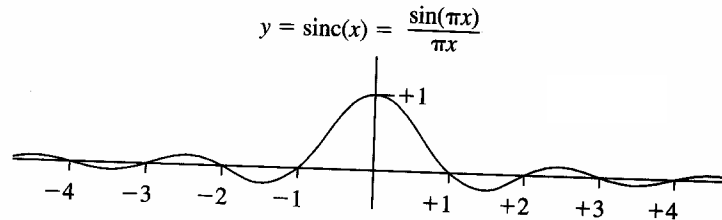


Figure: B-1 Form of the sinc function

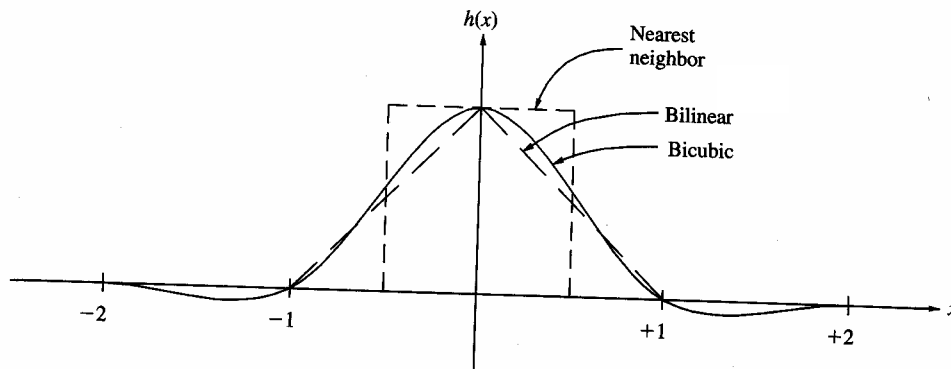


Figure: B-2 Shape of the bicubic, bilinear and nearest neighbor interpolations

Equations B-1 to 3 express the functional relationship of the spline.

$$f_1(x) = (a + 2)x^3 - (a + 3)x^2 + 1 \quad \text{for } 0 \leq x \leq 1 \quad (\text{B-1})$$

$$f_2(x) = ax^3 - 5ax^2 + 8ax - 4a \quad \text{for } 1 \leq x \leq 2 \quad (\text{B-2})$$

$$f_3(x) = 0 \quad \text{for } x \geq 2 \quad (\text{B-3})$$

where a = free parameter equal to slope of weighting function at $x = 1$ (generally $a = -0.5$ yields best results)

x = absolute value of difference between whole-number row or column and fractional row and column

The computational process is analogous to that of bilinear interpolation in that it is performed first along the rows and then down the single, fractional column. The computations are conveniently expressed in matrix form as shown in Equation B-4 below. In this equation, the R and C matrices consist of coefficients derived from Equations B-1 and B-2, and the D matrix contains the digital numbers from the 4 x 4 neighborhood surrounding the interpolated pixel.

$$RDC = \begin{bmatrix} r_1 & r_2 & r_3 & r_4 \end{bmatrix} \begin{bmatrix} d_{11} & d_{12} & d_{13} & d_{14} \\ d_{21} & d_{22} & d_{23} & d_{24} \\ d_{31} & d_{32} & d_{33} & d_{34} \\ d_{41} & d_{42} & d_{43} & d_{44} \end{bmatrix} \begin{bmatrix} c_1 \\ c_2 \\ c_3 \\ c_4 \end{bmatrix} \quad (\text{B-4})$$

Interpolating across the rows (based on the fractional column position) is done by forming the product DC . Subsequently, R is multiplied by the product to obtain the final interpolated value. In fact, the sequence of multiplication does not matter; they can be performed from left to right in Equation B-4.

$$\sum_{i=1}^m (w_i a_{in} a_{i1}) X_1 + \sum_{i=1}^m (w_i a_{in} a_{i2}) X_2 + \sum_{i=1}^m (w_i a_{in} a_{i3}) X_3 + \cdots + \sum_{i=1}^m (w_i a_{in} a_{in}) X_n = \sum_{i=1}^m (w_i a_{in} L_i) \quad (\text{C-9})$$

In Equations C-6 to C-9 the terms are as described previously, except the w_i 's are the relative weights of the individual observations.

C-2 Matrix Methods in Least Square Adjustment

The least square computations are quite lengthy and are therefore most economically performed on a computer. The algebraic approach as given in Equations C-2 to C-5 and C-6 to C-9 for forming normal equations, and for obtaining their simultaneous solution, can be programmed for computer solution or set up in a computer spread-sheet. The procedure is much more easily adapted to matrix methods, however.

In developing matrix equations for least square computations, analogy will be made to the algebraic approach presented in Section C-1. First, observations Equation C-1 may be represented in matrix form as

$${}_m A^n {}_n X^1 = {}_m L^1 + {}_m V^1 \quad (\text{C-10})$$

Where

$${}_m A^n = \begin{pmatrix} a_{11} & a_{12} & a_{13} & \cdots & a_{1n} \\ a_{21} & a_{22} & a_{23} & \cdots & a_{2n} \\ a_{31} & a_{32} & a_{33} & \cdots & a_{3n} \\ a_{41} & a_{42} & a_{43} & \cdots & a_{4n} \\ \cdots & \cdots & \cdots & \cdots & \cdots \\ a_{m1} & a_{m2} & a_{m3} & \cdots & a_{mn} \end{pmatrix}$$

$${}_n X^1 = \begin{bmatrix} X_1 \\ X_2 \\ X_3 \\ \vdots \\ X_n \end{bmatrix}$$

$${}_m L^1 = \begin{bmatrix} L_1 \\ L_2 \\ L_3 \\ \vdots \\ L_m \end{bmatrix}$$

$${}_m V^1 = \begin{bmatrix} V_1 \\ V_2 \\ V_3 \\ \vdots \\ V_m \end{bmatrix}$$

Upon studying the following matrix representation, it will be noticed that normal Equations C-2 to C-5 are obtained as follows:

$$(A^T A)X = A^T L \quad (\text{C-11})$$

In Equation C-11, $A^T A$ is the matrix of normal equation coefficients of the unknowns. Pre-multiplying both sides of Equation C-5 by $(A^T A)^{-1}$ and reducing, results in:

$$(A^T A)^{-1} (A^T A)X = (A^T A)^{-1} (A^T L) \quad (C-12)$$

$$IX = (A^T A)^{-1} (A^T L) \quad (C-13)$$

$$X = (A^T A)^{-1} (A^T L) \quad (C-14)$$

In Equation C-13, I is the identity matrix. Equation C-14 is the basic least squares matrix equation for equally weighted observations. The matrix X consists of most probable values for unknowns $X_1, X_2, X_3, \dots, X_n$. for a system of weighted observations, the following matrix equation provides the X matrix of most probable values for the unknowns:

$$X = (A^T W A)^{-1} (A^T W L) \quad (C-15)$$

In Equation C-15 the matrices are identical to those of the equally weighted equations, with the inclusion of the W matrix, which is a diagonal matrix of weights and is defined as follows:

$$W = \begin{bmatrix} w_1 & 0 & 0 & \cdots & 0 \\ 0 & w_2 & 0 & \cdots & 0 \\ 0 & 0 & w_3 & \cdots & 0 \\ \cdots & \cdots & \cdots & \cdots & \cdots \\ 0 & 0 & 0 & \cdots & w_m \end{bmatrix} \quad (C-16)$$

In Equation C-16 W matrix, all off-diagonal elements are shown as zero. This is proper when the individual observations are independent and uncorrelated; i.e., they are not dependent upon each other. This is often the case in photogrammetric applications.

References

- [1] R. A. Schowengerdt, *Remote Sensing, Models and Methods, for Image Processing*, Second Edition, Academic Press, Elsevier, USA, 1997.
- [2] T. M. Lillesand and R. W. Kiefer, *Remote Sensing and Image Interpretation*, Fourth Edition, John Wiley and Sons Inc, Singapore, 2003.
- [3] P. R. Wolf and B. A. Dewitt, *Elements of Photogrammetry with Applications in GIS*, Third Edition, Macgraw Hill, USA, 2000.
- [4] E. Avery and G.L. Berlin, *Fundamentals of Remote Sensing and Airphoto Interpretation*, Fifth Edition, Macmillan Publishing Company, New York, USA, 1992.
- [5] W. K. Pratt. *Digital Image Processing*, John Wiley and Sons, New York, 1978.
- [6] G. Dial, and J. Grodecki, "Satellite image block adjustment simulations with physical and RPC camera models", in *Proc. ASPRS Annual Conf.*, Colorado, USA, 2004 pp 151-169.
- [7] W. Zhang and Z. Li, "Rectification of airborne line-scanner imagery utilizing flight parameters", in *Proc. First Intl. Airborne Remote Sensing Conf. and exhibition, Strasbourg*, France, 1994, pp 447-456.
- [8] Y. Y. Lee, A. M. Wu and F. Wu, "An algorithm for geometric correction of high resolution image based on physical modeling," [Online document] 2002 Jan 14, Available www.gisdevelopment.com
- [9] J. R. Schott, *Remote Sensing-The Image Chain Approach*, Oxford University Press, New York, 1997.
- [10] NSPO, "Rocsat-2 remote sensing mission," [Online documents], 2007 July 1, Available: <http://www.nspo.org.tw/e60/menu0403.html>.
- [11] R. J. Lyon, "Remote sensing: visions beyond sight", *Stanford Today Series*, vol. 1, no. 17, pp. 2-7, 1966.
- [12] J. A. Richards and X. Jia, *Remote Sensing Digital Image Analysis*, Fourth Edition, Springer, Germany, 2006.
- [13] Paul M. Mather, *Computer Processing of Remotely-Sensed Images*, Second Edition, Wiley Publishing Inc., West Sussex, England, 1999.

- [14] B. Robertson, "Rigorous geometric modeling and correction of QuickBird imagery", in *Proc. of IGARSS 2003, Toulouse*. France, 21-25 July, 2003, pp.2166-2175.
- [15] T. Toutin, "Review Paper: Geometric processing of remote sensing images: models, algorithms and methods", *Intl. Journal of Remote Sensing*, vol. 25, no 10, 1893-1924, 2004.
- [16] W. Wolnicwicz, "Assessment of geometric accuracy of VHR satellite images", *Intl. Archives of Photogrammetry and Remote Sensing and Spatial Information Sciences*, vol. 35 no. B1, pp.19-23, 2004.
- [17] T. Toutin, "Error tracking in IKONOS geometric processing using a 3D parametric modelling", *Photogrammetric Engineering and Remote Sensing*, vol. 69, no. 1, pp. 43-51, 2003.
- [18] A. M. Wu, Y. Y. Lee, P. Kuo, and R. Kao, "ROCSAT-2 imaging planning and scheduling," *presented at the 1st Taipei Int. Conf on Digital Earth*, Taipei, Taiwan, 2003.
- [19] O. Montenbruck and E. Gill, *Satellite Orbits-Models, Methods and Applications*, Springer, New York, USA, 2001.
- [20] W. G. Rees, *Physical Principles of Remote Sensing*, Second Edition. Cambridge, U.K.: Cambridge Univ. Press, 2001.
- [21] R. Haydan, G. W. Dalke, J. Henkel, and J. E. Bare, "Applications of the IHS colour transform to the processing of multisensor data and image enhancement," *presented at the Int. Symposium Remote Sensing Arid and Semi-arid and Lands*, Cairo, Egypt, 1982.
- [22] J. G. Liu and J. Ma, "Imageodsey on MPI and GRID for co-seismic shift study using satellite optical imagery," *presented at the UK e-Science All Hands Meeting*, Nottingham, U.K., 2004.
- [23] J. Cihlar, T. J. Pultz, and A.L. Gray "Change detection with synthetic aperture radar", *Intl. Journal of Remote Sensing*, vol. 13, no. 3, pp. 401-414,1992.
- [24] P. Nonin, and S. Piccard, "Performance analysis of DEM automatic extraction from SPOT5 sensors", in *Proc. of IGARSS '03*, Toulouse, 2003, pp.309-311.
- [25] A. B Orun, and K. Natarajan, "A modified bundle adjustment software for SPOT imagery and photography: Tradeoff", *Photogrammetric Engineering and Remote Sensing*, vol. 60, no. 12, pp. 1431-1437, 1994.
- [26] Sovzond, "Accurate Image of the world", [Online document] 2007 May 3, Available: <http://www.sovzond.ru/en/satellites/france/771.html>.

- [27] H.D. Curtis, *Orbital Mechanics for Engineering Students*, Elsevier Aerospace Engineering Series, Burlington, USA, 2005.
- [28] M. Unser, "Splines: A perfect fit for signal and image processing," *IEEE Signal Processing Magazine*, vol. 16, pp. 22–38, Nov. 1999.
- [29] E.W. Cheney and W. A. Light, "Quasi-interpolation with basis functions having noncompact support," *Constructing Approximations*, vol. 8, pp. 35–48, 1992.
- [30] Z. Mao, D. Pan, H. Huang, and W. Huang, "Automatic registration of SeaWiFS and AVHRR imagery," *Intl. Journal of Remote Sensing.*, vol. 22, no. 15, pp. 1725–1735, 2001.
- [31] A. M. Wu and Y. Y. Lee, "Geometric correction of high resolution image using ground control points," in *Proc. 22nd Asian Conf. on Remote Sensing*, Singapore, 2001, pp 162-166.
- [32] M. Erdogan, O. Eker, A. Yilmaz and O. Aksu, "Orthorectification of SPOT images with the same-pass constraints," in *Proc. of XXth ISPRS Congress*, Istanbul, Turkey, 2004, pp 415-419.
- [33] T. Toutin, "Error tracking in IKONOS geometric processing using a 3D parametric model," *Photogrammetric Engineering and Remote Sensing*, vol. 69 no. pp. 43-51. 2003.
- [34] T. Toutin and A.L. Gray, "State-of-the-art of extraction of elevation data using satellite SAR data," *ISPRS Journal of Photogrammetry and Remote Sensing*, vol. 55, no. 1, pp. 13-33, 2000.
- [35] H. Chen, F. Wu, and C. Liu, "Introduction of ROCSAT-2 terminal," *presented at the 23rd Conf. Surveying Theories and Applications*, Taichung, Taiwan, 2004.
- [36] C. Liu, S.C.Wu, F.T. Hwang, A.M.Wu, and H. Chen, "Radiometric and geometric calibration of ROCSAT-2 image," *presented at the 25th Asian Conf. Remote Sensing*, Chiang Mai, Thailand, 2004.
- [37] C.C. Liu, C.A. Wu, M.L. Shieh, J.G. Liu, C.W. Lin, and C.L. Shieh, "Monitoring the illegal quarry mining of gravel on the riverbed using daily revisit FORMOSAT-2 imagery," *Intl. Geosciences and Remote Sensing Symposium.*, Seoul, Korea, 2005, pp. 1777–1780.
- [38] C.C. Liu, J.G. Liu, C.W. Lin, A.M. Wu, S.H. Liu, and C.L. Shieh, "Image processing of FORMOSAT-2 data for monitoring South Asia tsunami," *Intl. Journal of Remote Sensing* to be published.

- [39] M. N. Demers, *Fundamental of Geographic Information Systems*, Second Edition, John Wiley and Sons Inc, Singapore, 2002.
- [40] D.M. Tsai and C.T. Lin, “Fast normalized cross correlation for defect detection,” *Pattern Recognition Letters*, vol.24, no. 15, pp. 2625-2631, Nov 2003.
- [41] J. L. Moigne, W. J. Campbell, and R. F. Crompt, “An automated parallel image registration technique based on the correlation of wavelet features,” *IEEE Transactions on Geosciences and Remote Sensing*, vol. 40, no. 7 pp.1849–1864, 2002.
- [42] C.C. Liu, “Processing of FORMOSAT-2 imagery for site surveillance,” in *Proc. 26th Asian Conf. Remote Sensing*, Hanoi, Vietnam, 2005, pp. 3206-3214.
- [43] C. C.Liu. “Processing of FORMOSAT-2 daily revisit imagery for site surveillance,” *IEEE Transactions on Geosciences and Remote Sensing*, vol.44, no. 11, pp. 3206-3214, 2006.
- [44] A. Iwasaki, H. Fujisada, and S. Tsujimoto, “ASTER geometric performance,” in *Proc. SPIE—Sensors, Systems, and Next-Generation Satellites*, vol. 4540, 2001, pp. 27–38. DOI: 10.1117/12.450692.
- [45] A. Iwasaki and H. Fujisada, “ASTER geometric performance,” *IEEE Transactions on Geosciences Remote Sensing*, vol. 43, no. 12, pp. 2700–2706, Dec. 2005.
- [46] K. Jacobsen, “Understanding geo-information from high resolution optical satellites,” *GIS Development*, vol. 10, no. 3, pp. 24-28, 2006.
- [47] F.W. Leberl, *Radargrammetric Image Processing*, Norwood, USA: Artech House, 1990.
- [48] Y. Cazaux, G. Boucharlat, and D. Subiela, “12000 pixel monolithic linear sensor for high resolution pushbroom Earth observation satellites,” in *Proc. 3rd ESA Electron Components Conf.*, Noordwijk, The Netherlands, 1997.pp.56-63.
- [49] Jet Propulsion Laboratory, California Institute of Technology, “Airborne visible/infrared imaging spectrometer” [Online document] 2006, Mar 29, Available: <http://www.aviris.jpl.nasa.gov/>.
- [50] A. Plaza *et al.*, “Parallel implementation of end member extraction algorithms from hyperspectral data,” *IEEE Geosciences and Remote Sensing Letters*. vol. 3, pp. 285–290, 2006.
- [51] C. I. Chang and A. Plaza, “A fast iterative algorithm for implementation of pixel purity index,” *IEEE Geosciences and Remote Sensing Letters*. vol. 3, pp. 63–67, 2006.

- [52] H.S Jung, S. W. Kim and J. S. Won, “The simple method of geometric reconstruction for SPOT images”, in *Proc. Intl. Symposium of Remote Sensing '04*, Jeju, S. Korea, 2004, pp. 205-207.
- [53] C. D. Boor, “Quasi-interpolation and approximation power of multivariate splines,” in *Proc. Computation of Curves and Surfaces*, (W. Dahmen Edition), Dordrecht: Kluwer, 1990, pp. 313–345.
- [54] F. Eugenio, “Automatic satellite image georeferencing using a contour-matching approach,” *IEEE Transactions on Geoscience and Remote Sensing*, vol. 41, no. 12, pp. 2869-2880, 2003.
- [55] X. Dai and S. Korran, “A feature-based image registration algorithm using improved chain-code representation combined with invariant moments,” *IEEE Transactions on Geosciences and Remote Sensing*, vol. 37, no 5, pp. 2351–2362, 1999.
- [56] H.S. Stone and R. Wolpov, “Blind cross-spectral image registration using prefiltering and fourier-based translation detection,” *IEEE Transactions on Geosciences and Remote Sensing*, vol. 40, no. 7, pp. 637–650, 2002.
- [57] Mikhail E.M., and F.Ackermann, *Observation and Least Squares*, University Press of America, New York, 1982.
- [58] V. Kratky, “Rigorous photogrammetric processing of SPOT images at CCM Canada”, *ISPRS Journal of Photogrammetry and Remote Sensing*, vol. 44, pp. 53-71, 1989.
- [59] R. G. Congalton, “Using spatial autocorrelation analysis to explore the errors in maps generated from remotely sensed data,” *Photogrammetric Engineering and Remote Sensing*. vol. 54, pp. 587–592, 1998.
- [60] J. Stuckens, P. R. Coppin, and M. E. Bauer, “Integrating contextual information with per-pixel classification for improved land cover classification,” *Remote Sensing Environment*, vol. 71, pp. 282 – 296, 2000.
- [61] A. Plaza, “Parallel Processing opens new perspectives for hyperspectral imaging”, [Online document], 2007, May 14, Available: <http://spie.org/aplaza/x8695.xml>.
- [62] A. Plaza *et al.*, “Spatial/spectral end member extraction by multidimensional morphological operations,” *IEEE Transactions on Geosciences and Remote Sensing*, vol 40, pp. 2025–2041, 2002.
- [63] N. A. Dodgson, “Quadratic interpolation for image resampling,” *IEEE Transactions on Image Processing*, vol. 6, pp. 1322–1326, Sept. 1997.

- [64] I. German, “Short kernel fifth-order interpolation,” *IEEE Transactions on Signal Processing*, vol. 45, pp. 1355–1359, May 1997.
- [65] A. Schaum, “Theory and design of local interpolators,” *CVGIP: Graphical Models Image Processing*, vol. 55, no. 6, pp. 464–481, Nov. 1993.
- [66] T. Blu, P. Thévenaz, and M. Unser, T. Blu, P. Thévenaz, and M. Unser, “MOMS: Maximal-order interpolation of minimal support,” *IEEE Transactions Image Processing*, vol. 10, pp. 1069–1080, July 2001.
- [67] I. J. Schoenberg, “Contribution to the problem of approximation of equidistant data by analytic functions,” *Quarterly Applied Mathematic*, vol. 4, no. 2, pp. 45–99 and 112–141, 1946.
- [68] A. Bouillon, E. Breton, F. De Lussy and R. Gachet, “SPOT5 geometric image quality”, in *Proc. of IGARSS '03*, Toulouse, 2003, pp.303-305.
- [69] L. Chen and Y. Wu, “Image geometric simulation and orientation modeling for Rocsat-2,” *Proc. of ACRS*, 2000, pp. 6-13.
- [70] T. Toutin, “Geometric processing of remote sensing images: models, algorithms and method”, *Intl. Journal of Remote Sensing*. vol. 25, pp. 1893 – 1924, 2004.
- [71] M. Noguchi, C.L. Fraser, T. Nakamura, T. Shimono and S. Oki, “Accuracy assessment of QuickBird stereo imagery”, *Photogrammetric Record*, vol 19, no 106, pp. 128-138, 2004.
- [72] F. Amhar, J. Jansa, and C. Ries, “The generation of true orthophotos using 3D building model in conjunction with a conventional DTM”, *Intl Archives of Photogrametry and Remote Sensing*, vol. 32, no.B4, pp. 16-22, 1998.
- [73] USFS Spectroscopy Lab, “Imaging Spectroscopy”, [Online document] 2007, Jan 8, Available: <http://speclab.cr.usgs.gov/>.
- [74] A. Plaza *et al.*, “Commodity cluster-based parallel processing of hyperspectral imagery”, *Journal of Parallel and Distributing Computing*, vol. 66, pp. 345–358, 2006.
- [75] NASA, Ames Research Centre, Moffett Field, USA, “Airborne Sensor Facility” [Online document] 2006, Jun 13, Available: <http://asapdata.arc.nasa.gov>.
- [76] F. Eugenio, F. Marqués, and J. Marcello, “Pixel and sub-pixel accuracy in satellite image georeferencing using an automatic contour matching approach,” in *Proc. IEEE Int. Conf on Image Processing*, Thessalonik, Greece 2001, pp. 822–I.825.

- [77] F. Eugenio, J. Marcello, F. Marqués, A. Hernández-Guerra, and E. Rovaris, "A real-time automatic acquisition, processing and distribution system for AVHRR and SeaWiFS imagery," *IEEE Geosciences and Remote Sensing Newsletter*, no. 120, pp. 10–15, 2001.
- [78] Y. Cazaux, D. Subiela, and G. Boucharlat, "12 000-pixel monolithic linear sensor for high-resolution push-broom Earth observation satellites," *presented at the Advanced and Next-Generation Satellites*, Paris, France, 1995.
- [79] A. Baudoin, "Beyond SPOT 5: Pléiades, part of the French–Italian program ORFEO," *Proc. of the 20th Intl. Archives Photogrammetry and Remote Sensing Congress.*, Istanbul, Turkey, 2004.pp-242-249.
- [80] J. B. Campbell, *Introduction to Remote Sensing*, Third Edition, Taylor & Francis, London, U.K, 2002.
- [81] W. G. Rees, *Physical Principles of Remote Sensing*, Second Edition, Cambridge University. Press, Cambridge, U.K, 2001.
- [82] P.P. Vaidyanathan, "Multirate digital filters, filter banks, polyphase networks, and applications: A tutorial", *Proc. of the IEEE*, vol. 78, no. 1, pp. 56-93, Jan. 1990.
- [83] D. R. Peddle, R. L. Johnson, J. Cihlar, and R. Latifovic, "Large area forest classification and biophysical parameter estimation using the 5-Scale canopy reflectance model in Multiple-Forward-Mode," *Remote Sensing Environment*, vol. 89, pp. 252– 263, 2004.
- [84] N. Chrysoulakis, M. Abrams, H. Feidas, and D. Velianitis, "Analysis of ASTER multispectral stereo imagery to produce DEM and land cover databases for Greek islands: The REALDEMS Project," in *Proc. E-Environment: Progress and Challenge*, Instituto Politecnico Nacional, Mexico, 2004, pp. 411–424.
- [85] T. Toutin, *Elevation Modeling from Satellite Data, Encyclopedia of Analytical Chemistry: Instrumentation and Application*, John Wiley & Sons Ltd., Chichester, UK, 2002.
- [86] K. T.Alfriend , W. J.Barnds , S. L.Coffey , L. M. Stuhrenberg, "Attitude and orbit determination of a satellite system", *Advances in the Astronautical Sciences*, vol. 90, pp. 95-351, 1995.
- [87] T. Westin, "Precision rectification of SPOT imagery," *Photogrammetric Engineering and Remote Sensing*, vol 56, no. 2, pp. 247-253, 1990.
- [88] J. J. Degnan, "Millimeter accuracy satellite laser ranging: "A review, contributions of space geodesy to geodynamics", *Technology, Geodynamics*, vol. 25, pp. 133-162, 1993.

- [89] J. W. Boardman, "Precision geocoding of low altitude AVIRIS data: Lesson learned in 1998". [Online document] 2001, Dec 29 Available: <http://popo.jpl.nasa.gov/pub/docu/workshops/99.pdf>.
- [90] J.S. Lee, "Digital image enhancement and noise filtering by use of local statistics", *IEEE Transactions on Pattern Analysis and Machine Intelligence*, vol. 2, pp. 165-168, 1980.
- [91] K. Nikolakopoulos, E. Kamaratakis, and N. Chrysoulakis, "SRTM vs ASTER elevation products. Comparison for two regions in Crete, Greece," *Intl. Journal of Remote Sensing*, to be published.
- [92] T. Toutin, "Elevation modeling from satellite VIR data: A Review", *Int. Journal of Remote Sensing*, vol. 22, pp. 1097 – 1125, 2001.
- [93] C. I. Jchang, *Hyperspectral Imaging: Techniques for Spectral Detection and Classification*, Kluwer, New York, 2003.
- [94] L.C. Chen, C.-Y. Lo and J.Y. Rau, "The generation of true orthophotos from IKONOS GEO images", in *Proc. of the ACRS, GIS Development*, Katmandu, Nepal, Nov 25-29, 2002, pp. 7-11.
- [95] J.C Curlander, "Location of spaceborne SAR imagery", *IEEE Transaction on Geosciences and Remote Sensing*, vol. 22, pp. 106-112, 1982.
- [96] C. H. Davis and X. Wang, "Planimetric accuracy of IKONOS 1-m panchromatic image products", in *Proc. of the ASPRS Annual Conf.*, St Louis, Missouri, USA, April 23-27, 2001, pp. 677-683.
- [97] T. Kersten, E. Baltsavias, M. Schwarz. and I. Leiss, "IKONOS-2 Cartera Geo – Erste geometrische genauigkeitsuntersuchungen in der schweiz mit hochaufgeloesten satellitendaten", *Vermessung, Photogrammetrie, Kulturtechnik*, vol. 8, pp. 490-497, 2000.
- [98] J. Grodecki and G. Dial, "Block adjustment of high-resolution satellite images described by rational polynomial", *Photogrammetric Engineering and Remote Sensing*, vol. 69, no 1, pp. 59-68, 2003.
- [99] V.A. Chobotov, *Spacecraft Attitude Dynamics and Control*, Krieger Publishing company, Malabar, Florida, USA, 1991.
- [100] R.J Brown., B. Brisco, R. Leconte, D.J. Major, J.A. Fischer, G. Reichert, K.D. Dorporal, P.R. Bullock, H. Pokrant, and J. Culley "Potential applications of RADARSAT data to agriculture and hydrology", *Canadian Journal of Remote Sensing*, vol. 19, pp. 317-329, 1993, (CCRS #: 1099536).

- [101] R.J. Brown, B. Brisco, F.J. Ahern, C. Bjerkelund, M. Manore, T.J. Pultz, and V. Singhroy "SAR application calibration requirements", *Canadian Journal of Remote Sensing*, vol. 19, No. 3, pp.193-203, 1993, (CCRS #: 1099973).
- [102] L.C. Chen, , T.A. Teo and C.L. Liu, "The geometrical comparisons of RSM and RFM for FORMOSAT-2 satellite images," *Photogrammetric Engineering and Remote Sensing*, vol 72, no 5, pp. 573-579, 2006.
- [103] M. Ettarid, A. Ait M'Hand and R Aloui, "Digital true orthophotos generation", in *Proc. of the FIG Working Week*, Cairo, Egypt, 2005, pp.563-571.
- [104] C. S. Fraser, H. B.Hanley and T. Yamakawa, "Three-dimensional geopositioning accuracy of IKONOS imagery", *Photogrammetric Record*, vol 17, pp. 465-479, 2002.
- [105] D.C. Brown, "Decentering distortion of lenses," *Photogrammetric Engineering*, vol 32, no. 3, pp.444-462, 1966.
- [106] L. C. Chen, T. A. Teo, and J.Y. Rau, "Optimized patch back projection in orthorectificaion for high resolution satellite images," *Int. Archives of Photogrammetry and Remote Sensing*, vol 35, no.B2: pp. 586-591, 2004.
- [107] L.C. Chen and L.H. Lee, "Rigorous generation of digital orthophoto from SPOT images". *Photogrammetric Engineering and Remote Sensing*, vol 59, no.5: pp. 655-661, 1993.
- [108] I. Champion. and R. Faivre "Sensitivity of the radar signal to soil moisture: Variation with incidence angle, frequency, and polarization", *IEEE Transactions on Geosciences and Remote Sensing*, vol. 35, pp. 781-783, 1997.
- [109] T. Toutin. "Potential of road stereo mapping with RADARSAT images", *Photogrammetric Engineering and Remote Sensing*, vol. 67, no 27 p. 474-481, 2001.
- [110] D.L. Light, D. Brown, A. Colvocoresses, F. Doyle, M. Davies, , A. Ellasal, , J. Junkins, J. Manent, A. McKenney, R. Undrejka, and G. Wood, "*Satellite Photogrammetry*", Manual of Photogrammetry (Fourth Edition), Falls Church, USA, 1980, pp. 883-977.
- [111] C.H. Ahn , S.I Cho and J. C. Jeon, "Orthorectification software applicable for IKONOS high-resolution images: GeoPixel-Ortho", in *Proc. IEEE Geosciences and Remote Sensing Symposium*, Sydney, Australia, July 2001, pp. 555-557.
- [112] K. Di, R. Ma and R. Li, "Rational functions and potential for rigorous sensor model recovery." *Photogrammetric Engineering and Remote Sensing*, vol. 69, no.1, 33-41, 2003.

- [113] H. S. Jung and D.Y. Park and S. C. Lee, “The geometric correction of SPOT 5 HRG images using an orbit attitude and minimum control points”, in *Proc. IEEE Intl. Geosciences and Remote Sensing Symposium, (IGRSS’05)*, S. Korea, 2005, pp. 3273-3276.
- [114] J.B. Lee, Y. Huh, B. Seo, and Y. Kim, “Improvement the positional accuracy of the 3D terrain data extracted from IKONOS-2 satellite imagery”, *Intl. Archives of Photogrammetry and Remote Sensing*, vol. 34, no. B3, pp. B142- B145, 2002.
- [115] J. Grodecki, “IKONOS stereo feature extraction – RPC Approach”, in *Proc. The ASPRS Annual Conf.*, St Louis, Missouri, USA, April 23-27, 2001, pp. 432-440.
- [116] T. Toutin, “Block bundle adjustment of Ikonos in-track images”, *Intl. Journal of Remote Sensing*, vol, 24, no. 4, pp. 851-857, 2003.
- [117] T. Kim, D. Shin, and Y.R. Lee, “Development of robust algorithm for transformation of a 3D object point onto a 2d image point for linear pushbroom imagery”, *Photogrammetric Engineering and Remote Sensing*, vol 67, no. 4: pp. 449-452. 2001.
- [118] P. V. Radhadevi, R. Ramachandran and A. S. R. K. V. Murali Mohan, “Restitution of IRS-1C PAN data using an orbit attitude model and minimum control”, *ISPRS Journal of Photogrammetry and Remote Sensing*, vol. 53, pp. 262-271, 1998.
- [119] A. Plaza *et al.*, “AMEEPAR: Parallel morphological algorithm for hyperspectral image classification in heterogeneous networks of workstations”, *Lecture Notes in Computer Science*, vol. 3391, pp. 888–891, 2006.
- [120] D. Valencia and A. Plaza, “FPGA-based compression of hyperspectral imagery using spectral unmixing and the pixel purity index algorithm,” *Lecture Notes in Computer Science*, vol. 3993, pp. 24–31, 2006.
- [121] G. Rajiv., and I. H. Richard, “Linear pushbroom camera”, *IEEE Transactions on Pattern Analysis and Machine Intelligence*, vol. 19, no. 9, pp. 963-975, 1997.
- [122] S. K. Park and R. A. Schowengerdt, “Image reconstruction by parametric cubic convolution”, *Computer Vision, Graphics and Image Processing*, vol. 23, no. 3, pp. 258-272, Sep, 1983.
- [123] J. R. Kim, and J.P. Muller, “3D reconstruction from very high resolution satellite stereo and its application to object identification”, *Intl. Archives of Photogrammetry and Remote Sensing and Spatial Information Sciences*, vol. 34, no. B4, pp. 637-643, 2002.
- [124] D. Kristóf, É. Csató, and D. Ritter, “Application of high-resolution satellite images in forestry and habitat mapping – evaluation of IKONOS images through a Hungarian

- case study”, *Intl. Archives of Photogrammetry and Remote Sensing and Spatial Information Sciences*, vol. 34, no. B4, pp. 602-607, 2002.
- [125] M. Madani, “Real-Time Sensor-Independent positioning by rational functions”, *Proc. ISPRS Workshop on Direct Versus Indirect Methods of Sensor Orientation*. Barcelona, Spain, November 25-26, 1999, pp. 64-75.
- [126] M. Abrams, “ASTER: data products for the high spatial resolution imager on NASA’s EOS-AM1 platform,” *Intl. Journal of Remote Sensing*, vol. 21, pp. 847–861, 2000.
- [127] J. Setoain, C. Tenllado, M. Prieto, *et al.*, “Parallel hyperspectral image processing on commodity graphics hardware,” in *Proc. Intl. Conf. on Parallel Processing*, Columbus, OH, USA, 2006, pp 465-472.
- [128] V. Tao, and Y. Hu, “3D Reconstruction methods based on the rational function model”, *Photogrammetric Engineering and Remote Sensing*, vol 68, pp. 705-714, 2002.
- [129] S. Vassilopoulou, L. Hurni, V. Dietrich, E. Baltsavias, M. Pateraki, E. Lagios and I. Parcharidis, “Orthophoto generation using IKONOS imagery and high-resolution DEM: a case study on volcanic hazard monitoring of Nisyros Island (Greece)”, *ISPRS Journal of Photogrammetry and Remote Sensing*, vol. 57, pp. 24-38, 2002.
- [130] K. Jacobsen, G. Buyuksalih, A. Marangoz, U. Sefercik and I. Buyuksalih, “Geometric conditions of space imagery for mapping”, in *Proc. of Recent Advances in Space Technology (RAST)*, Istanbul, Turkey, 2005, pp. 116-127.
- [131] J. R. G. Townshend, C. O. Justice, C. Gurney, and J. McManus, “The impact of misregistration on change detection,” *IEEE Transactions on Geosciences and Remote Sensing*, vol. 30, no. 5, pp. 1054–1060, Sep. 1992.
- [132] E.M. Mikhail, *Observations and Least Squares*, New York: Harper and Row, 1976.
- [133] M. Unser, “Sampling—50 years after Shannon,” in *Proc. IEEE*, vol. 88, pp. 569–587, Apr. 2000.
- [134] T. Blu, P. Thévenaz, and M. Unser, “Complete parameterization of piecewise-polynomial interpolation kernels” *IEEE Transactions on Image Processing*, vol. 12, no. 11, pp. 1297-1309, Nov 2003.
- [135] D. Seidner, “Polyphase anti-aliasing in resampling of images”, in preparation.
- [136] R.G. Keys, “Cubic convolution interpolation for digital image processing”, *IEEE Transactions on Acoust, Speech Signal and Processing*, vol. ASSP-29, no. 6, pp. 1153-1160, Dec.1981.

- [137] S. K. Park and R. A. Schowengerdt, "Image reconstruction by parametric cubic convolution", *Computer Vision, Graphics and Image Processing*, vol. 23, no. 3, pp. 258-272, Sept.1983.
- [138] E. H.W. Meijering, K. J. Zuiderveld, and M. A. Viergever, "Image reconstruction with symmetrical piecewise nth-order polynomial kernels," *IEEE Transactions on Image Processing*, vol. 8, pp. 192–201, Feb. 1999.
- [139] F. Arif and M. Akbar, "A new approach for anti-aliasing raster data in air borne imagery", in *Proc. of SPIE vol. 5969, Photonic North Intl. Symposium*, Toronto, Canada, 2005, pp. 5969L-1 to9.
- [140] T. B. Thévenaz, and M. Unser, "Linear interpolation revitalized" *IEEE Transactions on Image Processing*, vol. 13, no. 5, pp. 710-719, 2004.
- [141] A. V. Oppenheim and R. W. Schaffer, *Discrete-Time Signal Processing*, Prentice Hall, Englewood, New Jersey, 1999.
- [142] V. Vitchev, "Mathematical basics of band limited sampling and aliasing", [Online document] 2005 Jan 22, Available: <http://www.rfdesin.com/pdf>.
- [143] M. T. Heath, "Sampling, reconstruction and anti-aliasing" in *Scientific Computing – An Introductory Survey*, CRC Press, New York, USA, 2001, pp.1-28.
- [144] F. Arif, M. Akbar and A. M. Wu, "Projection method for geometric modeling of high resolution satellite images applying different approximations", *Lecture Notes in Computer Sciences*, vol: 4319/2006, in *Proc. IEEE Pacific-Rim Symposium on Image and Video Technology (PSIVT'06) held in Hsinchu*, Taiwan, 11-13 December 2006, pp. 421-432.
- [145] P. P. Vaidyanathan, *Multirate Systems and Filter Bank*, Prentice Hall, Englewood, New Jersey, 1993.
- [146] C. R. Appledorn, "A new approach to the interpolation of sampled data," *IEEE Transactions on Medical Images*, vol. 15, pp. 369–376, June 1996.
- [147] I. Kaplan, "The Daubechies D4 Wavelet Transform," [Online document] 2007 Jan 12, Available: <http://www.bearcave.com/wavelets/daubechies/index.html>.
- [148] G. Strang and G. Fix, "A Fourier analysis of the finite element variational method," *Constructive Aspects of Functional Analysis*, (G. Geymonat, Edition). Rome, Italy, 1973, pp. 793–840.
- [149] T. Blu, P. Thévenaz, and M. Unser, "Generalized interpolation: Higher quality at no additional cost," in *Proc. IEEE Intl. Conf. on Image Processing*, vol. 3, 1999 Oct. 25–28, pp. 667–671.

- [150] R.G. Keys, "Cubic convolution interpolation for digital image processing", *IEEE Transactions on Acoustic, Speech and Signal Processing*, vol. ASSP-29, no. 6, pp. 1153-1160, Dec.1981.
- [151] T. Blu, P. Thévenaz, and M. Unser, "Minimum support interpolators with optimum approximation properties," in *Proc. IEEE Int. Conf. on Image Processing*, vol. 3, 1998 Oct. 4-7, pp. 242-245.
- [152] S. Harris and J. Ross, *Beginning Algorithms*, Wiley Publishing Inc., Indianapolis, Indiana USA, pp 4-9, 2006.
- [153] J. Ingada, V. Muron, D. Pichard and T. Feuvrier, "Analysis of artifacts in subpixel remote sensing image registration," *IEEE Transactions on Geosciences and Remote Sensing*, vol. 45, No. 1, pp.588-597, 2007.
- [154] F. Arif, M. Akbar and A. M. Wu, "Most favorable automatic georeferencing based on GCPs selection using least square method," in *Proc. The 4th Intl. Conf. on Digital Earth*, Taipei, Taiwan, 2006, pp. 183-192.
- [155] B. R. Corner, R. M. Narayanan and S. E. Reichenbach, "Noise estimation in remote sensing imagery using data masking", *Intl. Journal of Remote Sensing*, vol. 24, no. 4, pp. 689-702, 2003.
- [156] D. Lu, P. Mausel, E. Brondizio, and E. Moran, "Change detection techniques," *Intl. Journal of Remote Sensing*, vol. 25, no. 12, pp. 2365-2407, Jun. 2004.
- [157] Y. Liu, S. Nishiyama, and T. Yano, "Analysis of four change detection algorithms in bi-temporal space with a case study," *Intl. Journal of Remote Sensing*, vol. 25, no. 11, pp. 2121-2139, Jun. 2004.
- [158] K. Jacobsen, "Geometry of satellite images - calibration and mathematical models", in *Proc. ISPRS Intl. Conf.*, Jeju, S. Korea, 2005, pp. 182-185.
- [159] P. Thévenaz, T. Blu, and M. Unser, "Interpolation revisited," *IEEE Transactions on Medical. Images.*, vol. 19, pp. 739-758, July 2000.
- [160] A. R. Gillespie, A. B. Kahle, and R. E. Walker, "Color enhancement of highly correlated images: Channel ratio and chromaticity transformation techniques," *Remote Sensing Environment*, vol. 22, no. 3, pp. 343-365, Aug. 1987.
- [161] J. G. Liu, "Smoothing filter based intensity modulation: A spectral preserve image fusion technique for improving spatial details," *Intl. Journal of Remote Sensing*, vol. 21, no. 18, pp. 3461-3472, Dec. 2000.